Alma Mater Studiorum · University of Bologna

School of Science
Department of Physics and Astronomy
Master Degree in Physics

Fourier-domain OCT with undetected mid-infrared photons in the high-gain regime

Supervisor:

Prof. Francesco Minardi

Co-supervisor:

Prof. Maria Chekhova
Dr. Kazuki Hashimoto

Submitted by:
Giovanni Zotti

Academic Year 2023/2024

Abstract

I present the first experimental implementation for Fourier-domain optical coherence tomography (OCT) using undetected mid-infrared photons in the high-gain regime. The core component is a custom-designed, aperiodically poled Potassium Titanyl Phosphate ($KTiOPO_4$) crystal, enabling broadband parametric down-conversion (PDC) with high amplification. After discussing the theoretical background of classical OCT, nonlinear processes, PDC, and interference with undetected photons, I report the experimental performance of my setup. It achieves a typical signal-to-noise ratio (SNR) of ≈ 40 dB, axial resolution of ≈ 30 μm, depth range of ≈ 320 μm, and macroscopic lateral resolution of ≈ 3.3 mm. I demonstrate the setup's capability to resolve real microstructures and its advantage over classical OCT in operating with samples obscured by a Germanium window. Additionally, I confirm the high-gain regime's potential for strong signal power, allowing detection with standard Si power meters and time-gated measurements.

Contents

Introduction

Optical coherence tomography (OCT) is a powerful and well-established investigation technique, able to provide real-time, non-invasive, and noncontact cross-sectional imaging of a large plethora of different samples. Basically, OCT exploits a Michelson-type interferometer: the probing light beam is sent to a beam splitter, which conveys the two output beams into different perpendicular paths, the reference arm and the sample arm. A conceptual scheme is illustrated in Figure 1 [1].

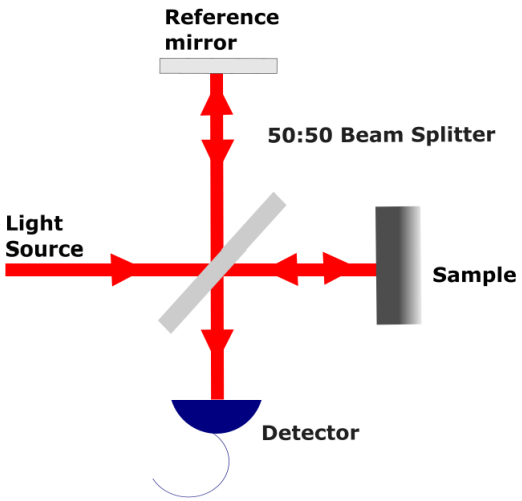

Figure 1: *A very simple scheme illustrating the fundamental design for classical OCT. The heart of the setup is the beam splitter, which splits the incoming light source into two beams, propagating perpendicularly. The first one moves along the sample arm, probes the sample and eventually gets reflected; the second one propagates along the reference arm, which ends with the reference mirror. We can then collect the interference pattern of the two beams after backscattering to reconstruct the cross-sectional image of the sample.*

We usually refer to the sample arm direction as axial direction, whereas the perpendicular one is called transverse direction. If interference occurs between the backscattered beams, it will yield spatial information about the sample microstructure. Thus, we can

exploit the interference pattern's detection for imaging reconstruction. By performing an axial scan, often indicated as A-scan, we can acquire the depth profile of the sample under investigation. Alternatively, we can move transversely the beam (or equivalently the sample) in order to obtain its transverse profile, which is known as B-scan. By combining these two modalities, we can reconstruct a full 2D cross-sectional image of the sample. It is possible to generate 3D volumetric data as well, generalizing the procedure to an additional dimension [1]. OCT can be achieved in two alternative modalities, Time-domain (TD) OCT and, more commonly, FD (Fourier-domain) OCT. In the first case, the detector is usually a simple photodetector; in the second one, it is instead replaced by a spectrometer. The differences between these approaches will be elucidated in the next chapter.

Since its invention in the late 1980s [2], OCT has proved revolutionary in the study of organic microstructures, especially in the field of ophthalmology, allowing the achievement of fundamental results like imaging cross-sections of the human retina [3]. Technical and theoretical upgrades have led to continuous improvement in this technique's performance, which stands alone among competing non-destructive investigation methods. Among the others, some unprecedented advantages are:

- high-resolution, which, at the state of the art, lies in the range $1 - 15$ μm. Thus, it is approximately one-two orders of magnitude finer than standard ultrasound imaging [1];

- enhanced sample penetration when compared to confocal microscopy, an extremely accurate technique (up to 1 μm depth resolution can be achieved) but with limited depth range (some hundreds of micrometers for biological tissues). On the opposite, commercial OCT setups can reach up to $1 - 2$ mm penetration depth [1];

- independence of the axial resolution on the focusing (another significant limit affecting confocal microscopy). In particular, it will be shown that the depth resolution strictly depends on the sample beam bandwidth. For example, in the Gaussian beam approximation, we have that

$$\mathrm{FWHM_z} = \frac{2\ln 2}{\pi}\frac{\lambda_c^2}{\Delta\lambda}, \tag{1}$$

  where $\mathrm{FWHM_z}$ is the depth resolution (formally, the full width at half maximum of the OCT peak), λ_c the central wavelength of the source, $\Delta\lambda$ its bandwidth (this last one is defined as the full width at half maximum of the spectrum [4]);

- When compared to X-ray computed tomography or magnetic resonance imaging, OCT is superior in terms of cost, safety, contrast, and resolution. Moreover, we do not need to encapsulate the sample, nor move or rotate the detector [5].

Inevitably, all these promising features have been responsible for increasing interest in OCT beyond the clinical medical field: today, it has been involved in a huge number of diverse sectors, from cultural heritage conservation to material characterization, from industrial quality control to fluid sensing. A list of promising applications can be found in the abstract collection of the symposium on OCT for non-destructive testing [6]. A fundamental limit to this process is that OCT applications have been restricted to the visible and near-infrared regions (up to 1.5 μm, NIR from now on) so far, which are optimized for the biological tissues but proved extremely ineffective for probing highly scattering materials, like oil paints, micro-porous materials, or alumina-based ceramics. The main physical reason lies in the high scattering contribution at such low wavelengths, drastically affecting the depth range and thus making OCT inappropriate.

This issue can be addressed by extending the OCT exploitable range up to the mid-infrared region (MIR from now on) since the scattering loss is predicted to be much lower at these frequencies (more in detail, it should be $\propto 1/\lambda^4$, at least assuming the particle is small in comparison to the wavelength [7]). The potential of MIR OCT has been especially emphasized for the probing of highly scattering novel ceramic materials, predicting a notable enhancement of the depth penetration already by shifting the probing wavelength to $2-4$ μm, according to Montecarlo simulations [8]. Spectral ranges up to 5 μm are the most promising ones since they are immediately below the critical region $5-7.5$ μm, where water absorption highly affects the performance [9]. This technique could be beneficial when materials that do not transmit in the NIR are involved as well (e.g. Ge, whose transmission curve is available in [10]).

It is thus a matter of fact that achieving this result would be extremely beneficial for high-precision fabrication and investigation. However, this is probably the most demanding challenge OCT has had to face since its invention.

The main difficulty lies in the fact that the current implementations of this technique rely on the usage of semiconductors (for example HgCdTe and InSb) for both detectors and light sources. Operating in the MIR spectral region then requires matching the bandgap with an energy an order of magnitude lower than that of the visible, while competing with the thermal noise. This fundamentally affects the performance of the setup, making current MIR operating devices highly expensive (cryogenic cooling is required for both sources and detectors) and unable to compete with the performance of their NIR counterparts in terms of sensitivity and noise [11].

MIR OCT was first achieved in 2007 by [12]: their system involved a broadband quantum cascade laser source (InGaAs/AlInAs), continuously emitting in the $6-8$ μm wavelength range, and a liquid nitrogen cooled HgCdTe detector. The axial resolution resulted in around 30 μm, with a dynamic range (defined as the ratio between the maximum and the minimum measurable optical power of the interference) of around 30 dB, significantly lower than the ones reported for standard OCT, 90 dB to 140 dB [13], and heavily affected by the modulation of the spectral shape. Many attempts have been made to enhance the effectiveness of this setup by employing alternative sources

(superluminescent quantum cascade laser [14], supercontinuum sources [15], or novel ultrafast optical parametric oscillators (OPOs) [9]) or detectors (low-cost pyroelectric detector [16]). However, despite significant developments in terms of the signal-to-noise ratio SNR (e.g. 81.7 dB in [16]) and acquisition time, the limitations are still far from being overcome, with the axial resolution typically lying in the range $30 - 50$ μm. A radical paradigm shift is thus necessary.

Recently, approaches to circumvent the need for MIR detectors have emerged. They rely on broadband upconversion, in other words, the spectrum shifting from the MIR region to the NIR region before detection. Different proposals to achieve efficient frequency shift exist, mainly involving sum-frequency generation [17], [18] or difference-frequency generation [19] inside properly poled nonlinear crystals. In this way, we can replace inefficient MIR detectors with better-performing Si detectors. Combining this strategy with the usage of a supercontinuum source, Israelsen et al. managed to achieve a remarkable axial resolution of 8.6 μm and a 60 dB sensitivity [18]. However, the setup was limited by the need to use a sophisticated broadband MIR laser as main source, as well as to employ an additional high-power laser for the upconversion setup, increasing the complexity of the system. Moreover, the upconversion module was characterized by a radially varying spatial mode profile, forcing the authors to use a multimode fiber and thus limiting the performance of the spectrometer. Yagi et al. [19] managed to achieve similar performance, with a notable enhancement in the A-scan rate, by adapting the upconversion time-stretched infrared spectroscopy setup from [20] to OCT. However, they had to develop a suitable MIR laser, opting for a complex difference-frequency generation (DFG) source realized with a femtosecond mode-locked Yb fiber laser as a master oscillator. A simpler design would be preferable.

Thanks to the *undetected photons* technique, nonlinear and quantum optics may offer another innovative approach. By replacing the beam splitter of the Michelson-type interferometer with a $\chi^{(2)}$ nonlinear crystal (adopting the design in figure 2), we can exploit the resulting idler and signal beams (produced in the SPDC process) respectively as sample and reference beams. In this geometry, the interference at the output will be due to the phase delays of all three photons (the pump, signal, and idler), allowing us to analyze the idler reflection of the sample without detecting the idler photons but just considering the signal photons [21]. In this way, we can circumvent both the necessity for MIR sources and detectors, plus we considerably simplify the experimental design compared to the techniques above.

Paterova et al. successfully achieved MIR OCT (3 μm) with undetected photons in [22]. However, the setup suffered from the narrow bandwidth of their tunable source, achieving an axial resolution limited at 93 μm. A promising result was accomplished by Vanselow et al. in [23]: by employing a nonlinear ppKTP (periodically poled Potassium Titanyl Phosphate KTiOPO4) crystal characterized by ultra-broadband SPDC spectra, they managed to demonstrate MIR OCT with 10 μm axial resolution and 20 μm lateral resolution. Moreover, they achieved the shot-noise level of detection, observing 10^6 times

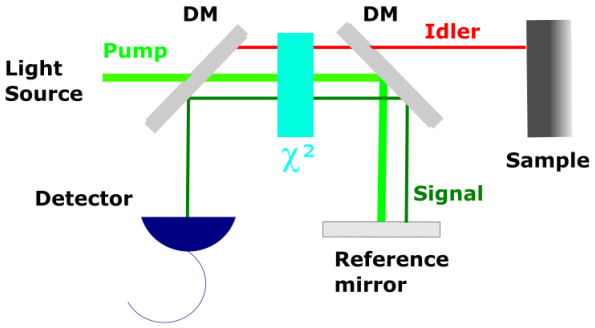

Figure 2: *Simple illustration of the experimental scheme to perform OCT with undetected photons. The beam splitter of the usual setup (the one in figure 1) is replaced by dichroic mirrors (DM). The nonlinear source is inserted between them, in order to generate the idler, which propagates along the sample arm, and the signal, which goes into the reference arm.*

more sensitivity at equal integration time and probe power. In [23], the problem of having a sufficiently large idler bandwidth was solved, even if the design of nonlinear crystals can be further optimized. However, these results are still affected by the intrinsic limits of operating in the low-gain regime of PDC. Under this condition, the number of photons per mode generated inside the nonlinear crystal is much smaller than one [24]. Thus, the measurement inevitably requires high-sensitivity detectors [25].

On the contrary, the high parametric gain regime is characterized by several (easily more than 10) photons per mode, to be precise the generation rate and the number of produced photons increase exponentially along the nonlinear medium [26]. The average power to be detected rises to μW or mW level, making it possible to use ordinary detectors (i.e. Si-based power meters)[27]. Moreover, the seeding effect inside the nonlinear crystal lets us have a weak, non-invasive idler beam to probe the sample and an amplified signal beam easier to detect [28]. Machado et al. [24] have demonstrated NIR OCT (idler centered at $\lambda_I = 1.55$ μm, signal at 810 nm) with undetected photons in the high-gain regime. Their work was unfortunately affected by severe limitations, in particular the narrow bandwidth, constraining the depth resolution to ≈ 30 μm and the depth range to ≈ 300 μm. Hashimoto et al. [28] have addressed these limitations by employing an aperiodically poled lithium niobate (APLN) crystal, achieving ultrabroad bandwidth spontaneous parametric down-conversion (SPDC) spectra (experimentally determined to be ≈ 30 THz) and a consequent axial resolution of 11 μm. However, their work was still restricted to the NIR region.

In this work, I report a novel experimental setup to perform MIR OCT with undetected photons in the high-gain regime, realized in collaboration with Prof. Dr.

Chekhova's research group, and in particular with my co-supervisor Dr.Hashimoto, at Max Planck Institute for the Science of Light. To do this, we rearranged the setup in [29], successfully employed to realize Fourier-transform infrared spectroscopy (FTIR) with undetected photons, making it suitable for OCT measurements. An important feature of the project is its nonlinear source, a KTP crystal whose poling period is chirped along the pump propagation (apKTP), characterized by a promisingly large idler bandwidth (around 0.8 μm with the central wavelength at ≈ 3 μm) and granting high-gain parametric amplification.

My thesis is divided into the following parts: the first chapter is dedicated to the classical OCT technique, providing an overview of the fundamental working principles, advantages and limits of the current state of the art, fields of application, and, eventually, alternative proposals to perform mid-IR OCT; the second one focuses on the description and explanation of quantum nonlinear processes as well as nonlinear sources, providing the background needed to understand imaging with undetected photons fully; eventually, the third chapter illustrates in detail my activity, going into the description of the setup, explaining data processing and experimental expedients, and comparing the final results with the ones obtained in similar scientific works.

Chapter 1

Optical Coherence Tomography

1.1 OCT: fundamental aspects

1.1.1 OCT potential

Optical Coherence Tomography, OCT in short, was developed and successfully applied to study biological tissues in [2]. Already at this early stage, it proved to be a promising alternative to other non-invasive investigation techniques (e.g. magnetic resonance imaging, x-ray computed tomography, confocal microscopy): it offered extremely high depth resolution, around 17 μm, detection sensitivity as low as 10 fW (that is the minimum detectable reflected optical power), and fast acquisition time, approximately 200 ms, while overcoming the need for ultrashort pulse laser sources (in contrast to alternative time-domain techniques). Moreover, its axial resolution proved to be independent of the available numerical aperture (one of the main limitations of confocal microscopy), allowing it to operate with a narrow beam diameter (around 9 μm). It is interesting to notice that, already in [2], the authors identify the scattering as one of the main limitations to OCT since it drastically affects the penetration depth. In particular, they underline this fact when analyzing fatty-calcified samples, in which scattering arose as the main responsible for the reduced penetration range. Since then, continuous upgrades have further optimized OCT, which is now an indispensable imaging technique in medical diagnostics. To better understand the role it plays, it can be useful to compare graphically its performance with ultrasound imaging and confocal microscopy since it shares common features with both of them. A plot is reported in Figure 1.1, taken from [1].

Thus, OCT lies somewhere in between the operative ranges of prominent competing techniques, achieving an axial resolution comparable with the one of confocal microscopy, while guaranteeing the same penetration depth as ultrasound imaging. This makes it irreplaceable for the diagnostics and the treatment of ocular diseases [30]. Moreover, even if the depth range is still limited up to $2-3$ mm because of scattering and absorption, this deficiency can be addressed by integrating OCT with various instruments, like catheters

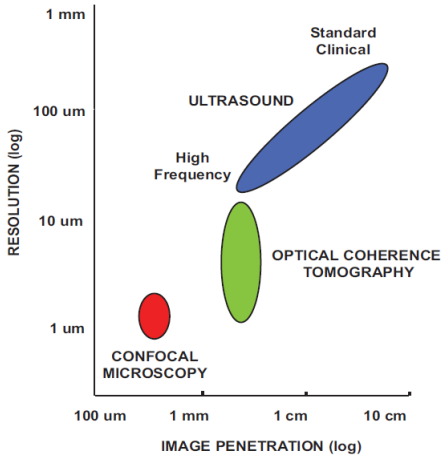

Figure 1.1: *Pictorial comparison between the performances of main imaging techniques in medical diagnostics. Taken from [1].*

or endoscopes, making internal body imaging possible as well [1].

Conceptually, ultrasound imaging and OCT are very similar. In both cases, the probing beam is directed onto the sample, it gets backscattered or back-reflected according to the acoustic/optical properties of the sample's layering structure, and, eventually, it brings spatial information which can be decoded by measuring the echo time. The main physical difference lies in the speed of the beam, which leads to important implications. While for ultrasound the measurements of echoes require a time resolution of around 10^2 ns, which is compatible with the electronic detection limits, the detection of echo time delays using a light beam would need a time resolution of about 30 fs, very difficult to detect directly. Thus, alternative measurement methods are necessary: the most employed is low-coherence interferometry [1].

1.1.2 Low-coherence interferometry

Interferometry has been known as one of the most reliable and precise measurement techniques for a long time. It allowed us to achieve fundamental results in physics, like the Michelson and Morley experiment or the detection of gravitational waves. The general idea is measuring the interference pattern between two beams, the first one probing the sample, and the second one propagating along a known fixed reference path. If we call E_s the sample arm field, and E_r the reference arm one, the output intensity will be given by

$$I = (E_r + E_s)(E_r + E_s)^*. \tag{1.1}$$

For the moment, we simplify this general result by considering just one single reflecting layer (the formal demonstration is in the next chapter)

$$I \propto |E_s|^2 + |E_r|^2 + 2|E_r||E_s| \cos(k\Delta L + \phi), \tag{1.2}$$

with ΔL being the optical path difference OPD (in the general case, we would have many values of ΔL). The key aspect of low-coherence interferometry is the employment of a low temporal coherence source: if we used a high-coherence pump, interference would be detected for a wide range of OPDs, in other words across all the sample's length. We would then lose any possibility of resolving its single regions or layers. On the contrary, low-coherence light is characterized by statistical phase fluctuations above a certain distance, the coherence length l_{coh}. This means that interference will happen just for OPD $< l_{coh}$: if we then operate with sufficiently low l_{coh}, we will be able to select just the region of the sample satisfying this coherence gate condition, being able to get information about its internal structure. If we now recall the usual relation [31]

$$l_{coh} \propto \frac{1}{\Delta\lambda}, \tag{1.3}$$

we can immediately deduce that a broad emission spectrum must characterize a low-coherence source.

1.1.3 TD-OCT and FD-OCT

Low-coherence interferometry OCT can be achieved with two distinct approaches: Time-domain (TD) and Fourier-domain (FD) OCT. In both cases, the experimental setup is essentially the one depicted in figure 1.

In TD-OCT, we usually collect the output intensity using a simple photodetector. Therefore, interference can be detected only when the OPD between the sample beam and the reference beam is smaller than the coherence length of the source. If the sample is composed of multiple reflecting layers and l_{coh} is smaller than their distance, we can simply move the reference (or, equivalently, the sample) to change the region of the sample for which the condition OPD $< l_{coh}$ is satisfied. By doing so, we can measure interference for all backscattering layers, and resolve each one's position by identifying all maxima of interference (corresponding to various OPD $= 0$). In this way, we are able to reconstruct the whole reflectivity profile in depth (A-scan). An explanatory representation is reported in figure 1.2.

En face TD-OCT exists as well: in this case, we collect one-dimensional reflectivity profiles moving the spot transversally while keeping the axial coordinate unchanged. This approach is needed when we want to collect a constant depth scan image in real-time [32].

In FD-OCT we measure and interrogate the interference spectrum over a wide range of wavelengths instead. In this case, l_{coh} still dictates the minimum resolvable distance,

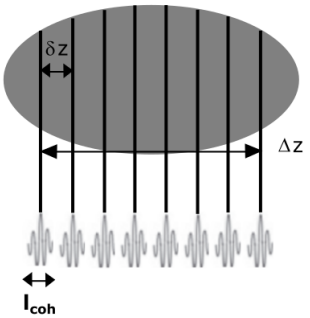

Figure 1.2: *Simple illustration of TD-OCT working principle. Each reflecting layer can be probed by changing the OPD, since* $l_{coh} < \delta z$.

but the interference can be recorded along the whole sample at once, with the depth range becoming primarily limited by the measurement conditions. The main advantage is that we can reconstruct the complete depth profile after one single measurement, without the need to implement mechanical scanning, but just by resolving the contribution of each layer to the global interference pattern exploiting Fourier analysis. Even FD-OCT can be achieved using two different approaches[32]:

- Spectrometer-Based OCT (SB-OCT): this technique relies on the setup in figure 1, with the detector being a spectrometer. The key idea is to exploit Fourier analysis to decode the spatial information hidden in the low-coherence interferometer output. In general, the interference spectrum will be characterized by a precise modulation pattern, with maxima and minima at certain wavelengths. The distance between adjacent maxima (it is not correct to talk of period, since the modulation may not be periodical), and so the number of peaks within the spectrometer range, depends on the OPD [33]. Therefore, when we image a real multilayered sample, each layer will give its contribution to the modulation figure depending on its depth (provided the usual OPD $< l_{coh}$ condition is satisfied). By performing a fast Fourier transform of the interference pattern, we can eventually decrypt the spatial profile encoded inside it. It must be added that the spectrometer plays a crucial role in this process, converting the optical input into a processable electrical output. A critical limitation is then the resolution $\delta\lambda$ of the spectrometer, which must be fine enough to sample the succession of maxima and minima in the channeled spectrum.

- Swept-Source OCT (SS-OCT): in this technique, the usual setup is modified replacing the broadband source with a swept source, typically a tunable laser, and employing a photodetector like in TD-OCT. The purpose is to reconstruct the interference pattern by rapidly sweeping the wavelength range, so exploiting the tunable source. The photo-detected signal will be more and more similar to the

channeled spectrum the narrower the source bandwidth is. The minimum requirement is that the $\delta\lambda$ is smaller than the spectral distance between adjacent peaks. In this way, we no longer have the need for a broadband spectral source.

SB-OCT is by far the prevailing modality of FD-OCT. However, in recent years the interest in it has notably increased, owing to the availability of new effective tunable sources [32]. In particular, SS-OCT proved to be highly effective for the realization of ultra-high speed OCT, reaching the record line rate of 5 MHz [34].

FD-OCT offers a fundamental advantage compared to TD-OCT: it delivers the reflectivity for all axial points at once. Therefore, it is definitely superior in terms of the acquisition rate, reaching a line rate of $\approx$ 300 kHz, three times larger than the one for TD-OCT [32]. However, this net advantage comes with some shortcomings:

- roll-off: the sensitivity of an OCT system is mainly determined by the amount of superimposition between the wavetrain reflected by the reference and the one coming from the sample [32]. In TD-OCT, we are continuously moving the reference/sample position, changing the OPD until we get the maximum interference condition $OPD = 0$ for a certain reflecting layer (this position is usually referred to as the zero path difference position ZPD). Clearly, this condition corresponds to a perfect superimposition of the two wavetrains; therefore the sensitivity does not vary with the depth. On the contrary, in FD-OCT we keep fixed both reference and sample positions. Let us consider a simple two-layer sample, having a certain length Δz. The wavetrains coming from the front and the back will be characterized by a certain spatial extension, which we may define as the length after which the wave loses intensity. This distance is certainly longer than the coherence length of the source, nonetheless it is finite. In particular, it may be interpreted as a sort of counterpart of the coherence length: it dictates the maximum OPD below which interference can be recorded in the operative range of wavelengths [32]. We will therefore call it CL for simplicity. CL mainly depends on the experimental, measurement conditions. Figure 1.3 pictorially describes the process

  For example, in SB-OCT it is given by the dispersion/diffraction process inside the spectrometer, whereas in SS-OCT it is inversely proportional to the linewidth $\delta\lambda$ emitted by the source [32]. Now, if we want to visualize the two OCT peaks, it is necessary to have superimposition between both sample-coming wavetrains and the reference wavetrain. Figure 1.3 clearly shows that this condition will be satisfied with maximum sensitivity just if $CL > 2\Delta z$, and only for the optimal $OPD = 0$ between the front layer and the reference mirror. In most real applications it is difficult to achieve very high CL, therefore the nonperfect superimposition is inevitable.

- *En face* scans: FD-OCT produces just A-scans. Therefore, it is impossible to produce real-time scans at a fixed depth using this technique. Normally, we can

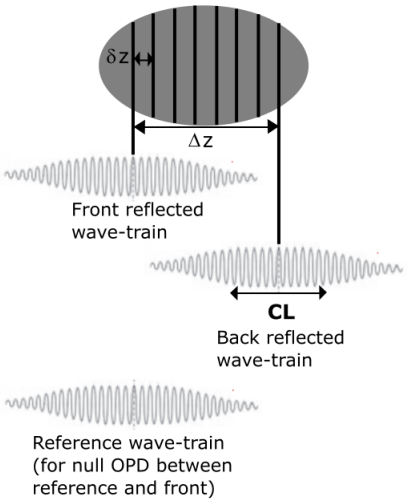

Figure 1.3: *Simple illustration of FD-OCT working principle. In order to be able to resolve both the front layer and the back layer, we need the two reflected wave trains to interfere with the one coming back from the reference. Since typically* $CL \approx 2\Delta z$*, this means we will have inevitably not perfect superimposition with increasing depth.*

reconstruct them after collecting the data for the whole volume. It is then sufficient to slice them while keeping the depth coordinate fixed. This limit has been addressed by several studies, like [35], in which they achieved multi MHz A-scan line rates. However, direct *en face* TD-OCT still results preferable for this purpose.

1.2 FD-OCT: mathematical description

1.2.1 OCT spectrum

This section aims to provide the basic mathematical tools and results to describe FD-OCT. I will just focus on this implementation of OCT, since it is the most widely used and the one of interest in my experimental activity. The following considerations are perfectly valid for both SB-OCT and SS-OCT, which are equivalent from a signal processing view [36]. The main reference is [36], therefore the notation and the way results are shown will be almost analogous.

Firstly, it can be useful to recall the setup for FD-OCT, already reported in figure 1. The broadband source can be mathematically described by a certain spectral intensity distribution, which is a function $S(k)$ of the wavenumber $k = \frac{2\pi}{\lambda}$ satisfying the normalization condition

$$\int S(k)\,\mathrm{d}k = P_0, \tag{1.4}$$

with P_0 being the power of the source. It emits electromagnetic radiation inside the interferometer, with an input intensity given by

$$I_{in} = |E_{in}|^2 = (\sqrt{S(k)}e^{i\phi(k)})(\sqrt{S(k)}e^{i\phi(k)})^*, \tag{1.5}$$

where E_{in} is the input electric field, $\phi(k)$ stands for the initial randomly distributed phase. For simplicity, we assume the propagation of the wave to be one-dimensional, rectilinear, and of plane scalar waves, therefore neglecting any contribution of the polarization. The light travels to the beam splitter, which we consider without losses, and is characterized by reflection coefficient α and transmission coefficient $1 - \alpha$. Then, it is separated into the sample beam and the reference beam. We assume the two arms to have equal length L, with the reference mirror being characterized by a field reflectivity r_r, and the sample being a generic reflecting material. Its field reflectivity r_s can be described as a complex function $a(z)$, with z being the depth. Now we can reconstruct the expressions for the two electric fields after reflection. A fundamental consideration we can make is that their time dependence $e^{i\omega t}$ can be neglected: in fact, we are interested just in the intensity detection process, which averages out this term operating on a large number of optical cycles [36]. Moreover, common paths between sample and reference fields are negligible as well, since their contribution will be absent in the output [36]. These considerations let us write the reference arm field $E_r(k)$ as

$$E_r(k) = \sqrt{\alpha(1-\alpha)}r_r\sqrt{S(k)}e^{i\phi(k)}e^{ik2L}, \tag{1.6}$$

with the additional phase term e^{ik2L} due to propagation in and out the reference arm. For the sample arm field $E_s(k)$, we have to pay attention to the propagation inside the material. Each reflecting layer at depth z will contribute with its field reflectivity $a(z)$ and with a phase term $e^{ikn(z)2z}$, with $n(z)$ being the generic expression for the refractive index and $2z$ being the total distance. Moreover, we will have an additional phase contribution $e^{i\pi}$ for the sample arm field traveling through the beamsplitter [37]. Therefore, we can write

$$E_s(k) = \sqrt{\alpha(1-\alpha)}\sqrt{S(k)}e^{i\pi}e^{i\phi(k)}e^{ik2L}\int_{-\infty}^{+\infty} a(z)e^{ikn(z)2z}\,\mathrm{d}z. \tag{1.7}$$

Equations 1.6 and 1.7 can be used to calculate the total intensity output, which is given by

$$I_{out}(k) = (E_r(k) + E_s(k))(E_r(k) + E_s(k))^*. \tag{1.8}$$

Since we are interested in the interference term, however, it is convenient to work already with

$$I_{int}(k) = E_r(k)E_s^*(k) + E_r^*(k)E_s(k). \tag{1.9}$$

Displacing the sample such that $z > 0$ and assuming $n(z) = 1$ for simplicity, we get

$$I_{int}(k) = \alpha(1-\alpha)S(k)r_r[e^{-i\pi}\int_0^{+\infty} a^*(z)e^{-ik2z}\,\mathrm{d}z + e^{i\pi}\int_0^{+\infty} a(z)e^{ik2z}\,\mathrm{d}z]. \tag{1.10}$$

Noticing that the integral terms correspond to the Fourier transform, we can rewrite it as

$$I_{int}(k) = \alpha(1-\alpha)S(k)r_r\mathcal{F}_k(\tilde{a}(z)), \tag{1.11}$$

with $\tilde{a}(z) = a^*(z)e^{-i\pi} + a(-z)e^{i\pi}$ being the symmetric representation of the reflectivity, $\mathcal{F}_k$ representing the Fourier transform of $\tilde{a(z)}$ for the Fourier pair $2z \to k$. Therefore, if we apply the inverse Fourier transform at both parts of Equation 1.11 and exploit the convolution theorem, we get

$$\tilde{i}(2z) = \alpha(1-\alpha)r_r\mathcal{F}_{2z}^{-1}(S(k)) \circledast a(z), \tag{1.12}$$

with $\circledast$ representing the convolution operation. Equation 1.12 is the fundamental relation of FD-OCT, stating the connection between the reflectivity, the inverse Fourier transform of the source spectrum, and the depth-dependent OCT spectrum. It allows us to calculate the expected OCT signal $|\tilde{i}(z)|$ for any arbitrary $S(k)$ and $a(z)$, giving information about both the amplitude and its FWHM_z, in other words, the spatial resolution.

1.2.2 Single-reflecting layer and Gaussian beam axial resolution

This model allows us to achieve two notable results, the expression of the output intensity for a single reflecting layer (Equation 1.2) and the one for the axial resolution in the case of a Gaussian beam (Equation 1). For the first one, it is sufficient to rewrite the sample arm field considering $a(z) = r_s\delta(z - z_s)$, where r_s is the field reflectivity of the single layer, z_s its position. Therefore, Equation 1.7 becomes

$$E_s(k) = \sqrt{\alpha(1-\alpha)S(k)}e^{i\pi}e^{i\phi(k)}e^{ik2L}r_se^{ikn(z_s)2z_s}. \tag{1.13}$$

Using $n(z_s) = 1$ for simplicity and calculating the total intensity as in 1.8 we get

$$I_{out}(k) = \alpha(1-\alpha)S(k)(r_r^2 + r_s^2 + 2r_rr_s\cos(k2z_s + \phi)), \tag{1.14}$$

with the π phase being generalized to any phase shift ϕ [38]. We have then demonstrated Equation 1.2, as well as the proportionality between the period in the wavenumber domain and the path difference length. Moreover, we can notice that the interference's contribution to the intensity (so to the signal), given by

$$I_{sig}(k) = \alpha(1-\alpha)S(k)(2r_rr_s\cos(k2z_s + \phi)), \tag{1.15}$$

is proportional to r_s (thus to $\sqrt{R_s}$ where R_s is the reflectance).

In order to obtain Equation 1, we need to start from the result 1.12. Assuming again the sample is a simple reflecting layer, we can write

$$|i(z)| = \alpha(1-\alpha)r_rr_s|\mathcal{F}_{2z}^{-1}(S(k))|, \tag{1.16}$$

which is proportional to the field reflectivity r_s. Consequently, we deduce that the amplitude in the OCT spectrum is in general proportional to $r_s = \sqrt{R_s}$. If we continue the calculation for a Gaussian $S(k)$

$$S(k) = \frac{1}{\sqrt{2\pi\sigma_k^2}} e^{-\frac{(k-k_c)^2}{2\sigma_k^2}}, \tag{1.17}$$

we find

$$|i(z)| = \alpha(1-\alpha) r_r r_s | \frac{e^{-ik_c 2z}}{4\pi} e^{-(2z)^2\sigma_k^2/2} |, \tag{1.18}$$

which is a gaussian distribution with standard deviation $\sigma_z = \frac{1}{2\sigma_k}$. Therefore, its $\mathrm{FWHM_z}$ (i.e. the axial resolution) will be given by

$$\mathrm{FWHM_z} = 2\sqrt{2\ln 2}\sigma_z = \frac{\sqrt{2\ln 2}}{\sigma_k} = \frac{4\ln 2}{\mathrm{FWHM_k}}. \tag{1.19}$$

Assuming that the bandwidth is small compared to the central value, $\Delta k = \mathrm{FWHM_k} \ll k_c$, and remembering the relationship $k = \frac{2\pi}{\lambda}$, we can write:

$$\Delta k \approx \mathrm{d}k = |\frac{\mathrm{d}k}{\mathrm{d}\lambda}\,\mathrm{d}\lambda| = \frac{2\pi}{\lambda^2}\Delta\lambda. \tag{1.20}$$

Since $\lambda \approx \lambda_c$ for the condition $\Delta\lambda \ll \lambda_c$, we finally have:

$$\mathrm{FWHM_z} = \frac{4\ln 2}{\Delta k} = \frac{2\ln 2}{\pi}\frac{\lambda^2}{\Delta\lambda} = \frac{2\ln 2}{\pi}\frac{\lambda_c^2}{\Delta\lambda}. \tag{1.21}$$

1.2.3 Visibility

We recall Equation 1.14:

$$I_{out}(k) = \alpha(1-\alpha)S(k)(r_r^2 + r_s^2 + 2r_r r_s \cos(2kz_s + \phi))$$

A fundamental quantity to describe OCT performance is the visibility $\mathcal{V}$, which is defined as

$$\mathcal{V} = \frac{I_{out}^{max} - I_{out}^{min}}{I_{out}^{max} + I_{out}^{min}}. \tag{1.22}$$

Thus, for a simple reflecting layer, we have:

$$\mathcal{V} = \frac{2r_r r_s}{r_r^2 + r_s^2}. \tag{1.23}$$

This expression allows us to rewrite Equation 1.14 as

$$I_{out}(k) = \alpha(1-\alpha)S(k)(r_r^2 + r_s^2)(1 + \mathcal{V}\cos(2kz_s + \phi)). \tag{1.24}$$

The visibility quantifies the quality of the interference, and how easy distinguishing maxima and minima is. Therefore, it is intrinsically related to the performance of the OCT.

Multiplying both sides of Equation 1.24 by $At_I/h\nu_c$, with A being the area of the detector, t_I the duration of the measurement, ν_c corresponding to the central frequency, we can pass to the number of photons at the output

$$\begin{aligned} N_{out}(k) &= \alpha(1-\alpha)\frac{S(k)At_I}{h\nu_c}(r_r^2+r_s^2)(1+\mathcal{V}\cos(2kz_s+\phi)) = \\ &= K(k)(1+\mathcal{V}\cos(2kz_s+\phi)), \end{aligned} \tag{1.25}$$

with $K(k)$ the number of photons detected when the spectrum is not modulated by the cosine. This relation is extremely important since we will find it is valid even for some quantum-OCT implementations (even if the expression for VIS might change).

1.2.4 Signal to Noise Ratio Modeling

Now we can propose a model for the OCT signal-to-noise ratio (SNR), one of the main figures of merit we have to consider for any investigation technique. In OCT, SNR is typically defined as the square of the ratio between the peak amplitude in Fourier-transformed data I and the standard deviation σ [39], i.e.

$$\mathrm{SNR} = (\frac{I}{\sigma})^2. \tag{1.26}$$

Thus, this parameter corresponds to our ability to distinguish the OCT signal from the background. The SNR is often expressed in dB, according to the formula

$$\mathrm{SNR}_{dB} = 20\log\left(\frac{I}{\sigma}\right)\mathrm{dB}. \tag{1.27}$$

The detection process is inextricably connected to the SNR estimation. We assume that the detector is made up of N pixels, with the n-th one detecting the central wave number k_n and a total number of photons

$$N_{out}(k_n) = K(k_n)(1+\mathcal{V}\cos(2k_nz_s+\phi)), \tag{1.28}$$

according to equation 1.25. Referring to [36], we consider each n-th spectrum as a properly normalized square function, such that $\sum_n^N S(k_n) = P_0$. For simplicity, we take $S(k_n) = P_0/N$ for any n. Moreover, we work after proper k value shifting, in such a way that the n-th pixel operates in the range $[(n-1)\Delta k; n\Delta k]$, with $\Delta k = \frac{k_{max}-k_{min}}{N}$. After the shifting, we will have the spectrum completely in the range $[0; 2k_c]$, with k_c the central wavenumber. Eventually, we neglect the additional phase ϕ, which is irrelevant in the following considerations.

The OCT signal is related just to the interference term, in general given by Equation 1.9. Applying it to a single reflecting layer we get

$$N_{sig}(k_n) = \alpha(1-\alpha)\frac{S(k_n)t_I}{h\nu_c}2r_r r_s\cos(2k_n z_s) = \\ = K(k_n)\mathcal{V}\cos\left(2\pi\frac{n}{N}q_s\right), \tag{1.29}$$

with $q_s = \frac{2k_c z_s}{\pi}$.

Applying the FFT to 1.29 (see Appendix A for explicit calculations), we get a fully real OCT signal, having two peaks (symmetric around the 0) with amplitude

$$N_{sig}(n) = I_{OCT} = \frac{1}{2N}K_{tot}\mathcal{V}, \tag{1.30}$$

K_{tot} representing the total number of detected photons. It is worth stressing that this formula is in agreement with the proportionality to r_s found in Equation 1.15, in fact:

$$\frac{1}{2N}K_{tot}\mathcal{V} = \frac{1}{2N}\alpha(1-\alpha)\frac{S(k)t_I}{h\nu_c}(r_r^2+r_s^2) * \frac{2r_r r_s}{r_r^2+r_s^2} \propto r_s. \tag{1.31}$$

At this point, we can consider the noise and define the theoretical shot-noise level. The noise must be considered in the absence of any interferometric signal [36]. In this case, each n-th channel detects a mean number of photons

$$N_{nonint}(n) = K(n) = \frac{K_{tot}}{N}. \tag{1.32}$$

For a sufficiently high number of counts (more than 30 [23]), we can consider the shot noise data in each channel approximately Gaussian, with both mean and variance equal to $N_{nonint}(n)$. We can associate to the shot-noise the random variable $\mathbf{N}(n)$: furthermore, we can easily treat $\mathbf{N}(n)$ as a zero mean Gaussian variable, after a shifting of $N_{nonint}(n)$. The contribution to the OCT spectrum of $\mathbf{N}(n)$ can be calculated by applying the inverse FFT

$$i_n(q) = \frac{1}{N}\sum_{n=0}^{N-1}\mathbf{N}(n)e^{i2\pi qn/N}. \tag{1.33}$$

It can be shown (see Appendices B and C) that the real part $\mathfrak{Re}[i_n(q)]$ and the imaginary part $\mathfrak{Im}[i_n(q)]$ are uncorrelated Gaussian random variables, having equal variances

$$\sigma^2_{\mathfrak{Re}[(i_n(q))]} = \sigma^2_{\mathfrak{Im}[i_n(q)]} = K_{tot}/2N^2. \tag{1.34}$$

We can then find the variance for $|i_n(q)| = \sqrt{\mathfrak{Re}[(i_n(q))]^2 + \mathfrak{Im}[i_n(q)]^2}$, that is a variable distributed accordingly to the Rayleigh distribution with variance (as shown in [40])

$$\sigma^2_{|i_n(q)|} = \frac{K_{tot}}{2N^2}(2-\frac{\pi}{2}). \tag{1.35}$$

Finally, combining Equations 1.30 and 1.35 we find

$$\mathrm{SNR}_{id} = (I_{OCT}/\sigma_{OCT})^2 = \frac{1}{4-\pi}\mathcal{V}^2 K_{tot}. \tag{1.36}$$

Equation 1.36 describes the ideal SNR whenever the number of detected photons can be written as in equation 1.25. It is therefore an important limit to understand how well our OCT setup performs.

1.2.5 Normalization with the non-interference spectrum

As discussed, the result in Equation 1.30 is obtained for a well-normalized rectangular spectrum. However, in a real scenario, $S(k)$ might have any shape, making invalid any generalization. Nonetheless, if we divide the interference spectrum by the non-interference one in the same conditions we get:

$$\frac{N_{out}(k)}{N_{non-interf}(k)} = \Pi(k)(1 + \mathcal{V}\cos(2kz_s + \phi)), \tag{1.37}$$

where $\Pi(k)$ is the rectangular function equal to 1 over its domain. However, this comes at a cost, since we lose the usual proportionality between the signal amplitude and the sample's field reflectivity r_s. If we use a single reference non-interference spectrum, instead, we preserve the proportionality, but the shape of $S(k)$ might change between the two measurements because of the variation of the sample. However, this slow variation should affect the FFT just for the DC component, so it can be easily addressed in the analysis phase.

Dividing by a reference non-interference spectrum is a standard normalization strategy [23][41], which allows the removal of artifacts in the OCT spectrum, making the signal more distinguishable.

1.2.6 Depth range and lateral resolution

Up to now, the axial resolution and the SNR were considered. Two additional figures of merit that must be taken into account to characterize the performance of an OCT setup are the depth range and the lateral resolution.

The depth range is defined as the maximum depth that can be probed, i.e. half of the maximum OPD still detectable in the OCT spectrum. Two physical boundaries dictate the depth range value: the Nyquist condition and the need to resolve the modulation of the interference pattern.

The Nyquist condition requires a value of the sampling frequency high enough to correctly reconstruct the interference pattern. This is, in general, an oscillating function in k-domain, like the one described by Equation 1.25, valid for a single reflecting layer. If

we consider this simplest case, we can notice that the equivalent of the angular frequency is given by $2z_s$. The Nyquist theorem states that, in order to reconstruct the frequency ν of the sampled signal correctly, we need to use a sampling frequency $\nu_s \geq \nu_{Ny} = 2\nu$. In this case, this condition holds in k-domain, therefore

$$\nu_{Ny} = 2\nu = \frac{2z_s}{\pi}. \tag{1.38}$$

Since the sampling frequency in our case is given by the inverse of the sampling period in the k-domain τ_{k_s}, the Nyquist condition becomes

$$\frac{1}{\tau_{k_s}} \geq \frac{2z_s}{\pi}. \tag{1.39}$$

Exploiting $k = \frac{2\pi}{\lambda}$, we get $\tau_{k_s} = \frac{2\pi}{\lambda^2}\tau_{\lambda_s}$, with τ_{λ_s} being the sampling period in λ-domain. Replacing τ_{k_s} expression we find

$$z_s \leq \frac{\lambda^2}{4\tau_{\lambda_s}}. \tag{1.40}$$

Considering N sampled points throughout the bandwidth $\Delta\lambda$ [42], we finally get

$$z_s \leq \frac{1}{4}\frac{\lambda^2}{\Delta\lambda}N. \tag{1.41}$$

The Nyquist condition is not sufficient, though. We have also an additional condition related to the necessity to resolve the average fringe distance in the interference pattern, which provides both another upper limit and a lower limit. The average fringe distance corresponds to the periodicity in k-space, therefore it is given by

$$\tau_k = \frac{1}{\nu_k} = \frac{\pi}{z_s} \tag{1.42}$$

This value must be, at the same time, larger than the spectrometer's resolution but smaller than the probing beam bandwidth [24]. The spectrometer's resolution in k-space is related to the one in the λ-domain as $\delta k_1 = \frac{2\pi}{\lambda^2}\delta\lambda_{sp}$, where $\delta\lambda_{sp}$ is the minimum resolvable spectral distance. More precisely, it is defined as the FWHM of the spectrometer's response function [43]. On the other hand, the probing beam bandwidth in k-domain can be estimated as $\delta k_2 = \frac{2\pi}{\lambda^2}\Delta\lambda$. Therefore, we obtain

$$\begin{aligned} &\delta k_1 \leq \tau_k \leq \delta k_2 \\ &\frac{2\pi}{\lambda^2}\delta\lambda_{sp} \leq \frac{\pi}{z_s} \leq \frac{2\pi}{\lambda^2}\Delta\lambda \\ &\frac{1}{2}\frac{\lambda^2}{\Delta\lambda} \leq z_s \leq \frac{1}{2}\frac{\lambda^2}{\delta\lambda_{sp}} \end{aligned} \tag{1.43}$$

Both conditions 1.41 and 1.43 must be carefully taken into account since they represent fundamental and very general limitations. Nonetheless, they are just theoretical boundaries: an experimental determination of the effective depth range, reconstructing the roll-off curve, is thus indispensable.

The lateral resolution δx is defined as the FWHM of the sample beam's intensity profile function $I(r, z)$ [42], with $z = z_s$. This function describes how the intensity of the beam, which propagates along the z direction, changes according to z and to the radial position r. If we consider the Gaussian beam approximation, i.e.

$$I(r, z) = \frac{P}{\pi w(z)^2/2} e^{-\frac{2r^2}{w(z)^2}} \tag{1.44}$$

where P is the optical power, $w(z)$ the beam radius (it varies owing to diffraction), we thus get [44]

$$\delta x = \sqrt{2 \ln 2} w(z_s) \tag{1.45}$$

In most cases the beam is highly focused, therefore we can take

$$\delta x = \sqrt{2 \ln 2} w_0 \tag{1.46}$$

with w_0 the minimum radius, also called the beam waist [42]. In most cases, the lateral resolution is determined experimentally, performing for instance a knife-edge measurement [23]. This strategy will be deepened in the experimental results.

1.3 Mid-infrared OCT

Classical OCT is optimized to work in the NIR range, more precisely between 700 and 1500 nm. Both detectors and broadband sources operating in this region are available, with high efficiency and relatively low cost. Since the biotissue transparency window goes from approximately 700 to 1300 nm [8], it is easy to explain the success of OCT in biomedical applications. However, the peculiar features of this technique make it extremely promising for any non-destructive testing (NDT) application: the sample is probed just with a light beam, avoiding any contact and granting a reasonably long depth range, remarkable axial and lateral resolutions, fast acquisition rate, and fine detection sensitivity [1]. For this reason, the interest in alternative applications of OCT has recently emerged, ranging from artworks inspection to material characterization, from fluid sensing to strain field characterization [8]. The main constraint to the OCT's success in these fields, especially in key industrial applications like micromanufacturing, is that its high efficiency is limited to the NIR range. The fabrication of ceramic multilayered microdevices, which would deeply benefit from the OCT's features, mostly relies on the usage of highly scattering materials like alumina and zirconia. Thus, standard probing wavelengths up to 1.5 μm can just provide seriously limited penetration depths

[8]. Consonantly, standard OCT proves to be largely ineffective for the investigation of devices based on materials that do not transmit in the NIR range, like Silicon-based and Germanium-based integrated circuits [45] or Silicon carbide components [46].

These severe limitations can be overcome by extending the exploitable range of wavelengths to the MIR region, thus limiting the scattering and accessing the high-transmission range for semiconductors. As already stated in the introduction, this is a considerable scientific challenge, since the current state-of-the-art for both detectors and sources operating in the MIR range is far from being competitive with their NIR counterparts.

It is worth reporting the most notable results demonstrated for MIR OCT "classical" implementations. I use the term "classical" indicating that they rely on developing a standard OCT setup, replacing the ordinary NIR operating components with their MIR equivalent.

The current state-of-the-art implementation was reported by Zorin et al. in [16]. They realized a MIR operating FD-OCT setup, relying on a super-continuous laser as the source and a low-cost $LiTaO_3$ pyroelectric focal linear array to record the spectral interference patterns. Their source emitted in the range $1.1 - 4.4$ μm, reduced to the optimal $3.75 - 4.25$ μm for OCT measurements. The characterization of the performance showed a remarkable sensitivity of 81.7 dB, but limited axial resolution ≈ 50 μm (determined by the coherence length) and depth range ≈ 1.1 mm (related to the spectral resolution and the beam's depth of focus). Finally, they proved the capacity of resolving the back layers in a multilayered ceramic structure, a net advantage with respect to commercially available OCT setups.

Chapter 2

OCT and nonlinear processes

Since the challenges in developing highly efficient detectors and sources operating in the MIR region are fundamental, inevitably dictating severe limitations for the classical implementation performance, most recent studies have focused on a radically different approach. The idea is to circumvent the necessity for such kinds of devices. In the upconversion technique, explained later on in this chapter, the sample is probed in the MIR region, but the back reflected light is upconverted to the visible or NIR region before detection. In OCT with undetected photons technique, instead, this advantage is combined with no necessity to have a MIR operating source as well (the details will be deepened in the next chapter). These counterintuitive results are made possible by the so-called *nonlinear processes*.

2.1 Nonlinear processes

Nonlinear processes are peculiar optical processes that can happen just inside materials for which the induced polarization depends nonlinearly on the electric field strength. This means that the standard equation of linear optics

$$\vec{P}(t) = \epsilon_0 \chi \vec{E}(t), \tag{2.1}$$

where χ is the susceptibility tensor, is no longer valid. To rewrite the polarization, we assume that we can write the optical electric field applied to a certain material as the sum over its frequency components $\vec{E}(\omega_n)$ (referring to [47])

$$\vec{E}(\vec{r}, t) = \sum_n \vec{E}(\omega_n) = \sum_n \vec{E}_n e^{i(\vec{k}_n \vec{r} - \omega_n t)} + \text{c.c.} \tag{2.2}$$

Analogously, we can write the polarization vector as

$$\vec{P}(\vec{r}, t) = \sum_n \vec{P}_n e^{i(\vec{k}_n \vec{r} - \omega_n t)} + \text{c.c.} \tag{2.3}$$

Since the sum is performed over positive frequencies, we can use a simple change of notation to remove the complex conjugate

$$\vec{E}(-\omega_n) = \vec{E}^*(\omega_n). \tag{2.4}$$

We define the first-order susceptibility tensor $\chi^{(1)}$ as the one fulfilling

$$P_i^{(1)}(\omega_n) = \epsilon_0 \sum_j \chi_{ij}^{(1)}(\omega_n) E_j(\omega_n). \tag{2.5}$$

Analogously, we define the second-order susceptibility $\chi^{(2)}$ using

$$P_i^{(2)}(\omega_n + \omega_m) = \epsilon_0 \sum_{jk} \sum_{(nm)} \chi_{ijk}^{(2)}(\omega_n + \omega_m; \omega_n, \omega_m) E_j(\omega_n) E_k(\omega_m). \tag{2.6}$$

In this case, since the amplitude $E(\omega_n)$ is associated with the dependence $e^{-i\omega_n t}$, whereas $E(\omega_m)$ to the $e^{-i\omega_m t}$ one, their product will oscillate at the sum-frequency $\omega_n + \omega_m$, from which the notation. Higher-order susceptibilities can be defined as well, with $\chi^{(3)}$ being a fourth-rank tensor and so on. We can now consider some processes associated with $\chi^{(2)}$.

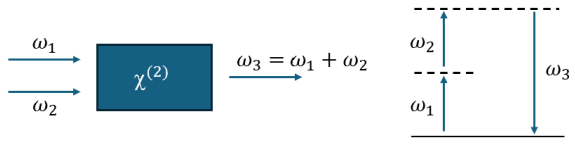

(a) *Geometry and energy-level diagram for the SFG process.*

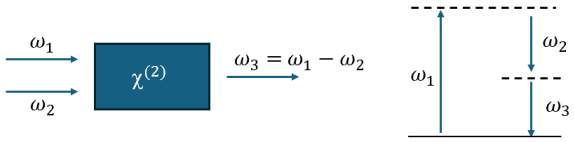

(b) *Geometry and energy-level diagram for the DFG process.*

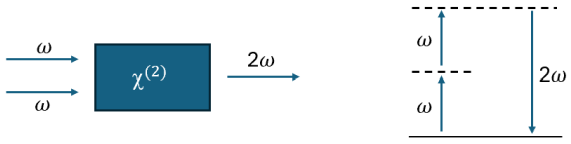

(c) *Geometry and energy-level diagram for the SHG process.*

Figure 2.1: *Summarizing schemes for the main nonlinear processes.*

A summarizing image for all the processes is reported in Figure 2.1:

- Sum-frequency generation: Let the input fields have frequencies ω_1 and ω_2 and the output frequency be $\omega_3 = \omega_1 + \omega_2$. Thus, by applying Equation 2.6 we find [47]

$$P_i^{(2)}(\omega_3) = \epsilon_0 \sum_{jk} [\chi_{ijk}^{(2)}(\omega_3; \omega_1, \omega_2) E_j(\omega_1) E_k(\omega_2) + \chi_{ijk}^{(2)}(\omega_3; \omega_2, \omega_1) E_j(\omega_2) E_k(\omega_1)]. \tag{2.7}$$

In most cases, $\chi^{(2)}$ is characterized by intrinsic permutation symmetries [47], therefore we assume for simplicity

$$\chi^{(2)}_{ijk}(\omega_3;\omega_1,\omega_2) = \chi^{(2)}_{ijk}(\omega_3;\omega_2,\omega_1), \tag{2.8}$$

from which we find the final expression for the polarization associated with the process

$$P^{(2)}_i(\omega_3) = 2\epsilon_0 \sum_{jk} \chi^{(2)}_{ijk}(\omega_3;\omega_1,\omega_2) E_j(\omega_1) E_k(\omega_2). \tag{2.9}$$

Sum-frequency generation (SFG) corresponds to the frequency sum-up of the two input waves. One important application is the generation of tunable ultraviolet radiation, by exploiting the SFG between two input beams in the visible range.

- Second-harmonic generation: let us consider now the special SFG case with $\omega_1 = \omega_2$, $\omega_3 = 2\omega_1$. We find

$$P^{(2)}_i(\omega_3) = \epsilon_0 \sum_{jk} \chi^{(2)}_{ijk}(2\omega_1;\omega_1,\omega_1) E_j(\omega_1) E_k(\omega_1), \tag{2.10}$$

losing the 2 factor (this result might seem counterintuitive, but it is just a consequence of the convention from [47] that $\chi^{(2)}_{ijk}(\omega_3;\omega_1,\omega_2)$ must approach $\chi^{(2)}_{ijk}(\omega_3;\omega_1,\omega_1)$ for ω_1 approaching ω_2). SHG can be experimentally extremely efficient. That is why it is commonly used to convert the wavelength of a fixed-frequency laser to a different region of the electromagnetic spectrum [47].

- Difference-frequency generation: DFG is an alternative form of SFG, in which the output frequency is $\omega_3 = \omega_1 - \omega_2$. In this case, we will have

$$P^{(2)}_i(\omega_3) = \epsilon_0 \sum_{jk} [\chi^{(2)}_{ijk}(\omega_3;\omega_1,\omega_2)] E_j(\omega_1) E^*_k(\omega_2) + \chi^{(2)}_{ijk}(\omega_3;\omega_2,\omega_1) E^*_j(\omega_2) E_k(\omega_1)]. \tag{2.11}$$

Indices jk are still dummy in this expression, therefore if $\chi^{(2)}$ symmetry is preserved we find

$$P^{(2)}_i(\omega_3) = 2\epsilon_0 \sum_{jk} \chi^{(2)}_{ijk}(\omega_3;\omega_1,\omega_2) E_j(\omega_1) E^*_k(\omega_2). \tag{2.12}$$

All these processes can happen only if they satisfy both energy and momentum conservation

$$\begin{cases} \hbar\omega_3 = \hbar\omega_1 + \hbar\omega_2 \\ \hbar\vec{k_3} = \hbar\vec{k_1} + \hbar\vec{k_2} \end{cases}, \tag{2.13}$$

usually referred to as *phase-matching conditions* in this context. A more detailed explanation of the physical reason behind the phase-matching conditions will be given in the next section.

Nonlinear processes will be significant just if the $\chi^{(2)}$ term is non-negligible. A rough estimation of $\chi^{(2)}$ order of magnitude can be obtained by assuming that the nonlinearity has an electronic origin. In this case, we expect the lowest order correction term $\vec{P}^{(2)}$ to be comparable with the linear response $\vec{P}^{(1)}$ when the intensity of the applied field is of the order of the atomic electric field $E_{at} = \frac{e}{4\pi\epsilon_0 a_0^2}$, with a_0 the Bohr radius [47]. Therefore, we have

$$\chi^{(2)} \approx \chi^{(1)}/E_{at}. \tag{2.14}$$

Since for condensed matter $\chi^{(1)}$ is in the order of the unity, we get

$$\chi^{(2)} \approx 2 \times 10^{-12}\text{m/V}, \tag{2.15}$$

which is not far from experimentally determined values. An important result can be also demonstrated by analyzing the symmetry properties of the $\chi^{(2)}$ tensor: it vanishes identically for all media that display inversion symmetry, like liquids, gases, amorphous solids, or many crystals. That is why noncentrosymmetric crystals play a crucial role in quantum optics.

We have seen that in nonlinear materials the response of the medium to the incoming radiation can cause the development of new frequency components, not present in the input field. The physical reason can be qualitatively described like this: when the material is subject to the external field, electrical charges with opposite signs rearrange forming some induced dipoles, which oscillate according to the incoming radiation [48]. In a nonlinear medium, their response will be nonlinear, therefore containing components at new frequencies (for example, at $\omega_3 = \omega_1 + \omega_2$ for SFG). In most cases, each dipole would produce its independent radiation pattern, without interacting with the surrounding ones. However, if the relative phasing of the dipoles is correct (phase-matching conditions), all the radiated fields will superimpose constructively, determining the formation of a beam with a well-defined frequency, different from the input ones [48]. To better understand the phase-matching condition, a precise description of the wave propagation inside the nonlinear medium is necessary.

2.1.1 Wave propagation in nonlinear optical media and phase-matching conditions

The main references for this subsection will be [48] and [49]. In particular, I will consider just the SFG process, since it is the one of main interest for my application (and the more general one). Let us consider the Maxwell equations inside the nonlinear medium,

for regions without free charges or free currents

$$\begin{cases} \nabla \vec{D} & = 0 \\ \nabla \vec{B} & = 0 \\ \nabla \times \vec{E} & = -\frac{\partial \vec{B}}{\partial t} \\ \nabla \times \vec{H} & = \frac{\partial \vec{D}}{\partial t} \end{cases} \tag{2.16}$$

with

$$\vec{B} = \mu_0 \vec{H} \quad , \vec{D} = \epsilon_0 \vec{E} + \vec{P}. \tag{2.17}$$

In order to find the wave propagation equation, we can apply the curl operator to the rotor of the electric field, getting

$$\nabla \times \nabla \times \vec{E} = -\nabla \times \frac{\partial \vec{B}}{\partial t} = -\frac{\partial}{\partial t} \nabla \times \vec{B}. \tag{2.18}$$

By combining Equations 2.16 and 2.17 and remembering $c^2 = 1/\epsilon_0 \mu_0$ we find

$$\nabla^2 \vec{E} - \frac{1}{c^2} \frac{\partial^2}{\partial t^2} \vec{E} = \frac{1}{\epsilon_0 c^2} \frac{\partial^2 \vec{P}}{\partial t^2}. \tag{2.19}$$

This is the wave propagation equation inside a nonlinear optical medium, where the polarization can be decomposed in its linear and nonlinear components as

$$\vec{P} = \vec{P}^{(L)} + \vec{P}^{(NL)} \tag{2.20}$$

or alternatively as

$$\nabla^2 \vec{E} - \frac{1}{\epsilon_0 c^2} \frac{\partial^2}{\partial t^2} \vec{D} = 0 \tag{2.21}$$

with

$$\vec{D} = \epsilon_0 \vec{E} + \vec{P} = \epsilon_0 \vec{E} + \vec{P}^L + \vec{P}^{NL} = \vec{D}^{(1)} + \vec{P}^{(NL)} \tag{2.22}$$

This final form is particularly useful in the case of a lossless, dispersionless medium, because it allows us to easily write $\vec{D}^{(1)} = \epsilon_0 \epsilon^{(1)} \vec{E}$ introducing the frequency-independent dielectric tensor $\epsilon^{(1)}$ (scalar for an isotropic material). Therefore, we find the equation

$$-\nabla^2 \vec{E} + \frac{\epsilon^{(1)}}{c^2} \frac{\partial^2 \vec{E}}{\partial t^2} = -\frac{1}{\epsilon_0 c^2} \frac{\partial^2 \vec{P}^{(NL)}}{\partial t^2}. \tag{2.23}$$

For a dispersive medium, Equation 2.23 must hold for all frequency components. Thus,

$$\nabla^2 \vec{E}(\omega_n) - \frac{\epsilon^{(1)}(\omega_n)}{c^2} \frac{\partial^2 \vec{E}(\omega_n)}{\partial t^2} = \frac{1}{\epsilon_0 c^2} \frac{\partial^2 \vec{P}^{(NL)}}{\partial t^2}. \tag{2.24}$$

We can now build a model for SFG searching a solution for Equation 2.24, with $\vec{P}^{(NL)} \approx \vec{P}^{(2)}$. We will consider the input beams collimated, monochromatic, and continuous for simplicity, propagating along the z direction.

If we have an SFG process with input frequencies ω_1 and ω_2, output $\omega_3 = \omega_1 + \omega_2$, each component must satisfy the propagation equation, in particular the component

$$\vec{E}_3(z,t) = E_3(z)\hat{z}e^{i(k_3 z - \omega_3 t)} + \text{c.c.} \tag{2.25}$$

(with standard definitions $k_3 = \frac{n_3\omega_3}{c}$, $n_3^2 = \epsilon^{(1)}(\omega_3)$, $\hat{z}$ the unit vector along z-direction). The component $\vec{P}_3$ of the polarization vector will be given by $\vec{P}_3^{(2)}(z,t) = P_3^{(2)}(z)\hat{z}e^{i((k_1+k_2)z-\omega_3 t)}+$ c.c defined accordingly to Equation 2.9, i.e. with

$$P_3^{(2)}(z) = 2\epsilon_0\chi^{(2)}E_1(z)E_2(z) = 4\epsilon_0 d_{eff}E_1(z)E_2(z), \tag{2.26}$$

introducing $d_{eff} = \frac{1}{2}\chi^{(2)}$. Using Equation 2.26 inside 2.24, we find

$$\frac{\partial^2 E_3}{\partial z^2} + 2ik_3\frac{\partial E_3}{\partial z} = -\frac{4d_{eff}\omega_3^2}{c^2}E_1E_2e^{i(k_1+k_2-k_3)z}. \tag{2.27}$$

Usually, the amplitude $E_3(z)$ slowly depends on the coordinate z, thus we can neglect the first term. We finally find

$$\frac{\mathrm{d}E_3}{\mathrm{d}z} = \frac{2id_{eff}\omega_3^2}{k_3c^2}E_1E_2e^{i\Delta kz}, \tag{2.28}$$

where we have introduced the wavevector mismatch

$$\Delta k = k_1 + k_2 - k_3. \tag{2.29}$$

If we have $\Delta k = 0$, the perfect phase matching condition, the amplitude E_3 will increase linearly with z. If the condition is not perfectly satisfied, we have to perform the integration of the exponential term over the length of the crystal L, finding

$$E_3(L) = \frac{2id_{eff}\omega_3^2E_1E_2}{k_3c^2}(\frac{e^{i\Delta kL}-1}{i\Delta k}). \tag{2.30}$$

If we calculate the intensity $I = |E|^2$ we get

$$I_3 = \frac{8d_{eff}^2\omega_3^2I_1I_2}{n_1n_2n_3\epsilon_0c^2}L^2\mathrm{sinc}^2(\frac{\Delta kL}{2}). \tag{2.31}$$

The wavevector mismatch effect is thus completely described by the sinc^2 factor, which is plotted in figure 2.2.

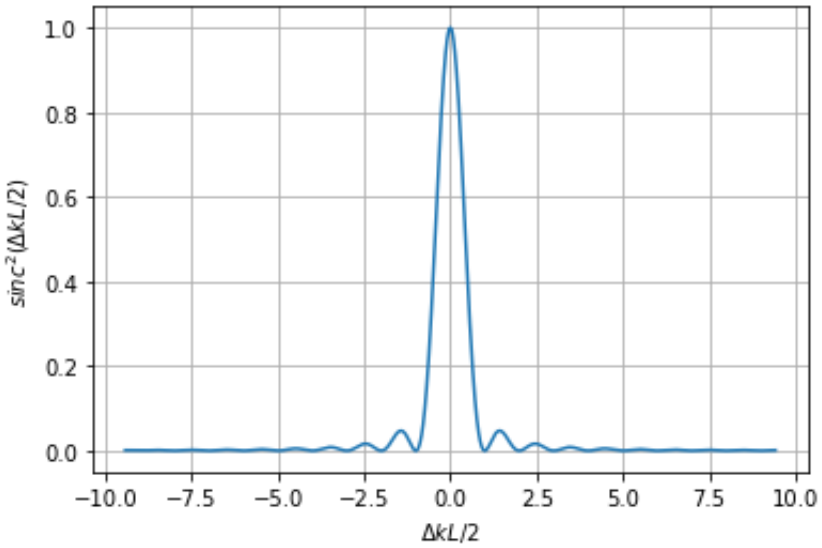

Figure 2.2: *Plot of the* sinc^2 *function, describing the effect of the wavevector mismatch in the intensity of the SFG process.*

Experimentally, perfect phase-matching is thus described by

$$\begin{cases} \omega_3 = \omega_1 + \omega_2 \\ \frac{n_3\omega_3}{c} = \frac{n_1\omega_1}{c} + \frac{n_2\omega_2}{c} \end{cases} . \tag{2.32}$$

For most materials, both equalities cannot be achieved simultaneously, since in normal dispersion conditions we have that $\omega_1 < \omega_2 < \omega_3$ implies $n_1(\omega_1) < n_2(\omega_2) < n_3(\omega_3)$. This operative condition is possible just for birefringent crystals, which are characterized by two (uniaxial crystal) or three (biaxial crystal) different refractive indices along different directions [49].

2.1.2 Parametric down-conversion

Parametric down-conversion (PDC) is another fundamental nonlinear process. In this case, a photon, called *pump*, spontaneously converts into a pair of entangled photons each one at a lower energy, referred to as *signal* and *idler*. The corresponding diagram is reported in Figure 2.3.

The process must fulfill the usual phase-matching conditions

$$\begin{cases} \omega_p = \omega_i + \omega_s \\ \Delta\vec{k} = \vec{k_p} - \vec{k_i} - \vec{k_s} = 0 \end{cases} . \tag{2.33}$$

The discovery of PDC was the final achievement of a series of fundamental theoretical [50][51][52] and experimental [53][54][55][56]works, published between the 1960s and

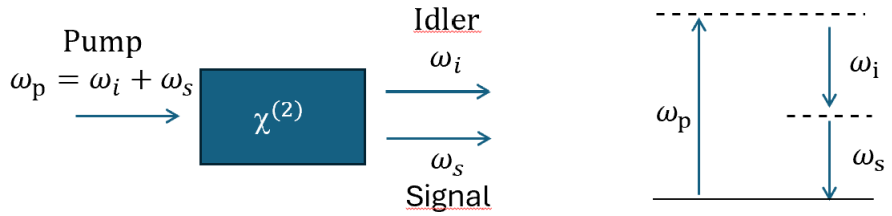

Figure 2.3: *Diagram for the PDC process. An incoming photon with frequency ω_p decays into a couple of photons at lower energies (idler and signal).*

1970s. Since then, this process has become the essential backbone of many quantum optics experiments in a huge variety of different fields, like quantum metrology [57], quantum cryptography [58], and quantum computing [59]. PDC is intrinsically different from the processes just described because it implies the spontaneous, "ex-nihilo" creation of an additional photon in a particular mode. At first sight, it might simply seem the reverse-time process of SFG. However, this statement is misleading, because it neglects some additional features of PDC related to its purely quantum nature. In fact, as I will show in the next subsection, a classical model for this process is impossible.

2.1.3 Parametric amplification and non-classicality of parametric down-conversion

To prove that PDC cannot be described in the classical framework, we start again from Equation 2.24, but using as outputs $\vec{E}_1(z,t)$ and $\vec{E}_2(z,t)$. By doing so, we find the differential equations

$$\frac{\mathrm{d}E_1}{\mathrm{d}z} = \frac{2id_{eff}\omega_1^2}{k_1c^2}E_3E_2^*e^{-i\Delta kz} \tag{2.34}$$

$$\frac{\mathrm{d}E_2}{\mathrm{d}z} = \frac{2id_{eff}\omega_2^2}{k_2c^2}E_3E_1^*e^{-i\Delta kz}. \tag{2.35}$$

They can be solved assuming perfect phase-matching, finding the relations [49]

$$E_2(z) = i\sqrt{\frac{\omega_2 n_1}{\omega_1 n_2}}\frac{E_3}{|E_3|}E_1^*(0)\sinh(\alpha z) \tag{2.36}$$

$$E_1(z) = E_1(0)\cosh(\alpha z) \tag{2.37}$$

$$\alpha = \frac{\chi^{(2)}|E_3|}{c}\sqrt{\frac{\omega_2\omega_1}{n_2n_1}}. \tag{2.38}$$

These results mean that $E_2(z)$ and $E_1(z)$ are different from 0 if and only if $E_1(0)$ is non-null. Consequently, the classical process having E_1 and E_2 as outputs necessarily needs E_3 and E_1 as inputs. The phenomenon described in this way, whose scheme is represented in Figure 2.4, is thus something inherently different from PDC, normally called *parametric amplification*.

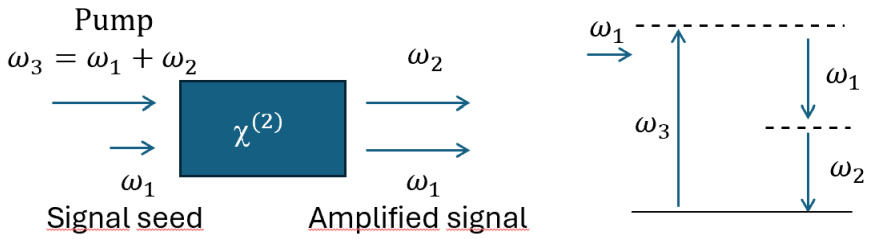

Figure 2.4: *Diagram for the parametric amplification process. The amplification of the signal can happen only if we have a non-null seeded signal as input.*

Parametric amplification is a key process in a large plethora of fields, including spectroscopy, generation of ultrafast laser pulses, quantum communication, and nonlinear microscopy.

2.1.4 Fock states and creation/annihilation operators

Before describing the PDC process, it is worth recalling some fundamental concepts in quantum optics.

The electromagnetic field propagation is described by Maxwell's equations, with each independent solution being called *optical mode* [60]. If we rewrite the electromagnetic radiation using its Fourier expansion for all the accessible optical modes and solve the propagation equation, it can be shown that each component can be treated equivalently to a quantum harmonic oscillator [61]. Thus, the number of photons for each mode completely describes the transport of energy and information [60]. We can adopt the second quantization formalism to describe a generic multi-photon ensemble, using the so-called Fock states in the form $\left|n_1, n_2, ..., n_\mu, ...\right\rangle$, where each n_μ indicates the occupation number for the μ-th optical mode [62]. These Fock states form a basis for the Hilbert space of the electromagnetic field. Moreover, since each optical mode can be treated equivalently to a quantum oscillator, we can introduce the associated creation/annihilation operators $\hat{a}_\mu^\dagger$, $\hat{a}_\mu$. These operators can be easily applied to the Fock states, according to the relations

$$\hat{a}_\mu^\dagger \left|n_1, n_2, ..., n_\mu, ...\right\rangle = \sqrt{n_\mu + 1} \left|n_1, n_2, ..., n_\mu + 1, ...\right\rangle, \tag{2.39}$$

$$\hat{a}_\mu \left|n_1, n_2, ..., n_\mu, ...\right\rangle = \sqrt{n_\mu} \left|n_1, n_2, ..., n_\mu - 1, ...\right\rangle, \tag{2.40}$$

and their commutation relations are

$$[\hat{a}_\mu, \hat{a}_{\mu'}] = [\hat{a}^\dagger_\mu, \hat{a}^\dagger_{\mu'}] = 0, \tag{2.41}$$

$$[\hat{a}_\mu, \hat{a}^\dagger_{\mu'}] = \delta_{\mu\mu'}. \tag{2.42}$$

The creation/annihilation operators can be used to write explicitly the Fourier components of the electromagnetic field. For simplicity, just transversal modes are usually considered, assuming that the optical mode μ is uniquely defined by the wavevector $\vec{k}_\mu$. In this case, we can write the operators associated to the electromagnetic field as

$$\hat{E}^{(+)}_\mu(\vec{r}, t) = \sum_\mu C_{\vec{k}_\mu} e^{i(\vec{k}_\mu \vec{r} - \omega_\mu t)} \hat{a}_{\vec{k}_\mu}(\vec{r}), \tag{2.43}$$

$$\hat{E}^{(-)}_\mu(\vec{r}, t) = (\hat{E}^{(+)}_\mu(\vec{r}, t))^\dagger, \tag{2.44}$$

with $C_{\vec{k}_\mu}$ being the proper decomposition coefficient.

Eventually, we also introduce the photon-number operator $\hat{N}_\mu$ for each mode μ. This is defined by

$$\hat{a}^\dagger_\mu \hat{a}_\mu = \hat{N}_\mu, \tag{2.45}$$

and its action on Fock states is given by

$$\hat{N}_\mu \left| n_1, n_2, ..., n_\mu, ... \right\rangle = n_\mu \left| n_1, n_2, ..., n_\mu, ... \right\rangle. \tag{2.46}$$

For conciseness, we can also introduce the notation

$$|n\rangle_\mu = \left| 0, 0.., n_\mu, 0, ... \right\rangle, \tag{2.47}$$

$$|0\rangle = |vac\rangle = |0, 0, ...\rangle. \tag{2.48}$$

$$\tag{2.49}$$

2.1.5 Quantum description: low-gain vs high-gain

At this point, we can introduce the general PDC Hamiltonian [63]

$$\hat{H}_{\mathrm{PDC}} = \int \mathrm{d}^3 r \chi^{(2)}(\vec{r}) \hat{E}^{(+)}_p(\vec{r}, t) \hat{E}^{(-)}_s(\vec{r}, t) \hat{E}^{(-)}_i(\vec{r}, t) + \mathrm{H.c.} \tag{2.50}$$

simultaneously describing both PDC and SFG processes and where various operators $\hat{E}^{(+,-)}_{p,s,i}$ are defined according to the equations 2.43 and 2.44 (where the sum can be converted to an integral over $\mathrm{d}\vec{k}_{\mu_{p,s,i}}$ if the modes are dense enough in k-space). In most cases, the pump is assumed to be a classical plane-wave [64] propagating along the z axis, notably simplifying the calculation. It is important to highlight that, in the general expression of the Hamiltonian, both $\chi^{(2)}$ and the various creation/annihilation

operators $\hat{a}$ are functions of the position. This is fundamental to understand how the crystal structure affects the process.

The general Hamiltonian allows us to describe the evolution of the creation/annihilation operators solving the Heisenberg equations. Before doing so, we adopt a more comfortable notation (valid for undepleted pump, collinearity of the process, conservation of the polarization): we write the frequencies of idler and signal as $\omega_i = \omega_0 + \Omega$, $\omega_s = \omega_0 - \Omega$ respectively, introducing $\omega_0 = \omega_p/2$ and the detuning frequency Ω. The phase mismatch will be then given by $\Delta(\Omega) = k_p - k(\Omega) - k(-\Omega)$. The field operators $E^{(+)}_{s,i}(z,t)$ will then satisfy [65]

$$E^{(+)}_{s,i}(z,t) \propto \int \hat{a}(\pm\Omega, z) e^{i(k(\pm\Omega)z - (\omega_0 \pm \Omega)t)} \mathrm{d}(\pm\Omega), \tag{2.51}$$

where the sum in Equation 2.43 can be converted into an integral since the modes are densely packed in k-space, $\hat{a}(+\Omega, z) = \hat{a}_{\vec{k}_s}$, and $\hat{a}(-\Omega, z) = \hat{a}_{\vec{k}_i}$. An important theoretical result is that the explicit dependence of each $\hat{a}$ on z and $\Delta(\Omega)$ can be found by solving the following system of differential equations [65]:

$$\begin{cases} \frac{\partial \hat{a}(\Omega,z)}{\partial z} & = \chi^{(2)}(z) E_p \hat{a}^\dagger(-\Omega, z) e^{i\Delta(\Omega)z} \\ \frac{\partial \hat{a}^\dagger(-\Omega,z)}{\partial z} & = \chi^{(2)*}(z) E_p^* \hat{a}(\Omega, z) e^{-i\Delta(-\Omega)z} \end{cases}. \tag{2.52}$$

This system admits a single solution when we take into account known boundary conditions at $z = 0$, expressable in the form of special unitary transformations (called Bogolyubov transformations) for the down-converted photons creation and annihilation operators. More precisely, these transformations are in the form [65]

$$\begin{cases} \hat{a}(\Omega, L) = U(\Omega)\hat{a}(\Omega, 0) + V(\Omega)\hat{a}^\dagger(-\Omega, 0) \\ \hat{a}^\dagger(\Omega, L) = U^*(\Omega)\hat{a}^\dagger(\Omega, 0) + V^*(\Omega)\hat{a}(-\Omega, 0) \end{cases}, \tag{2.53}$$

where L is the length of the nonlinear crystal, $U(\pm\Omega)$ and $V(\pm\Omega)$ are four complex numbers defining the transformation. These numbers can be found solving in the complex domain the system 2.52. Therefore, in general, they are dependent on $\chi^{(2)}(z)$, $\Delta(\Omega)$, E_p, and L. Additionally, unitarity requires $|U(\pm\Omega)|^2 - |V(\pm\Omega)|^2 = 1$, $U(\Omega/V(\Omega) = U(-\Omega)/V(-\Omega)$. Thus, the degrees of freedom of the solution reduce up to four purely real parameters. [64] showed that we can use

$$\begin{aligned} r(\Omega) &= \ln\big(|U(\Omega)| + |V(\Omega)|\big), \\ \psi^0(\Omega) &= \frac{1}{2}\arg[U^{-1}(\Omega)V(\Omega)], \\ \psi^L(\Omega) &= \frac{1}{2}\arg[U(\Omega)V(-\Omega)], \\ \kappa(\Omega) &= \frac{1}{2}\arg[U(\Omega)U^{-1}(-\Omega)]. \end{aligned} \tag{2.54}$$

$r(\Omega)$ takes the name of *squeezing parameter* or *parametric gain*, the other terms are called *squeezing angles*. It is important to notice that r,ψ^0,ψ^L are even functions of Ω, while κ is odd. The physical meaning of r is a key aspect and will be soon clarified. Rewriting $U(\Omega)$ and $V(\Omega)$ in terms of these new variables, we find [65]

$$U(\Omega) = e^{i[\psi^L(\Omega)-\psi^0(\Omega)+\kappa(\Omega)]} \cosh r(\Omega), \tag{2.55}$$

$$V(\Omega) = e^{i[\psi^L(\Omega)+\psi^0(\Omega)+\kappa(\Omega)]} \sinh r(\Omega). \tag{2.56}$$

We can finally calculate the expected output photon number corresponding to the detuning frequency Ω. This is defined by the expectation number $\langle N(\Omega, L\rangle) = N(\Omega)\delta(\Omega - \Omega^{'}) = \langle \hat{a}^{\dagger}(\Omega, L)\hat{a}(\Omega^{'}, L)\rangle$. Substituting Equations 2.55,2.56 into 2.53, and using the usual commutation relation $[\hat{a}(\Omega, z)\hat{a}^{\dagger}(\Omega^{'}, z)] = \delta(\Omega - \Omega^{'})$, we can find (see the Appendix D for details)

$$\langle N(\Omega, L)\rangle = N_{s,i}(\Omega) = \sinh^2 r(\Omega), \tag{2.57}$$

which defines the output spectra $S(\omega_0 \pm \Omega)$ (provided normalization dividing by $\max\langle N_{s,i}\rangle$[26]).

The parametric gain r is then directly related to the number of photons in each mode after the PDC process. Moreover, if we wrote explicitly all dependences we would have $r = r(\Omega, \Delta(\Omega), \chi^{(2)}(z), E_p, L)$ and, in particular, it can be shown that $r \propto E_p$ [65]; this shows how the crystal design, the pump, and the phase-matching conditions affect the squeezing parameter and, so, the shape of the PDC spectra.

In the limit of $r \to 0$ we have that $\langle N\rangle \to r^2$: this condition corresponds to the so-called *low-gain regime*, or *spontaneous parametric down-conversion*. On the contrary, if $r \gg 1$. The dependence is purely exponential ($\propto \sinh^2(r)$. This condition corresponds to the *high-gain regime*. A comparison between r^2 and $\sinh^2 r$ functions is reported in Figure 2.5 for clarity.

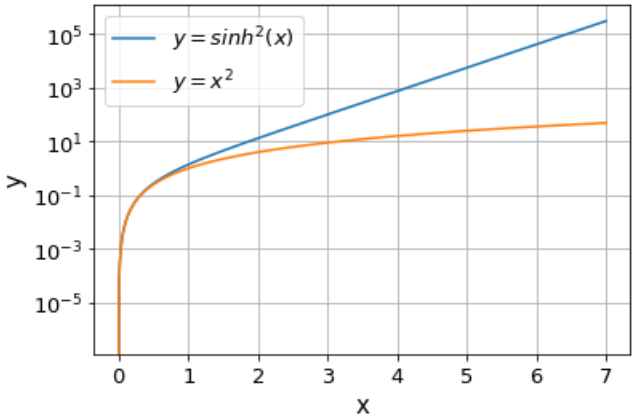

Figure 2.5: *Comparison of functions* $y = x^2$ *and* $y = \sinh^2 x$

The typical parametric gain in SPDC is of the order of $10^{-3} - 10^{-4}$ for CW lasers. In this case, the number of generated photons inside the crystal is too small to increase the

generation rate, which remains constant along the whole crystal [26]. If the gain becomes bigger than 1 (a good reference for experimental value is [66], in which the parametric gain is found to be $3.9 < r < 6.5$), instead, the large photons number generated at the beginning of the crystal further enhance the generation rate, seeding the production at the end [26]. A schematic representation comparing the generation of photons in the low-gain and high-gain regimes is reported in Figure 2.6.

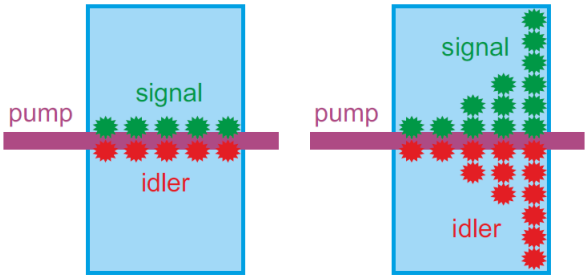

Figure 2.6: *A pictorial comparison between the generation photons in low-gain regime (left) and high-gain regime (right). Taken from [26].*

I would like to make some final considerations about the SPDC limit $r \to 0$. Since r^2, associated with the number of down-converted photons, is $\ll 1$, we might consider it as the probability associated with the PDC process happening. I will exploit this analogy later in the context of the SU(1,1) interferometer. Moreover, $\langle N \rangle \to r^2 \propto |E_p|^2$, thus its intensity is proportional to the pump power.

We can now summarize the most important conclusions:

- All the PDC processes can be mathematically described by introducing the parametric gain $r(\Omega)$. In particular, the number of down-converted photons (directly related to the output spectrum) is given by $\sinh^2(r(\Omega))$;
- The parameter $r(\Omega)$, in general, depends on the detuning frequency, the phase-matching conditions, the geometry and length of the crystal, and the pump intensity ($I_p \propto |E_p|^2$);
- Low-gain PDC is characterized by a low number of generated photons per mode. Mathematically, this corresponds to a low parametric gain value, which allows us to work in the limit $\sinh^2 r \to r^2$. Its intensity is linearly dependent on the pump intensity;
- High-gain PDC is characterized by a large number of photons per mode, a condition mathematically corresponding to a large r. In this case, the high number of generated photons at the beginning of the crystal further enhances the total generation rate.

2.2 Quasi-phase-matching and aperiodically poled nonlinear crystals

To have a better understanding of the role played by the crystal design structure in determining the parametric gain r, we will focus on the class of nonlinear crystals effectively involved in the project: aperiodically poled nonlinear crystals with quasi-phase-matching (QPM). For this purpose, I will mainly refer to [65] and supplementary material in [28]. Let us recall the notation used in the previous subsection, in particular, the phase mismatch

$$\Delta(\Omega) = k_p - k(\Omega) - k(-\Omega). \tag{2.58}$$

The PDC process can happen just for those frequencies Ω that fulfill the phase-matching condition

$$\Delta(\Omega) \approx 0 \tag{2.59}$$

In most cases, this results in a narrow-band spectrum of available frequencies, which is inappropriate for OCT. Suppose now it is impossible to achieve phase-matching for a certain frequency $\omega_0 + \Omega$ in a determined nonlinear crystal. Starting from its original structure, we can design and produce a layered structure characterized by periodical $\chi^{(2)}$, with each layer having $\Lambda/2$ width.To achieve this, it is fundamental to provide an inversion of the crystal structure for each subsequent layer (the resulting structure is illustrated in Figure 2.7).

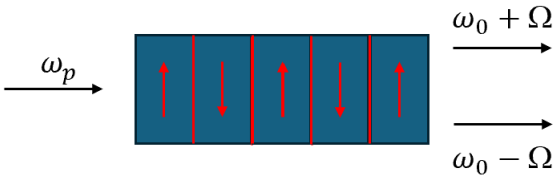

Figure 2.7: *Schematic representation of a periodically poled nonlinear crystal. The red arrows represent the inversion of the crystal structure for each subsequent layer. The black arrows, instead, represent pump, signal, and idler photons.*

In this way, the $\chi^{(2)}$ gets the form [65]

$$\chi^{(2)}(z) = \chi_0 \mathrm{sgn}(\sin Kz) = \frac{-i\chi_0}{\pi} \sum_{n=-\infty}^{+\infty} \frac{1-(-1)^n}{n} e^{inKz}, \tag{2.60}$$

with $K = \frac{2\pi}{\Lambda}$ being the spatial frequency of this artificial grating, usually called *inverse grating vector*, and the second equality corresponding to the Fourier series expansion. On the contrary, Λ describes the spatial period.

The QPM method involves choosing the appropriate K such that

$$K = \Delta(\Omega). \tag{2.61}$$

Substituting Equation 2.60 into the system 2.52, we find

$$\begin{cases} \frac{\partial \hat{a}(\Omega,z)}{\partial z} & = \sum_{n=-\infty}^{+\infty} \frac{-i\chi_0}{\pi} \frac{1-(-1)^n}{n} E_p \hat{a}^\dagger(-\Omega, z) e^{i(\Delta(\Omega)+n\Delta(\Omega))z} \\ \frac{\partial \hat{a}^\dagger(-\Omega,z)}{\partial z} & = \sum_{n=-\infty}^{+\infty} \frac{i\chi_0^*}{\pi} \frac{1-(-1)^n}{n} E_p^* \hat{a}(\Omega, z) e^{-i(\Delta(-\Omega)+n\Delta(-\Omega))z}, \end{cases} \tag{2.62}$$

where the phase-mismatch is compensated just for $n = -1$, while all other terms in n become negligible [65].

Quite several techniques to produce these kinds of periodically oriented crystals exist [67], e.g. the stacking of different nonlinear crystals [68] or the periodic implantations of ions [69]. The most popular method relies on the nonlinear crystal to be ferroelectric. In this case, we can apply a time-constant external field with, in principle, any desired spatial periodicity. For its ferroelectric properties, the crystal will then rearrange its internal structure accordingly, keeping it when the external field is removed. Crystals fabricated in this way are called periodically poled crystals.

The same building procedure can allow us to achieve a non-constant grating profile along the crystal, i.e. $K = K(z)$. This way, different parts of the crystals will show QPM at different frequencies. These structures are called *aperiodically poled crystals*, as the apKTP crystal employed in my project (Figure 2.8 shows the general scheme for their structure).

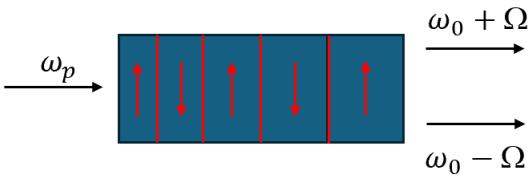

Figure 2.8: *Schematic representation of an aperiodically poled nonlinear crystal.*

Mathematical modeling is possible when the spatial frequency modulation is weak, that is the width $\Lambda(z)$ is a slowly varying function in z. In this case, we can write the

$\chi^{(2)}$ as

$$\chi^{(2)}(z) = \chi_0 \mathrm{sgn}[\sin \int_0^z K(z^{'})\mathrm{d}z^{'}] = \\ \approx \frac{-i\chi_0}{\pi} \sum_{n=-\infty}^{+\infty} \frac{1-(-1)^n}{n} e^{in\int_0^z K(z^{'})\mathrm{d}z^{'}}. \tag{2.63}$$

If we proceed as above to rewrite the system 2.52, considering just the $n = -1$ term, we find

$$\begin{cases} \frac{\partial \hat{a}(\Omega,z)}{\partial z} & = \frac{-i\chi_0 E_p}{\pi}(-2)\hat{a}^{\dagger}(-\Omega,z)e^{i(\Delta(\Omega)z - \int_0^z K(z^{'})\mathrm{d}z^{'})} \\ \frac{\partial \hat{a}^{\dagger}(-\Omega,z)}{\partial z} & = \frac{i\chi_0^* E_p^*}{\pi}(-2)\hat{a}(\Omega,z)e^{-i(\Delta(-\Omega)z - \int_0^z K(z^{'})\mathrm{d}z^{'})} \end{cases}. \tag{2.64}$$

Introducing $\xi = \frac{2\chi_0 E_p}{\pi}$ we finally have

$$\begin{cases} \frac{\partial \hat{a}(\Omega,z)}{\partial z} & = +i\xi\hat{a}^{\dagger}(-\Omega,z)e^{i(\Delta(\Omega)z - \int_0^z K(z^{'})\mathrm{d}z^{'})} \\ \frac{\partial \hat{a}^{\dagger}(-\Omega,z)}{\partial z} & = -i\xi^*\hat{a}(\Omega,z)e^{-i(\Delta(-\Omega)z - \int_0^z K(z^{'})\mathrm{d}z^{'})} \end{cases}. \tag{2.65}$$

This system can be solved (considering boundary conditions at $z = 0$) as already described in the previous subsection. In particular, it can be shown that the complex numbers characterizing the Bogolyubov transformation are in the form [65]

$$U(\Omega) \propto e^{i[k(\Omega) - k_0 + \frac{1}{2}\Delta(\Omega)]L - \frac{i}{2}\int_0^L K(z)\mathrm{d}z}, \tag{2.66}$$

$$V(\Omega) \propto e^{i[k(\Omega) - k_0 + \frac{1}{2}\Delta(\Omega)]L - \frac{i}{2}\int_0^L K(z)\mathrm{d}z}. \tag{2.67}$$

2.3 Upconversion mid-infrared OCT

Nonlinear processes guarantee the possibility of converting the wavelength of an optical beam. This can be an extremely useful feature to achieve efficient MIR OCT, since one of the main issues is related to the difficulties in the direct (or homodyine) detection of MIR radiation. More specifically, upconversion MIR OCT relies on the upconversion of the probing wavelength (in the MIR range) to the ordinary NIR range, allowing us to use ordinary detectors to measure the interference patterns. As explained previously, the upconversion can be achieved by exploiting an SFG or a DFG process inside a nonlinear crystal.

In [18], Israelsen et al. reported a novel upconversion MIR OCT setup, reported in Figure 2.9.

It relied on a custom MIR SC source (MOPA laser), producing a continuous spectrum from 0.9 to 4.7 μm, and an in-house developed broadband upconversion module. This included a MgO-doped periodically poled lithium niobate (PPLN) crystal and a CW

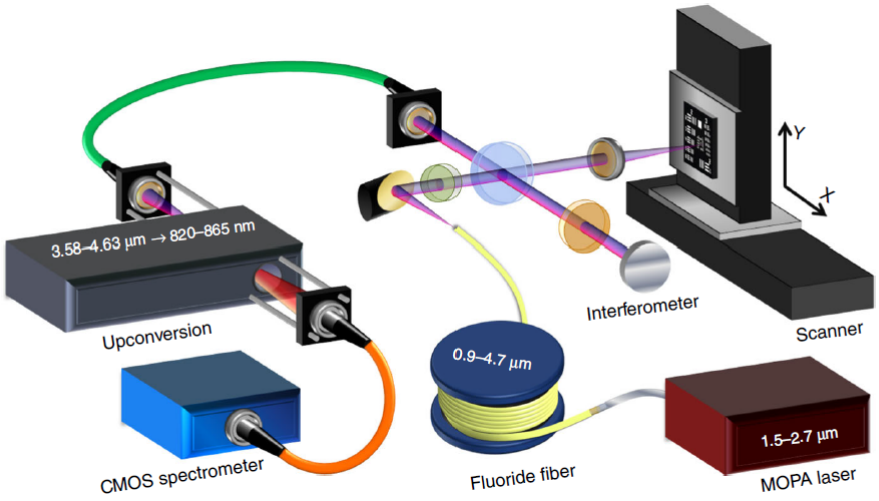

Figure 2.9: *The experimental setup realized by Istraelsen et al. to perform upconversion MIR OCT. Taken from [18].*

laser centered at 1064 nm, which was used as the second input for the SFG process (together with the light coming back from the interferometer's arms). The module was developed to convert the MIR input, more specifically in the large bandwidth $3576-4625$ nm, to the narrow NIR band $820-865$ nm. It was then possible to use a standard 800 nm spectrometer to sample the interference patterns. Their setup showed remarkable performance, with an axial resolution of 8.6 μm (limited by the bandwidth detectable with the upconversion module), a depth range of $\approx$ 8.6 mm (limited by the spectral resolution), and an SNR around 65 dB. They also proved the possibility of resolving the internal structure of highly complex samples, like the Europay, Mastercard, Visa (EMV) chip and the near-field communication antenna embedded in a credit card. Yagi et al. used a similar approach in [19]. In this case, the source is a homemade MIR laser, providing broadband radiation in the $3-4$ μm range, while the upconversion module relies on the DFG process inside a MgO-doped PPLN crystal. The second input for the DFG was generated by a fs pulsed Yb-fiber laser, centered at 1037 nm. Their setup offered an axial resolution of 11.6 μm (again limited by the upconversion module), a depth range of 1.2 mm (related to the linewidth of the pulses for upconversion), and a sensitivity of 55 dB. In both studies, the main limitations lie in the necessity to employ both a complex and expensive MIR source and a second high-power laser to achieve the upconversion process.

Chapter 3

OCT with undetected photons

A proposal to overcome the intrinsic limits of upconversion techniques, which still relies on the powerful features of nonlinear optics, is *interference with undetected photons*. Firstly proposed in [70], this experimental technique grants the opportunity to probe the sample with one beam at a certain wavelength and get all the information by detecting a separate beam, at a different wavelength[71]. In this way, we can circumvent at once both the necessity for generation and detection in the MIR region. The typical interferometric scheme exploited for this technique is the so-called SU(1,1) interferometer, reported in Figure 3.1.

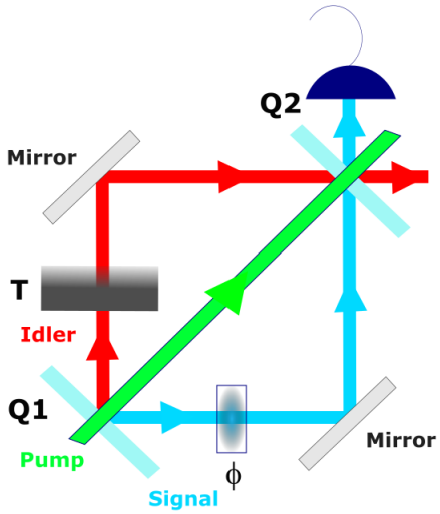

Figure 3.1: *Schematic design of a SU(1,1) interferometer.*

Clearly, it is equivalent to the OCT with undetected photons scheme already illustrated in Figure 2, in which we exploit the reflection through the same nonlinear crystal

instead of the transmission across a second one.

The PDC process inside the crystal Q1 provides idler in the MIR region and signal in the visible/NIR region, while using a standard laser as the pump. Then, the idler is used to probe the sample, whereas the signal is taken as the reference. The passage through the second crystal Q2 determines the interference between the two beams: we can thus measure just one of them (i.e. the signal) to reconstruct the interference pattern.

Since the SU(1,1) geometry is indispensable for my project, it is worth analyzing more in detail its specific features.

3.1 SU(1,1) interferometer for OCT

3.1.1 Mach-Zehnder and SU(1,1) interferometers, single- photon picture

First, I would like to consider the SU(1,1) interferometer in the single photon picture, which is particularly intuitive. Moreover, it is convenient to start from its "linear" counterpart: the Mach-Zehnder interferometer. The term "linear" refers to the fact that we have no nonlinear elements: as we can see from the scheme in Figure 3.2, this interferometer relies just on the splitting of the source beam into two paths, thanks to a first beam splitter, which are then recombined at a second beam splitter before detection [71].

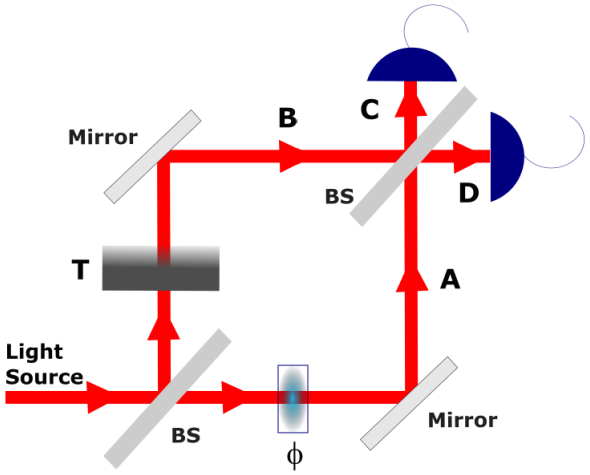

Figure 3.2: *The schematic for a Mach-Zehnder interferometer.*

The phase shifter ϕ along the A path is used to model relative optical delays between the two beams, whereas T along the B path is just a generic transmittance $T = |T|e^{i\gamma}$. In principle, the system is completely equivalent to one using just a single beam splitter,

provided that both the beams are reflected back to it before detection (adding a reference mirror along A and replacing T with R). This last design corresponds exactly to the standard setup for classical OCT, already illustrated in Figure 1.

If we consider a single photon entering the interferometer, and provided the path difference between A and B is shorter than the coherence length, its state after the first beam splitter will be described by the superimposition

$$|\psi\rangle = \frac{1}{\sqrt{2}}(|1\rangle_A |0\rangle_B e^{i\phi}) + \frac{1}{\sqrt{2}}(|T|e^{i\gamma} |1\rangle_B + \sqrt{1-|T|^2} |0\rangle_B) |0\rangle_A , \tag{3.1}$$

where A and B subscripts correspond to A and B paths respectively. This state is then the input for the second beam splitter, whose output $|\psi_{out}\rangle$ can be measured along the paths C and D. We can calculate the expected count rates S_C, S_D using

$$\begin{cases} S_C = \langle\psi_{out}| \hat{N}_C |\psi_{out}\rangle \\ S_D = \langle\psi_{out}| \hat{N}_D |\psi_{out}\rangle \end{cases} . \tag{3.2}$$

The final result is found to be [71]

$$S_{C,D} = \frac{(1+|T|^2) \pm 2|T| \cos(\phi - \gamma)}{4}. \tag{3.3}$$

By scanning ϕ, we can calculate the visibility as

$$\mathcal{V} = \frac{S_{max} - S_{min}}{S_{max} + S_{min}} = \frac{2|T|}{1+|T|^2}, \tag{3.4}$$

which is compatible with the result shown in Equation 1.25.

We consider now the SU(1,1) interferometer. In this case, the two beam splitters of the Mach-Zehnder interferometer are replaced with the two nonlinear media $Q1$ and Q_2. It is important to notice that signal and idler paths from Q_1 are perfectly aligned with the ones at Q_2. For now, we assume to be in the low-gain regime, to simplify the calculations. The total SPDC quantum state before Q_2 is then given by

$$|\psi\rangle = |T|(|1\rangle_S e^{i\phi} |1\rangle_I e^{i\gamma}) + \sqrt{1-|T|^2}(|1\rangle_S e^{i\phi} |0\rangle_I), \tag{3.5}$$

where the two terms account for the idler passing or not passing across the transmittance T. Notice that if we calculate the count rate in the signal mode S_S at this point we get

$$\langle\psi| \hat{N}_S |\psi\rangle = 1, \tag{3.6}$$

which means we have no interference. $|\psi\rangle$ can be then used as the input wavefunction for the second crystal, together with the pump. $r^2 \ll 1$ descibes the probability of $|\psi\rangle$ changing because of the PDC process in Q2. Thus, we can assume this state is

kept fixed at the output. However, we have to consider the additional presence of the pump and the SPDC process acting on it (in this case, we have many photons, and thus the PDC process becomes non-negligible). Consequently, we will have the total output wavefunction

$$|\psi_{out}\rangle \approx \frac{1}{\sqrt{2}}(|T|\,|1\rangle_S\, e^{i\phi}\,|1\rangle_I\, e^{i\gamma} + \sqrt{1-|T|^2}\,|1\rangle_S\, e^{i\phi}\,|0\rangle_I + |1\rangle_S\,|1\rangle_I), \tag{3.7}$$

where the $\frac{1}{\sqrt{2}}$ factor accounts for normalization. We can now calculate the final count rate in the signal mode as

$$\begin{aligned} S_S^{out} &= \langle\psi_{out}|\,\hat{N}_S\,|\psi_{out}\rangle = \\ &= 1 + |T|\cos(\phi+\gamma). \end{aligned} \tag{3.8}$$

By scanning the phase ϕ, we find a visibility

$$\mathcal{V} = |T|, \tag{3.9}$$

compatible with the calculations in [23].

A more general approach requires treating the two passages across the nonlinear media using the Bogolyubov transformations.

3.1.2 SU(1,1) interferometer with Bogolyubov transformations

To precisely describe interference from an SU(1,1) interferometer, we need to recover the mathematical treatise in sections 2.1, 2.2. It is sufficient to consider what happens to the creation/annihilation operators associated to the PDC process after two passages through the nonlinear medium. This is shown in [28] Supplementary material. Let us analyze the general case with two crystals, with length L and displaced at a distance d like in figure 3.3.

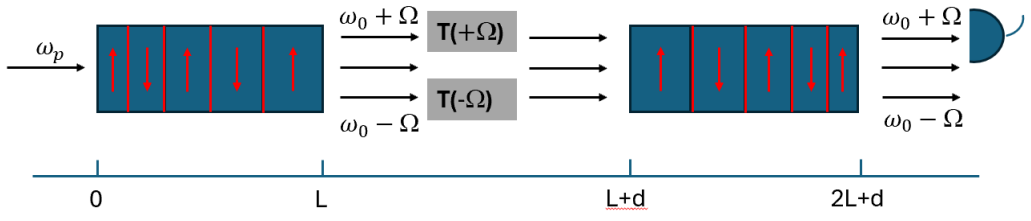

Figure 3.3: *Schematic representation of the passage through the two nonlinear crystals of a SU(1,1) interferometer.*

The annihilation operator evolution after each crystal is given by the Bogolyubov transformations:

$$\hat{a}(\Omega, L) = U_1(\Omega)\hat{a}(\Omega, 0) + V_1(\Omega)\hat{a}^\dagger(-\Omega, 0), \tag{3.10}$$

$$\hat{a}(\Omega, z_{out}) = U_2(\Omega)\hat{a}(\Omega, L+d) + V_2(\Omega)\hat{a}^\dagger(-\Omega, L+d), \tag{3.11}$$

with $z_{out} = 2L + d$, each U_n, V_n factor satisfying unitarity and the relations already described. We introduce then the complex "transmittance" between the two crystals $T(\Omega) = T_A(\Omega)e^{i\phi(\Omega)}$, with $T_A(\Omega)$ being the transmittance amplitude crossed by the component at $\omega_0 + \Omega$, ϕ being the phase acquired. The quotation marks indicate that this term is not necessarily related to a physical transmittance: in an OCT experiment with undetected photons, it would correspond to the reflectance of the sample. We eventually introduce the associated complex "reflectance", defined by the relation $|T|^2 + |R|^2 = 1$. This term allows us to write how the annihilation operators evolve in the space between the crystals

$$\hat{a}(\Omega, L+d) = T(\Omega)\hat{a}(\Omega, L) + R(\Omega)\hat{a}_{vac}(\Omega). \tag{3.12}$$

where the second term accounts for the absorption in the sample. By combining all these equations we finally find (explicit calculations in Appendix E):

$$\hat{a}(\Omega, z_{out}) = U_{int}\hat{a}(\Omega, 0) + V_{int}(\Omega)\hat{a}^\dagger(-\Omega, 0) + U_2(\Omega)R(\Omega)\hat{a}_{vac}(\Omega) + V_2(\Omega)R^*(-\Omega)\hat{a}^\dagger_{vac}(-\Omega), \tag{3.13}$$

where

$$U_{int}(\Omega) = U_2(\Omega)U_1(\Omega)T(\Omega) + V_2(\Omega)V_1^*(-\Omega)T^*(-\Omega), \tag{3.14}$$

$$V_{int}(\Omega) = U_2(\Omega)V_1(\Omega)T(\Omega) + V_2(\Omega)U_1^*(-\Omega)T^*(-\Omega). \tag{3.15}$$

The expression of $\hat{a}(\Omega, z_{out})$ allows us to calculate the output spectrum $S(\omega_0 + \Omega)$ as $\langle \hat{a}^\dagger(\Omega, z_{out})\hat{a}(\Omega, z_{out})\rangle$. We find

$$S(\omega_0 + \Omega) = |V_{int}(\Omega)|^2 + |V_2(\Omega)R(-\Omega)|^2. \tag{3.16}$$

Finally, recalling the relations 2.54, assuming that the pump is undepleted $|U_1| = |U_2|$,$|V_1| = |V_2|$, $r_2 = r_1 = r$, and working for $\Omega > 0$, $T_A(+\Omega) = 1$, $T_A(-\Omega) = T_A$ (just the idler travels across a sample) we find the final result (see Appendix F for the whole calculation)

$$S(\omega_0 + \Omega) = \frac{\sinh^2 2r(\Omega)}{2}\left(\frac{1 + T_A^2}{2} + T_A \cos\big(\tau(\omega_0 - \Omega) + \rho(\Omega)\big)\right) + \sinh^2 r(\Omega)(1 - T_A^2), \tag{3.17}$$

where $\tau = \frac{2z_s}{c}$ accounts for the additional distance traveled by the idler. $\rho(\Omega)$ is a quadratic term responsible for the chirping of the spectral interferogram with respect to the frequency [28].

3.1.3 Mid-infrared OCT in the low-gain regime

We can rewrite Equation 3.17 in the limit of low-gain regime $r \ll 1 \rightarrow \sinh r \approx r$. In this case

$$S(\omega_0 + \Omega) \approx \frac{4r^2(\Omega)}{2}\left(\frac{1+T_A^2}{2} + T_A \cos\big(\tau(\omega_0 - \Omega) + \rho(\Omega)\big)\right) + r^2(\Omega)(1 - T_A^2) = \\ = 2r^2(1 + T_A \cos\big(\tau(\omega_0 - \Omega) + \rho(\Omega)\big)), \tag{3.18}$$

which is consistent with the result in Equation 3.8 and the spectrum shown in [23], with a visibility $\mathcal{V} = T_A$. Recalling that $\omega_s = \omega_0 + \Omega$ we can thus write the number of signal photons as

$$N(\omega_s) = N_0(1 + T_A \cos\big(\tau\omega_s + \phi(\omega_s)\big)), \tag{3.19}$$

where the coefficient N_0 is the number of signal photons when we have no oscillation. This is completely equivalent to the already found expression for the classical OCT in Equation 1.25, with $\mathcal{V} = T_A$, $\tau = 2z_s/c$. We have therefore proved the possibility of applying OCT in the low-gain regime.

3.1.4 Mid-infrared OCT in the high gain regime

In the high-gain regime, we have that $\sinh^2(2r) \gg \sinh^2 r$, thus the interference spectrum 3.17 can be rewritten neglecting the last term

$$S(\omega_0 + \Omega) \approx \frac{\sinh^2 2r}{2}\left(\frac{1+T_A^2}{2} + T_A \cos\big(\tau(\omega_0 - \Omega) + \rho(\Omega)\big)\right). \tag{3.20}$$

We can then proceed in the calculation exactly as in the low-gain regime, finding

$$N(\omega_s) = N_0\left(1 + \frac{2T_A}{1+T_A^2}\cos\big(\tau\omega_s + \phi(\omega_s)\big)\right), \tag{3.21}$$

which is again analogous to the classical OCT spectrum 1.25, with the visibility being given by $\mathcal{V} = \frac{2T_A}{1+T_A^2}$. These results are compatible with the ones derived in the Supplementary Material of [28] and they can be used to describe the expected behavior for my experimental setup.

3.2 Existing implementations of OCT with undetected photons with SU(1,1) interferometer

Many works have proved the potential of SU(1,1) interferometry to realize OCT with undetected photons. The general schematic of the setup, employable for both TD and FD OCT, is the one illustrated in Figure 3.4.

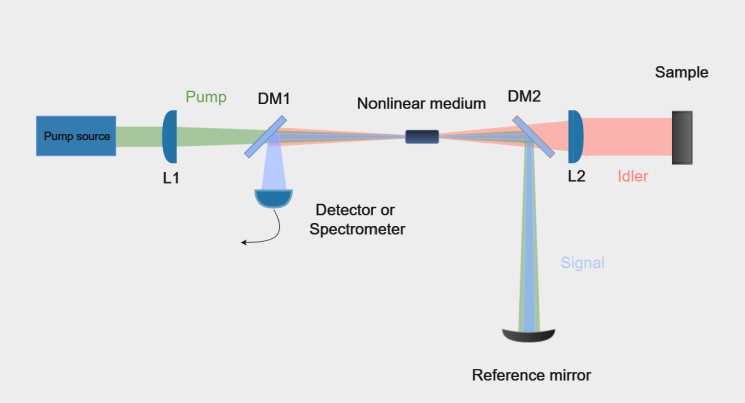

Figure 3.4: *The usual experimental schematic to achieve OCT with undetected photons. DM stands for dichroic mirror, L stands for lens.*

The pump is firstly focused by the lens L1 into the nonlinear crystal. The PDC process generates idler and signal beams at different wavelengths, which get separated by the dichroic mirror DM2. In this way, the pump and signal beams are sent into the reference arm, where they get back-reflected by the reference mirror. On the contrary, the idler beam is conveyed into the idler arm, where it gets collimated or focused into the sample using the lens L2 and, eventually, gets reflected. All the beams come then back to the nonlinear medium, where they interfere. Finally, the signal beam is isolated using the second dichroic mirror DM1 and the measurement is performed by using a photodetector or a spectrometer. The main conceptual difference between various proposals lies in the choice of the nonlinear medium. The proof-of-concept for infrared TD-OCT with undetected photons in the low-gain regime was reported by Paterova et al. in [22]. Their setup relied on the collinear PDC process inside a PPLN crystal. Different crystal designs were evaluated, with the idler central wavelength ranging from ≈ 1.5 μm up to ≈ 3 μm (so with this last one in the MIR range). The pump was an ordinary Nd:YAG (Yttrium-Aluminum Garnet) CW laser, with the central wavelength at 532 nm or 488 nm depending on the crystal design used. Moreover, both a notch filter and a bandpass filter were inserted before the detector (a CCD camera) to remove the noise. The setup suffered from the narrow bandwidth of the tunable source, resulting in an axial resolution of ≈ 93 μm. Nonetheless, it was successfully applied to a high variety of samples, including a Si window and a microscope resolution target test.

The state-of-the-art for OCT with undetected photons in the low-gain regime was achieved by Vanselow et al. in [23]. Their setup, designed to perform FD-OCT, is reported in Figure 3.5.

In this case, the three beams were collimated by using an off-axis parabolic mirror (OAP), with the idler getting then focused into the sample to achieve high lateral resolution. The pump was a frequency-doubled Nd:YAG CW laser, centered at 660 nm

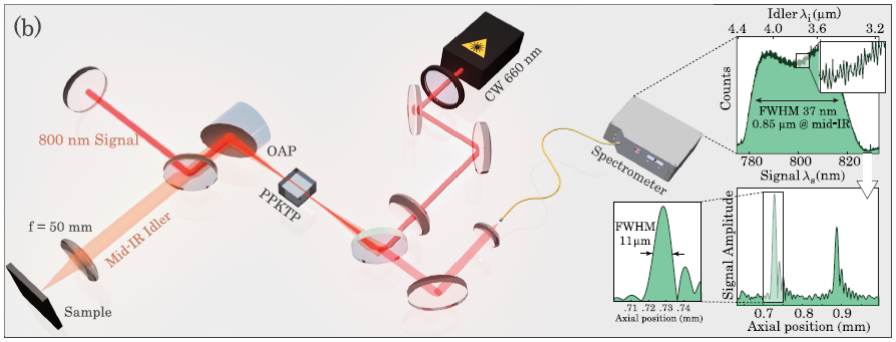

Figure 3.5: *The optical setup realized by Vanselow et al. The inset shows a typical raw interference spectrum and the corresponding OCT spectrum. Taken from [23].*

and with a maximum power of 500 mW. The spectrometer was a commercial uncooled spectrometer, providing a very good spectral resolution around 0.11 nm. By exploiting the PDC process inside a ppKTP crystal, granting broadband idler and signal (from 3.3 to 4.2 μm and from 785 to 823 nm respectively), they achieved an axial resolution of 10.1 μm, a depth range around 2.8 mm, and an SNR equal to 47 dB at 8 ms integration time. Moreover, they demonstrated the setup to be shot-noise limited and managed to resolve the internal structure of a high-interest multilayered alumina sample.

In [72], Roeder et al. have recently shown NIR TD-OCT after replacing the usual bulk nonlinear crystal with a PPLN waveguide. This nonlinear medium provided high brightness and the possibility to optimize the SNR by adjusting the relative gain of the two PDC processes, compensating the losses inside the interferometer. The PDC process provided idler and signal centered at 1360 nm and 830 nm respectively, using a commercial CW laser centered at 514 nm as the pump. The detection was achieved by using a commercial, inexpensive photodetector. The main limitation was the axial resolution, which resulted in ≈ 0.2 mm, owing to the waveguide's narrow bandwidth.

Machado et al. proved for the first time both TD and FD NIR OCT with undetected photons in the high-gain regime ($r \approx 4.8$) in [24]. Their setup relied on the usage of a PPLN crystal, providing broadband idler (8 nm bandwidth centered at 810 nm) and signal (30 nm bandwidth centered at 1550 nm). The pump was a pulsed Nd:YAG laser, generating 18 ps long pulses centered at 532 nm, with a repetition rate of 1 kHz. They successfully resolved a thick microscope glass slide with $d = 100$ μm and exploited the seeding effect to achieve a high signal photon number ($\approx 4 \times 10^5$ photons per pulse) while preserving limited idler power (1.6 fJ per pulse). However, their system suffered from limited axial resolution, around ≈ 30 μm (determined by the signal bandwidth), and depth range, ≈ 300 μm (related to the spectrometer resolution).

Hashimoto et al. addressed these limitations in [28], adopting the setup reported in Figure 3.6.

In this case, the nonlinear medium was an aperiodically poled lithium niobate crystal,

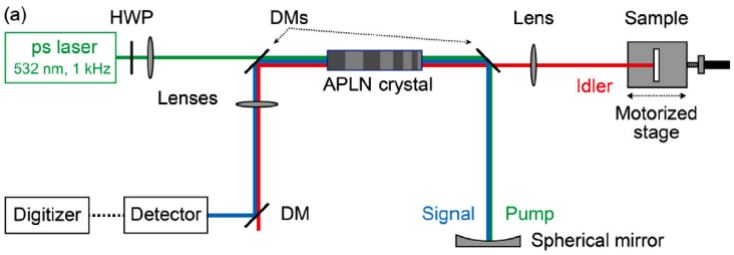

Figure 3.6: *The optical setup realized by Hashimoto et al. HWP stands for half wave plate, DM for dichroic mirror. Taken from [28].*

providing further enhanced idler and signal bandwidths (experimentally found to be $\approx$ 30 THz, with central wavelengths equal to 1565 nm and 796 nm respectively) and, consequently, a better axial resolution, around $\approx$ 11 μm. The pump was again a ps-pulsed pulsed laser, centered at 532 nm and with an average pump power equal to 1 mW. The average signal power at the output was found to be $\approx$ 10 μW, making it possible to use an ordinary Si power meter for the measurement. The setup successfully resolved very thin films of lithium niobate and cover glass, with thicknesses of 7 and 102 μm respectively. However, it suffered from the limited depth range $\approx$ 300 μm, still determined by the spectrometer resolution.

Chapter 4

Mid-infrared OCT with undetected photons in the high-gain regime

4.1 Introduction

We have analyzed in detail the existing approaches to achieve MIR OCT, carefully considering the advantages and disadvantages of each of them. The "classical" implementations are still far from being comparable with their NIR counterpart, despite significant improvements achieved using novel devices (supercontinuum sources, OPOs, or pyroelectric array detectors). The upconversion scheme shows promise, as it avoids the need for a MIR detector and achieves axial resolution as low as ≈ 10 μm and a satisfying scan rate. However, it has significant limitations, including the need for an MIR source and the intrinsic drawbacks of the upconversion scheme. Eventually, MIR OCT with undetected photons, implemented up to now just in the low-gain regime, showed remarkable performance, with an axial resolution ≈ 10 μm, shot-noise level of detection. Nonetheless, the low-gain regime prevents the use of ordinary detectors, being intrinsically defined by low signal power. The solution I explore in this project is the implementation of a MIR OCT interferometer with undetected photons, operating in the high-gain regime.

The high-gain regime is characterized by the seeding effect, which opens the possibility of achieving high signal power (measurable using ordinary detectors, like Si power meters) without giving up on probing the sample with a low-power, non-invasive idler. Since the high-gain regime is inherently defined by a larger number of photons per mode than the low-gain regime, we can conclude that it should grant higher SNR at parity of noise (and other measurement conditions).

The theoretical description of OCT with undetected photons in the high-gain regime was reported in the previous chapter, together with a review of the first implementations, limited up to now to the NIR range. Here, I describe in detail my work to develop and test the first experimental setup achieving MIR OCT with undetected photons in the

high-gain regime.

4.2 Experimental setup and methodology

4.2.1 Optical scheme and components

The main setup for my project has been realized by adapting the design in [29], previously employed for FTIR (Fourier-transform infrared) spectroscopy. The scheme is illustrated in Figure 4.1.

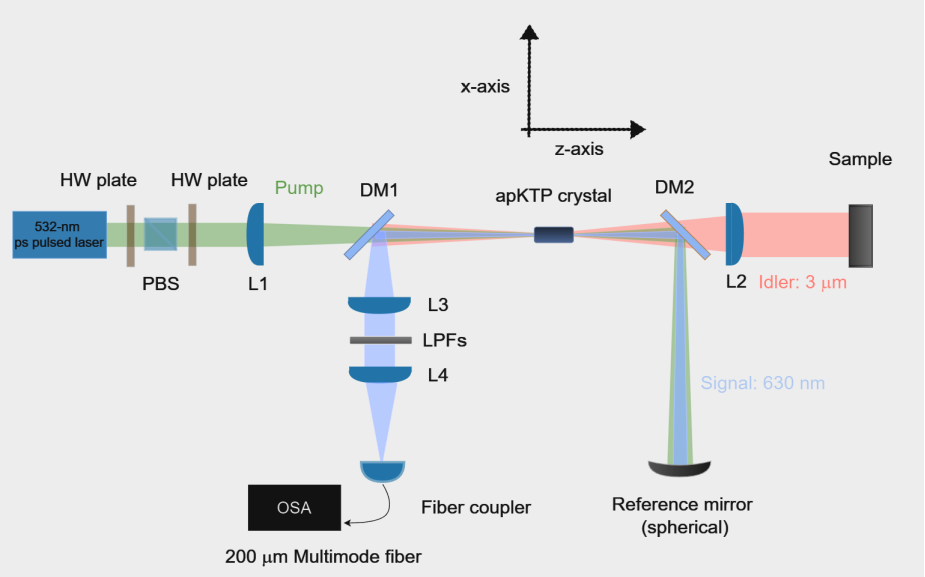

Figure 4.1: *The optical setup realized to perform MIR-OCT with undetected photons in the high-gain regime. HW stands for half-wave plate, PBS for polarizing beam splitter, L for lens, DM for dichroic mirror, and LPF for low-pass filter.*

This design is conceptually analogous to the one presented in Figure 2, with the sample placed along the idler arm and the reference, mirror (spherical with $f = 100$ mm) along the signal arm.

The input light is generated by a $15 - \text{ps}$ pulsed laser, centered at 532 nm and with a repetition rate of 1 kHz (Ekspla, PL2210A-1K-SH/TH). The beam passes then through a first half-wave plate, a polarizing beam splitter (PBS), and a second half-wave plate. Since the input pump is linearly polarized, the purpose of the first half-wave plate is to change the polarization angle and thus the amount of light transmitted by the PBS. In this way, we can control the input pump power. The second half-wave plate, instead, is aligned such that the polarization angle matches the optic axis of the

crystal, required to have the phase matching conditions for PDC[1]. The light is then focused into the crystal using a focal lens with $f = 200$ mm (L1 in Figure 4.1), achieving high-gain PDC. Immediately after the lens, we can use a Si power meter (Thorlabs, S130VC) to measure the pump power. The apKTP (aperiodically poled Potassium Titanyl Phosphate $KTiOPO_4$) crystal (provided by Raicol Crystals) has a poling period gradually increasing from 12.3 to 14.0 μm and will be described in detail in the next subsection. It is mounted on a movable two-axis stage to optimize the alignment and the PDC process.

A first dichroic mirror (DM1 in Figure 4.1) separates the idler beam (centered at ≈ 3 μm) from the signal (centered at ≈ 630 nm) and pump beams. The idler beam reaches the sample after being collimated by using a $f = 100$ mm CaF_2 lens (L2 in Figure 4.1). This choice results in a macroscopic idler beam size, which affects the lateral resolution, expected to be in the mm range, and makes the idler more susceptible to scattering. Nevertheless, other important applications of the MIR-OCT, such as probing materials containing non-transmitting layers in the NIR region, should not be limited by it.

The sample is mounted on a motorized stage, allowing motion along both the $z-$axis (depth) and the perpendicular $x-$direction (vertical in the figure) for B-scan measurement.

The back-reflected idler reaches the nonlinear crystal a second time, together with the signal and the pump coming back from the reference mirror. This determines a second PDC process, completing the SU(1,1) interferometer. The signal spectrum at this point is described by the formula in Equation 3.20, containing all the information about the back-reflecting internal structure of the sample.

To separate the signal beam from the other beams and carry out the measurement, a second dichroic mirror (DM2) and a scheme consisting of a collimating lens ($f = 100$ mm, L3 in Figure), two long pass filters (Thorlabs, FGL570 (cut-off of 570 nm) and Thorlabs, FELH0550 (cut-off at 550 nm)), and a focusing lens ($f = 100$ mm, L4 in Figure) are employed. The focused signal beam is then properly coupled into a multimode fiber with a core size of 200 μm and finally connected to the spectrometer. The PDC process inside the crystal is spatially multimode. Therefore, a multimode fiber is needed to collect all the spatial modes and get a sufficient amount of signal in the spectrometer. In general, a trade-off exists between the size of the fiber's core and the spectrometer resolution. Achieving a high resolution requires the usage of a narrow exit slit of the monochromator, reducing the amount of light reaching the detector but increasing the ability to resolve close spectral features. A narrow core fiber is needed as well, to preserve the high spatial coherence of the light [73]. On the contrary, using a wide core size in combination with a large exit slit increases the intensity of the broad peak, but limits the best achievable spectral resolution. The optimal core size of 200 μm was chosen considering the balance

[1]When the polarization angle has to match the optic axis of the crystal to satisfy the phase matching conditions, we say that the PDC is of type 0. This is the case for our nonlinear crystal

between these two aspects.

The measurements of the interference spectra were performed by using an optical spectrum analyzer OS (Yokogawa, AQ6374).

One of the key aims of this project is to realize an OCT setup operating in the MIR range. A fundamental aspect of this work is then to compare the performance of the realized setup to the one of an ordinary NIR OCT setup. This comparison can help identify new applications that are not possible for the classical OCT implementations. To facilitate this comparison, I realized a NIR-OCT setup as well, described in detail in Appendix G.

4.2.2 The apKTP crystal

The heart of the interferometer is the nonlinear apKTP crystal. Its experimental characterization was previously performed in [29], to which I refer for detailed specifications.

KTP crystals are promising nonlinear materials, characterized by large $\chi^{(2)}$, thermally stable phase-matching, low dielectric constant, and broad acceptance angles [74].

In my setup, the KTP crystal was designed to have a chirped poling period along the crystal axis. The grating vector K (defined as $\frac{2\pi}{\Lambda}$) linearly decreases from 510 rad/mm (i.e. $\Lambda = 12.3$ μm) to 449 rad/mm ($\Lambda = 14.0$ μm). The chirp rate is $\zeta = 6.1$ rad/mm^2.

The crystal was fabricated using a mask designed according to the profiles reported in Figure 4.2a. Figure 4.2b shows the resulting microscopic images of the long and short periods respectively. The linear chirping was achieved by employing a piecewise-constant quasi-linear profile, characterized by a local period increment of 25 nm [29]. From the design, it is evident that the crystal can be oriented in a short-long or a long-short direction, depending on the spatial period of the first region encountered by the pump beam.

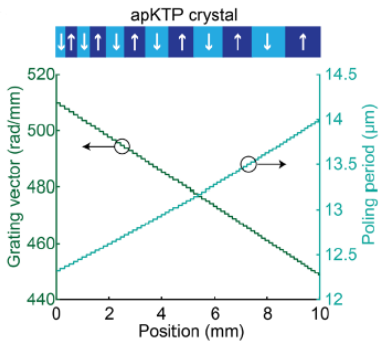

(a) *The mask design's schematic, showing the variation of grating vector and poling period. Taken from [29].*

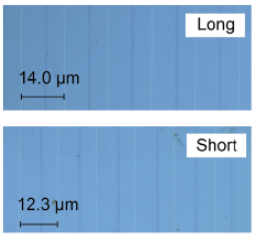

(b) *Microscopic images showing the fabricated apKTP. above the long poling period is shown, below the short one. Taken from [29].*

The signal spectrum resulting from the first PDC (i.e. one passage through the crystal) was measured in [29]. The results are shown in Figure 4.3a, which compares the simulated data (dotted line) to the experimental ones (solid line). The idler spectrum, instead, is reported only from simulations' results. The plot is illustrated in Figure 4.3b.

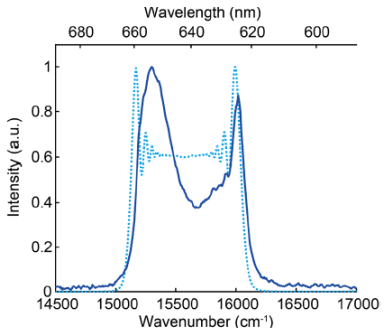

(a) *A comparison between the experimental data (solid line) and the simulated ones (dotted line) for the first PDC signal spectrum of the fabricated apKTP. Taken from [29].*

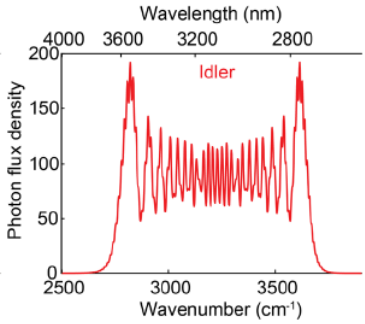

(b) *The simulated data for the idler first PDC spectrum for the fabricated apKTP. Taken from [29].*

From the simulations, the spectra are expected to span approximately the ranges 624nm $\leq \lambda_s \leq$ 660nm and 2.74μm $\leq \lambda_i \leq$ 3.60μm. The measured signal spectrum is in good agreement with the simulated one, although it is affected by detrimental processes at high gain (e.g. at high pump power). The first issue is bandwidth narrowing: depending on the orientation of the crystal (short-long or long-short), the intensity at either the shorter or longer wavelength increases much more rapidly than the other, resulting in an overall shrinking of the spectrum. This phenomenon is thought to be caused by the depletion of the number of signal photons inside the crystal, owing to the emergence of additional nonlinear effects at high power, possibly the coincidental phase-matched pump-signal SFG [29]. The second issue is a time decrease in the signal intensity: this process is probably due to gray tracking effects. These effects are well known for KTP materials: they are fatigue damages caused by the internal defects of the crystal, associated with the reduction of nonlinear properties [74]. Both these effects must be carefully accounted for during the measurement process.

4.2.3 Samples description

I performed preliminary measurements (SNR estimation, roll-off curve, axial resolution...) using a standard flat silver mirror as the sample. To demonstrate that the realized MIR-OCT setup could perform FD-OCT and resolve microstructures, I employed a "stepped" Al sample and a thin Si layer:

- The Al stepped sample is shown in Figure 4.4, together with its schematics. It is characterized by a step height of ≈ 100 μm, separating two highly parallel and flat surfaces. The sample was kindly provided by the Max Planck Institute for the Science of Light's mechanical workshop.

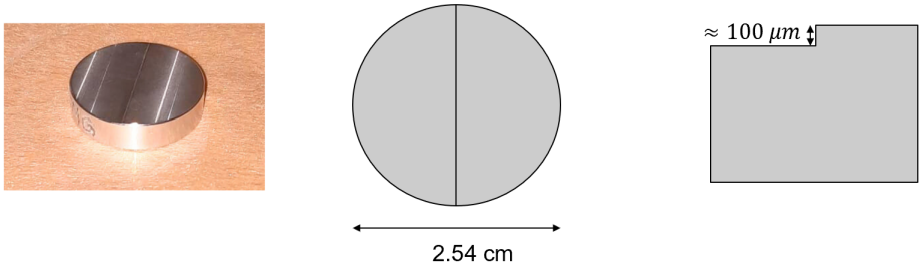

Figure 4.4: *Photo and schematic design of the Al stepped sample*

- The Si thin layer was cut from a 3-inch Si wafer, (50 ± 10) μm thin, and is double-side polished (Waferworld, SKU 1034). For the measurement, the layer was mounted on a silica flat window. This is shown in Figure 4.5. The window was carefully chosen to ensure it had no measurable reflectance at the probing wavelength, guaranteeing that the entire back-reflected light effectively came from the layer.

Figure 4.5: *Photo of the cut Si layer, carefully attached to the flat* SiO_2 *window for measurement.*

Choosing a suitable sample to demonstrate the advantages of MIR-OCT over NIR-OCT was challenging. As previously mentioned, the macroscopic size of the idler beam made the system highly affected by scattering, making it impossible to successfully measure highly scattering materials like alumina or zirconia. However, germanium (Ge) is a suitable candidate: this material is characterized by very low transmittance in the NIR region, as shown in Figure 4.6.

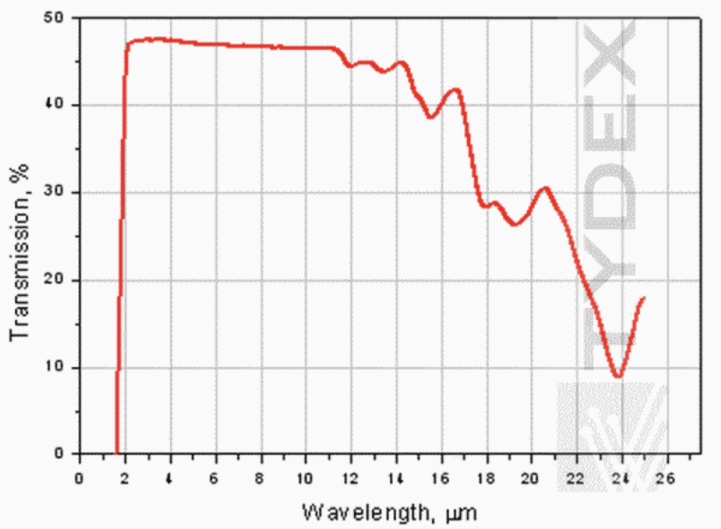

Figure 4.6: *Ge transmission curve, reported over NIR and MIR ranges. Taken from [75].*

Despite most applications relying on very thin active layers of Ge ($\approx$ nm), the inactive Ge substrate is usually much larger, making it difficult to realize effective NIR OCT. For example, in germanium solar cells the total Ge substrate thickness is around 175 μm, even though the emitting layer typically lies in the range of $150 - 250$ nm [76]. If we wanted to probe the underlying structure using classical OCT, we would rely only on the transmitted portion of the light, which is expected to be around $T^2(1.5\mu\text{m}) = 0.0069$ (considering forward and backward transmissions) [77]. This makes NIR OCT highly ineffective.

In the MIR range, however, Ge's transmittance is known to increase significantly. Therefore, I decided to test whether our setup could successfully resolve structures behind a Ge window. In particular, I used a broadband anti-reflective (BBAR) coated Ge window (AR coating range: $3 - 12$ μm), with a thickness of 1 mm and a size of 1/2-inch, double-side polished (Edmund Optics, 83-347). The transmission at the idler central wavelength declared by the constructor is $T(3\mu\text{m}) \approx 0.93$

4.2.4 General methodology and preliminary measurements

The measurement procedure is quite standardized for both the MIR-OCT and NIR-OCT setups. It involves mounting the sample in the idler arm, adjusting its orientation and position in order to maximize the superimposition between the back-reflected beams, changing its z-coordinate to identify the ZPD position (corresponding to the maximum of interference), and eventually slightly moving it within the depth range. The alignment procedure is considered in further detail in Appendix H for the MIR-OCT setup.

Once aligned, we can measure the interference and non-interference patterns. The

non-interference pattern is needed to properly remove the background, as explained in section 1.2.5. It can be obtained by moving the sample far away from the ZPD, at a distance longer than the depth range (in my case, preliminary analysis showed a depth range ≈ 350 μm for the MIR-OCT setup, ≈ 2.5 mm for the NIR setup. Thus, the sample was moved of ≈ 500 μm and ≈ 5 mm respectively).

Initially, I used the silver mirror as the sample, to evaluate the performance of both setups. More specifically, I made the following preliminary measurements for the MIR OCT setup:

1. SNR versus averaging times: the averaging times parameter is a setting of the OSA, which quantifies how many measurements the spectrometer must average for each wavelength value [78]. I will use the less ambiguous term "number of averages" from now on

    - I sampled ten interference spectra for each number of averages, operating at a fixed position of the sample (≈ 100 μm from the ZPD) and a fixed pump power (1.03 ± 0.02 mW). This value was chosen as a good compromise between having a sufficient SNR and limiting gray tracking effects. It was therefore roughly retrieved for all subsequent measurements.
    - After completing each set of 10 measurements, the crystal was slightly shifted perpendicularly with respect to the beam direction, changing the focusing point inside it. This operation helps to mitigate the gray-tracking effects without changing the global spectral shape
    - This measurement justified the number of averages chosen for the following measurements (discussion in the following sections): 30.

2. Roll-off curve: The roll-off curve reconstruction is fundamental, as it shows the possibility of performing FD-OCT, measuring the depth range, and understanding the behavior of axial resolution and SNR at different depths. Two procedures were adopted. In the first, the roll-off profile was reconstructed by measuring the inference spectrum for each depth just once, to simulate an FD-OCT measurement. In the second case, I sampled ten spectra for each depth value, analogously to the SNR versus averaging times measurement. This second strategy aims to find the statistical uncertainties associated with the axial resolution and the SNR.

3. SNR versus signal power: Determining this curve allows us to understand which is the dominant noise source in the setup.

    - The procedure was analogous to the SNR versus averaging times measurement, i.e. sampling ten spectra for each signal power value at a fixed depth and pump power. In this case, the depth was roughly 150 μm.

- The signal power was modified by moving a variable Neutral Density (ND) filter, placed in front of the detector.

4. Lateral resolution measurement: A D-shaped mirror was used as the sample for this purpose.

    - The idea is to perform a so-called knife-edge measurement: if we place the D-shaped mirror as in Figure 4.7 and perform a B-scan (moving in the x-direction), we expect to observe the reflection (and so the corresponding OCT peak) just moving towards the half where the mirror is present.

Figure 4.7: *Photo of the D-shaped mirror employed as the sample to estimate the idler beam size. The blue arrow indicates the x-direction for the B-scan.*

    - If we plot the OCT peak height as a function of the lateral position, we expect to observe an erfc profile, whose shape is directly related to the beam size. (See Appendix I for the derivation)
    - To obtain the OCT heights versus lateral positions function, various interference spectra were measured at a fixed depth, slightly changing the lateral position using the motorized stage. In this case, I chose to decrease the number of samples for each lateral position to one, owing to the large number of points required to perform an effective nonlinear fit. The uncertainty associated with each OCT height was calculated assuming that the relative uncertainty is equal to that found for a single measurement (i.e. using the standard deviation instead of the standard deviation of the mean) of the normal mirror at the same depth.

For the NIR OCT setup, I limited the preliminary measurements to the roll-off curve measurement, as it is used solely for comparison. The aim was to estimate the axial res-

olution, SNR, and depth range and compare them to the typical values for commercially available OCT setups. In this case, the averaging times value was set equal to 1, as the SNR was already sufficient.

The main setting parameters chosen for the OSA were the measurement span ($620 - 650$ nm for the MIR setup, $1300 - 1700$ nm for the NIR setup), the spectral resolution (for both setups $\delta\lambda_{sp} = 0.5$ nm), the sampling period (0.1 nm for both setups), and the sensitivity mode (HIGH2). All these choices are justified and deepened in Appendix J.

4.2.5 Samples measurement

After completing preliminary evaluations, I used both the MIR OCT and NIR OCT setups to measure the stepped Al sample and the Si layer.

The stepped Al should behave as a single reflective layer, with the depth depending on the lateral position. To highlight this feature, it was necessary to perform a whole B-scan. The procedure is completely analogous to the ones described above: all A-scans were reconstructed at a fixed position of the sample (the one maximizing the SNR) and fixed pump power. After measuring each interference pattern, the lateral position was changed by using the motorized stage. Each A-scan was measured just once.

For the Si layer, the main purpose was to resolve its thickness. Since the thickness should not change with the lateral position, this coordinate was kept fixed. In the case of the MIR OCT setup, I sampled different A-scans at slightly different depths, in order to emphasize the consistent displacement of the two peaks. Moreover, each A-scan was sampled ten times, to have more statistics and increase the SNR.

The second fundamental objective was to show the effective advantage of the MIR-OCT setup, which is able to overcome the presence of the Ge window in the idler arm. To achieve this, I first measured the A-scan for the silver mirror before and after mounting the Ge window, for both the NIR OCT and the MIR OCT setups. Ge has a group index $n_g(1.5\mu\text{m}) = 4.265$, $n_g(3\mu\text{m}) = 4.0959$ [77]. Therefore, after mounting the window it was necessary to move the sample along the $z-$direction to compensate for the additional path and retrieve the interference. Since we expect to see nothing in the case of the NIR OCT setup due to the extremely low transmittance, several positions (spanning $\pm$2mm around the expected one $z_f = z_0 - n_g * 1\text{mm}$) were considered to ensure that the results were not affected by the chosen position of the sample.

Then, I also measured a second time the A-scan for the Si layer in both cases, to show that the MIR-OCT setup is still able to resolve a microstructure even with the presence of the Ge window. Again, ten measurements were performed to enhance the SNR.

The reconstruction of the OCT spectra starting from the measured interference spectra is described in detail in Appendix K. Essentially, each interference pattern was properly processed and transformed using the inverse Fast-Fourier-Transform (iFFT) to reconstruct the corresponding OCT spectrum. Figure 4.8 shows three interference spectra,

measured for three different depths of the mirror (expected steps of ≈ 60 μm), and the corresponding OCT spectra.

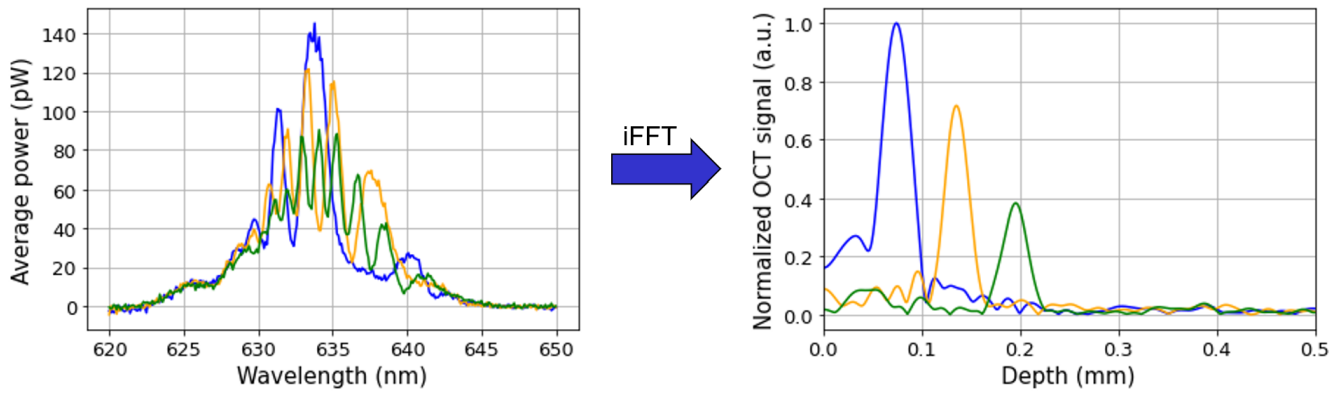

Figure 4.8: *Three experimentally sampled interference spectra corresponding to three different axial positions of a silver mirror. On the right, the resulting OCT spectra are shown.*

4.3 Results and discussion

4.3.1 Results of preliminary measurements for MIR-OCT setup

Before discussing the main results, it is worth mentioning the signal power and visibility found for the standard measurement conditions. I evaluated them in detail just for the SNR vs number of averages measurements, as they are expected to be roughly preserved in other cases. The visibility was found to be $\mathcal{V} = 0.813 \pm 0.007$, while the signal power was 9.0 ± 0.5 nW (calculated from the interference spectra).

The measurement of SNR vs number of averages yielded the results reported in Figure 4.9a and 4.9b.

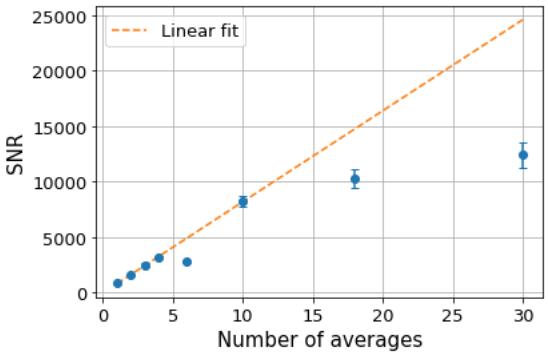

(a) *Behavior of the SNR vs the number of averages set on the OSA. The uncertainties are the statistical ones. The orange line corresponds to the linear fit for the points up to 10 averages.*

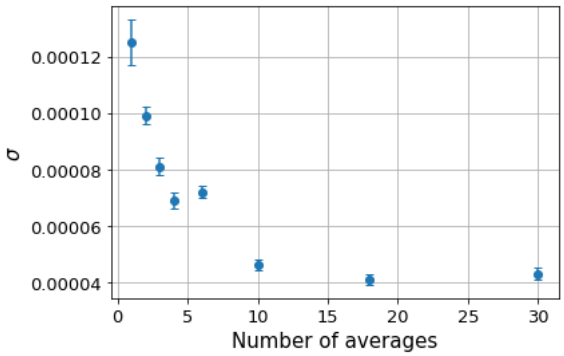

(b) *Behavior of the noise σ vs the number of averages set on the OSA. The uncertainties are the statistical ones.*

Figure 4.9: *Results for a different number of averages.*

The first plot shows the value of the SNR vs the number of averages, while the second one shows more in detail the behavior of σ, i.e. the noise calculated as the standard deviation of the data in the OCT spectrum far away from the main peak [23]. As expected, the number of averages increases the SNR. For a number of averages up to 10, we observe an optimal agreement with the theoretical linear behavior, related to the fact that the random noise responsible for σ decreases as the square root of the number of averages [79]). The linearity is confirmed by the fit performed in this region (the fifth experimental point can be excluded using the Chauvenet criterion), with an extremely high determination coefficient $R^2 = 0.999$. However, for a higher number of averages, we observe a decrease in the slope, compatible with the emergence of some systematic effects that do not average out. Since the OSA noise characterization does not show such features (more in detail in Appendix L), we can suppose data processing is responsible for them. In particular, a noncorrect experimental evaluation of the noninterference spectrum (possibly connected to gray-tracking effects during the measurement) might explain the observed disagreement from the linear increase. The behavior of σ seems to show a saturation in the noise decrease above 15 averages. After this value, the variation of the SNR is just due to the small increase in the OCT peak height. The main condition for the optimal choice of the number of averages is then > 15. Additionally, this number should be chosen in order not to determine a too-long measurement time. These two factors led me to choose 30 (The corresponding measurement time for each interference spectrum in the MIR OCT setup case (with the settings previously indicated) is around 150 s).

Figure 4.10a reports the roll-off curve obtained for a single measurement for each

position, while Figure 4.10b shows the dependence of the axial resolution on the depth, studied with higher statistics.

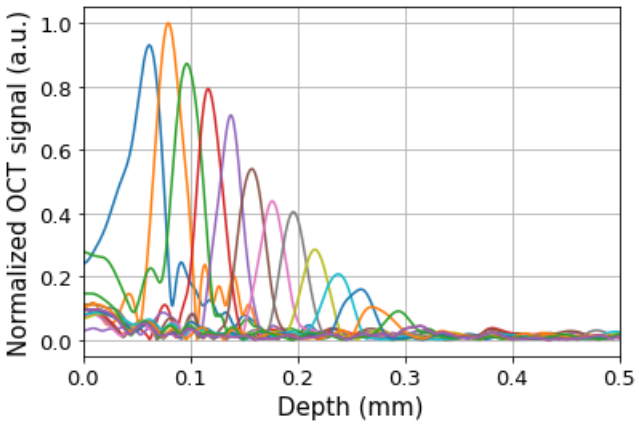

(a) *The measured roll-off curve for the MIR-OCT setup.*

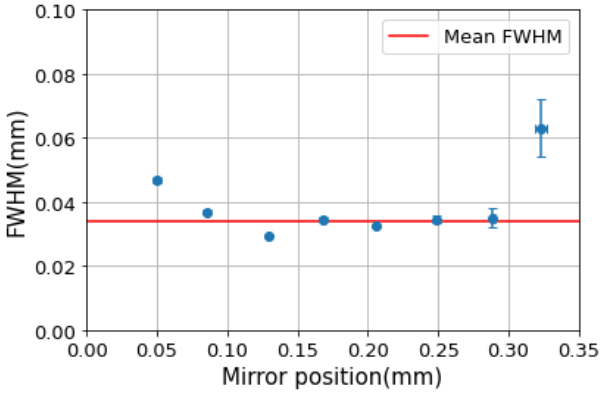

(b) *The dependence of the axial resolution on the depth. The error bars correspond to the statistical uncertainty.*

Figure 4.10: *Characterization of the FD-OCT roll-off.*

The first plot shows how the SNR decreases with the position. The depth range is found to be ≈ 320 μm, where the SNR is still high enough to resolve the mirror OCT peak. It can be noticed that the optimal position seems to be at ≈ 100 μm from the ZPD. Nearer peaks are affected by smaller SNR and broadening, probably owing to the effect of some residual DC component. These features are confirmed by Figure 4.10b. In this case, the axial resolution seems quite constant in the range $100 - 300$ μm from the ZPD, with the average value $\text{FWHM}_z = (33.8 \pm 0.1)$ μm. It increases rapidly when moving at nearer or farther depths, showing high uncertainty in the second case. To fully understand the origin of these effects, I decided to compare the experimental roll-off with a simulated one. The discussion and interpretation of these findings are reported in the corresponding subsection.

Eventually, the roll-off curve measurement allows us to study the uncertainty on the peak position as well. This is shown in Figure 4.11.

As expected, the statistical uncertainty is almost constant up to ≈ 250 μm, where it rapidly diverges since we are approaching the depth range. The average value far away from this limit, corresponding to the red line in the figure, was found to be (0.4 ± 0.2) μm. We can now multiply this value by $\sqrt{10}$ (where 10 is the number of measurements) to estimate the average uncertainty on the mirror position provided by a single A-scan

$$\delta z \approx 1.3 \mu\text{m} \tag{4.1}$$

The SNR vs Signal Power curve is reported in Figure 4.12a, together with the corresponding I vs Signal Power plot in Figure 4.12b (I corresponds to the height of the OCT

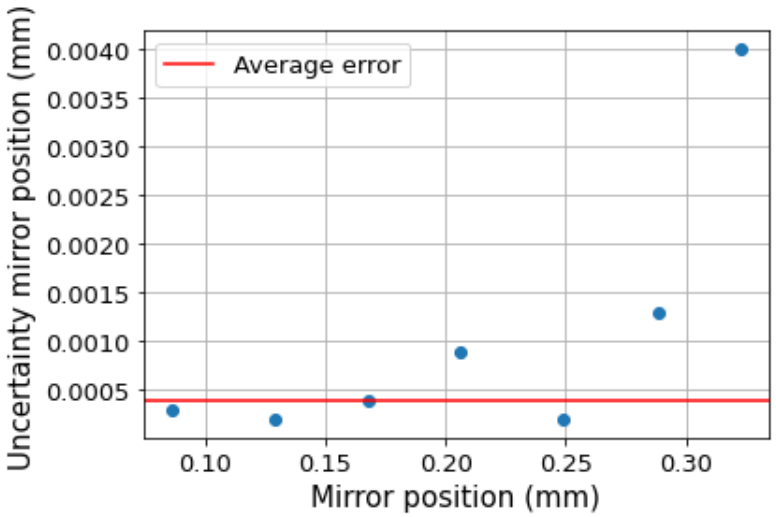

Figure 4.11: *Dependence of the error on the mirror position (calculated as the standard deviation of the mean) on the roll-off. The red line indicates the average value of the uncertainty, calculated in the range of positions* $0.1 - 0.25$ *mm.*

peak). Firstly, it is worth underlining that the difference between the SNR values shown here and those found for the averaging times characterization is just due to the roll-off. These measurements were performed with the mirror at a depth (165.1 ± 0.5) μm, while the previous ones were at (96.3 ± 0.4) μm.

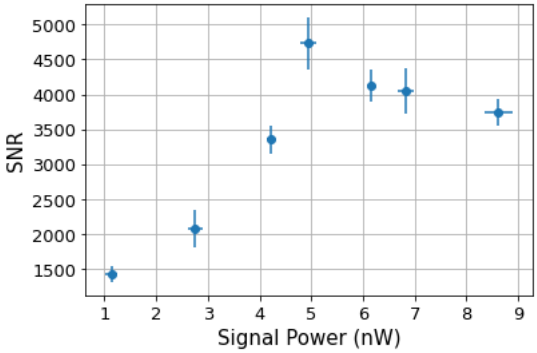

(a) *The SNR dependence on the Signal Power. The uncertainties are the statistical ones.*

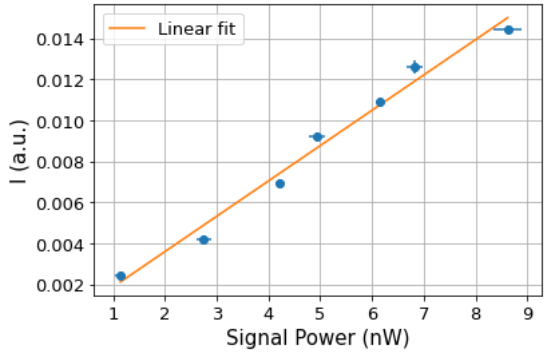

(b) *The behavior of the OCT height I vs the Signal power.* The orange line represents the linear fit.

Figure 4.12: *Results of the characterization at different signal powers*

The behavior of the SNR shows a probable variation of the dominant noise term. To confirm this, it is necessary to verify the expected curve for I. In this case, the data seem

to confirm the theoretical linearity, with the linear fit validated by the high determination coefficient $R^2 = 0.983$. This means that the behavior of the SNR is connected just to the dominating noise, which seems to drastically change between low signal power and high signal power regions.

Since the shot-noise level (expected to determine an SNR around 100 dB using Equation 1.36) is far from the observed condition, we can conclude that the dominant noise must be different. In particular, both detector noise and Relative Intensity Noise (RIN) of the signal pulses are possible candidates. Since the detector noise is constant with the signal power, it will be responsible for a quadratic dependence of the SNR on it. On the contrary, RIN is proportional to the signal power, therefore it will give a constant contribution to the SNR. A reasonable explanation of the observed behavior is then that the dominant noise changes from the detector's noise to RIN, with the second one prevailing above ≈ 5 nW. RIN was found to be dominant in [29] as well. Finally, the results of the knife-edge measurement are reported. Figure 4.13 shows the dependence of the OCT peak's height on the lateral position. The orange line corresponds to the fit with the expected behavior in the Gaussian beam assumption, given by

$$f(D) = a(1 - \mathrm{erf}((D - z)f)) + b, \tag{4.2}$$

which is justified in Appendix I. The fit is validated by the $R^2 = 0.981$. The FWHM of its derivative allows us to estimate the lateral resolution, resulting in $\delta x = (3.3 \pm 0.5)$ mm.

Since the NIR OCT technique is well established, the preliminary analysis of the realized setup is reported in Appendix M. Its performance guarantees an axial resolution as good as 6.7 μm and a depth range around 2.4 mm, values compatible with commercially available OCT setups [1].

4.3.2 Comparison with simulations and interpretation of the results

The MIR-OCT setup shows severe limitations in terms of axial resolution and depth range. It is therefore fundamental to understand the main physical factors affecting its performance. To do so, I compared the experimental results of the characterization to the ones achieved by simulating the interference spectra.

The simulated spectra were calculated by taking into account the shape of the experimental non-interference spectrum, the theoretical interference pattern (given by Equation 1.25 for the NIR-OCT setup, by Equation 3.20 for the MIR-OCT setup), and the limited spectral resolution. The code is described in more detail in the Appendix N.

The simulated spectra were eventually analyzed to reconstruct the corresponding OCT spectra, using the same method employed for experimental data processing. Firstly, the validity of the simulation code was verified for the NIR OCT setup, as reported in

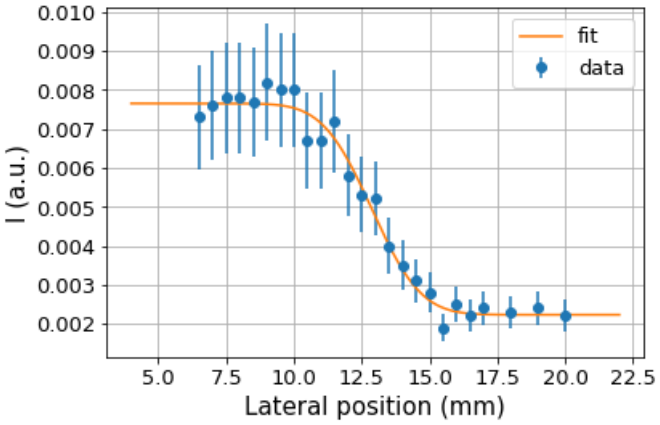

Figure 4.13: *The dependence of the OCT peak's height on the lateral position for the D-shaped mirror. The orange line corresponds to the fit with the expected behavior (Gaussian beam assumption).*

detail in Appendix N. In the case of the MIR OCT setup, this direct comparison might be misleading, since the chirping factor $\rho(\Omega)$ is assumed to be null in the simulation. It is thus more meaningful to compare the resulting OCT spectra, which are shown in Figure 4.14.

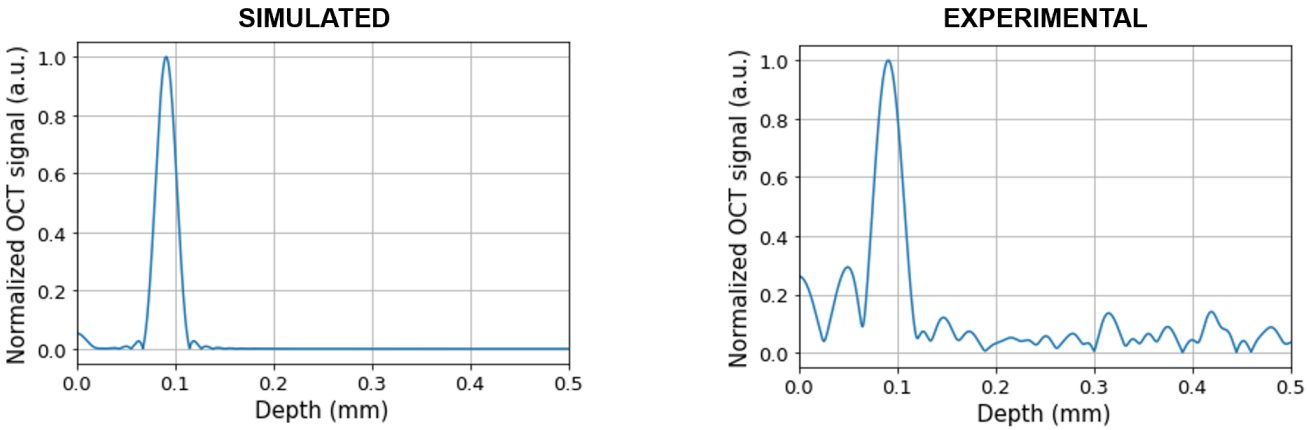

Figure 4.14: *Comparison between a simulated OCT spectrum and an experimental one for the MIR-OCT setup. The sample is the silver mirror $R \approx 1$, displaced at depth $z = 91$ μm*

We can see that the agreement is really good, with very similar FWHMs (experimental: 30 μm, simulated: 24 μm) despite the absence of any noise in the simulation. This allows us to conclude that the axial resolution is primarily limited by the signal

bandwidth and the usage of the Hanning window, with no significant losses of other nature.

Figure 4.15 shows the simulated roll-off curve for the MIR OCT. We can see that the decrease in the OCT signal is very similar to the experimental one

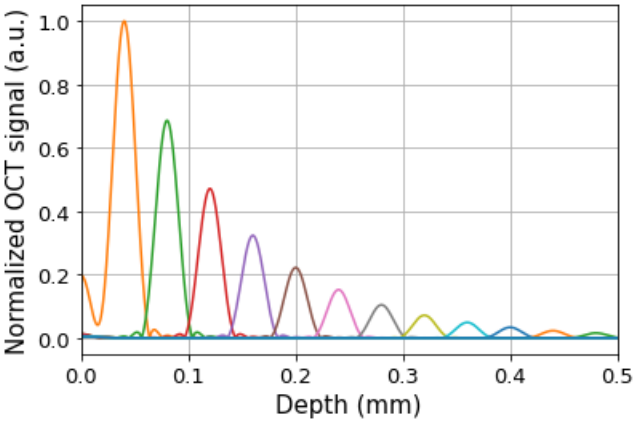

Figure 4.15: *Simulated roll-off for the MIR-OCT setup, assuming* $\delta\lambda_{sp} = 0.6$ nm.

Since the limited spectral resolution is the only element that can affect its behavior in the simulated data, we can affirm that it is the primary limitation in the experimental setup. This is confirmed by the simulated roll-off in Figure 4.16, in which $\delta\lambda_{sp}$ is assumed to be 0.3 nm.[2]

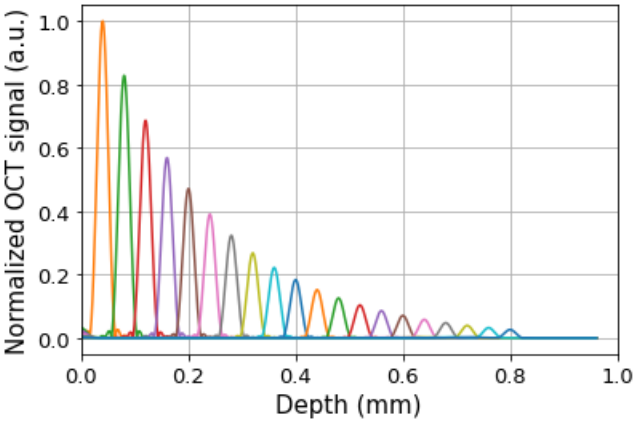

Figure 4.16: *Simulated roll-off for the MIR-OCT setup, assuming* $\delta\lambda_{sp} = 0.3$ nm.

[2]Experimentally, we can think of achieving a better spectral resolution by using a smaller core-size fiber. However, in principle, this will also affect the power conveyed to the OSA, possibly worsening the SNR. Therefore, the comparison done here can not be realized practically. The purpose is just to show that the spectral resolution is the main limitation of the depth range.

It is important to notice that other factors that may negatively affect the roll-off are the chirping factor and the noise, which are neglected in the simulation.

Eventually, it is important to notice that the worsening of the axial resolution at low and high depths does not appear in the simulated data for the MIR OCT setup. At low depths, this phenomenon is probably due to the presence of a residual DC component, which can be determined by both gray tracking effects during the measurement and the chirping. At high depths, instead, the large fluctuations observed suggest the phenomenon is mainly related to the decrease in the SNR.

4.3.3 Samples measurement results

Figure 4.17 shows the B-scan of the Al stepped sample, obtained with the MIR OCT setup.

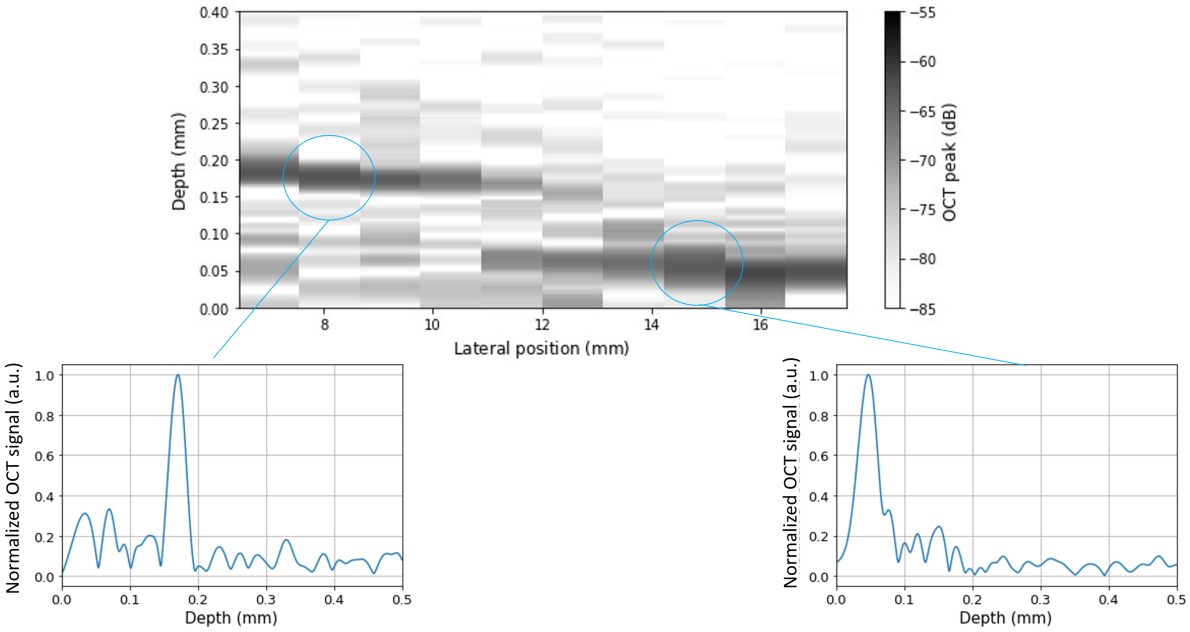

Figure 4.17: *B-scan of the stepped Al sample, obtained by using the MIR OCT setup. Two OCT spectra corresponding to different lateral positions are shown as well*

I added the A-scans corresponding to two lateral positions ($x = 8$ mm and $x = 15$ mm) for clarity. The SNR is sufficient to resolve the microstructure, operating sufficiently near the ZPD position. The broadening in the region on the right is due to the residual DC component, as already explained. We can also notice that the reflective layer appears slightly tilted (the surface is not perfectly perpendicular to the beam) and that both the peaks corresponding to the different heights appear between $x = 12$ mm and $x = 14$ mm

(owing to the macroscopic size of the idler beam). The step height can be calculated as the distance between the two surfaces. To obtain it, I first performed a linear fit of the left and right layers visible in the B-scan. The results are reported in Figure 4.18.

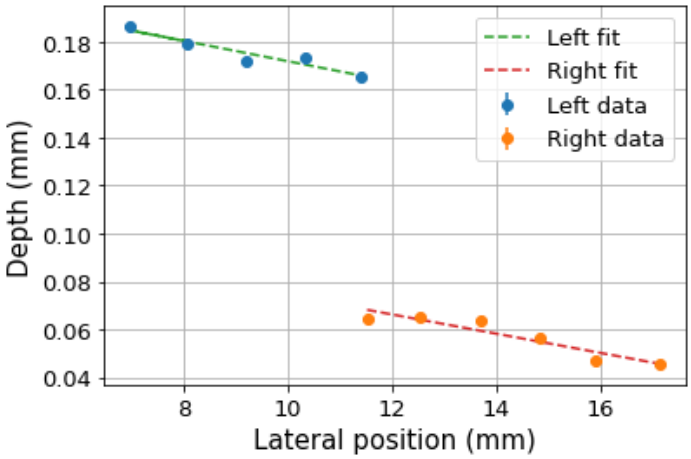

Figure 4.18: *The linear fits corresponding to the two surfaces of the Al stepped sample, obtained from the experimental B-scan measured with the MIR OCT setup.*

By using the two linear equations resulting from the fits to estimate the angular coefficient of the sample with respect to the beam direction and the distance between the layers, we get

$$L = (100 \pm 3)\mu\text{m}, \tag{4.3}$$

where the uncertainty was calculated as two times the one in Equation 4.1, i.e. the one associated with a generic distance measured using the MIR setup (difference of the peaks' positions)[3]. The B-scan was realized using the NIR OCT setup as well. The results are shown in Figure 4.19.

We can use the NIR OCT results to evaluate again the step height, proceeding analogously to the MIR case. We thus find

$$L = (94.7 \pm 0.6)\mu\text{m}, \tag{4.4}$$

This value is in very good agreement with the estimation obtained from the MIR OCT measurement, with the formal incompatibility of 2 μm being easily explainable by considering the bigger uncertainty associated with the positions in the left halves of the B-scans and the possible presence of small imperfections in the sample.

The thin Si layer measurements for the MIR OCT setup are shown in Figure 4.20.

[3]Rigorously, the uncertainty should be calculated starting from the ones associated with the fitting parameters. However, the calculation in this case resulted highly underestimated ≈ 0.3 μm.

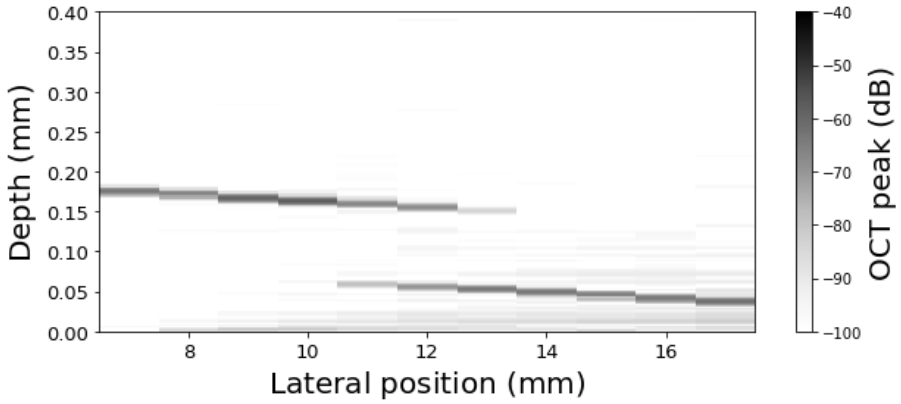

Figure 4.19: *B-scan of the stepped Al sample, obtained by using the NIR OCT setup.*

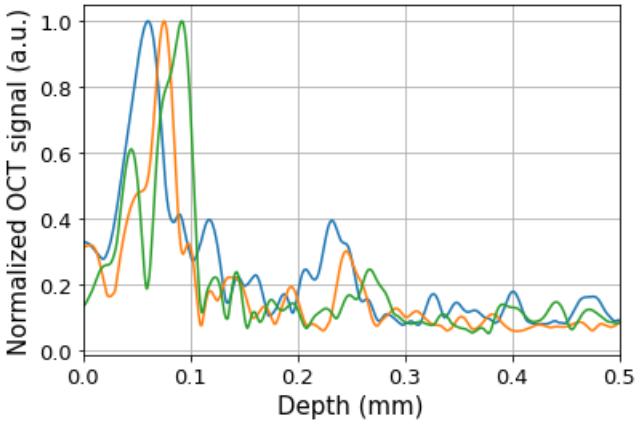

Figure 4.20: *Three A-scans of the thin Si layer, found thanks to the MIR OCT setup. The position of the sample was changed by steps of 20* μm.

Three OCT spectra, each one obtained after moving the sample of 20 μm, are shown. The doublet peak is clearly distinguishable and shows a displacement consistent with the mechanical one. The three estimations of the distance between the two peaks ((172 ± 3) μm, (171 ± 3) μm, and (177 ± 3) μm must be divided by the refractive index of the Si (furnished by [77].), giving

$$d_1 = (172 \pm 3)\mu\text{m}/n_{Si}(3\mu\text{m}) = (49.6 \pm 0.9)\mu\text{m}, \tag{4.5}$$

$$d_2 = (49.3 \pm 0.9)\mu\text{m}, \tag{4.6}$$

$$d_3 = (51.0 \pm 0.9)\mu\text{m}. \tag{4.7}$$

All these estimations are compatible with the expectation value.

The Si layer was measured with the NIR OCT setup as well. The resulting OCT

spectrum is reported in Figure 4.21 and the estimated thickness is

$$d = (198.1 \pm 0.6)\mu\text{m}/n_{Si}(1.5\mu\text{m}) = (54.5 \pm 0.2)\mu\text{m}. \tag{4.8}$$

This value is in good agreement with the ones estimated from the MIR OCT measurement. The formal disagreement might be easily explained by an underestimation of the uncertainties (also connected to the slight tilting of the sample with respect to the beam)

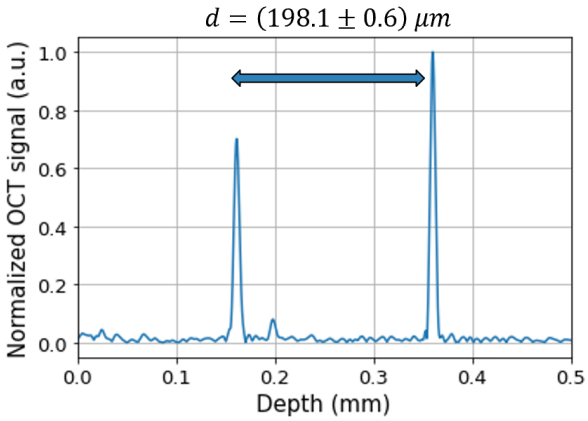

Figure 4.21: *A-scan of the thin Si layer, found thanks to the NIR OCT setup.*

4.3.4 MIR setup advantage: Ge window measurements

The MIR OCT setup should still be able to resolve the sample after inserting the Ge window along the idler arm, as previously explained. Figure 4.22 compares the resulting OCT spectra obtained using the silver mirror as a sample, before and after the Ge window mounting.

It clearly shows that the MIR OCT setup works as expected, being still able to identify the reflecting layer without any significant modification in terms of SNR or axial resolution.

Figure 4.23 shows instead the same comparison achieved using the NIR OCT setup.

The system fails completely to recognize the mirror after inserting the window, as expected. The absence of any peaks was verified for several depths of the sample. Moreover, I also confirmed that the alignment remained appropriate during the entire process since after removing the window it was easy to recover the mirror's OCT peak. We can then conclude that, while standard NIR OCT setups are intrinsically unable to work in the presence of Ge layers, the MIR OCT setup reported in this project is still operative under this condition.

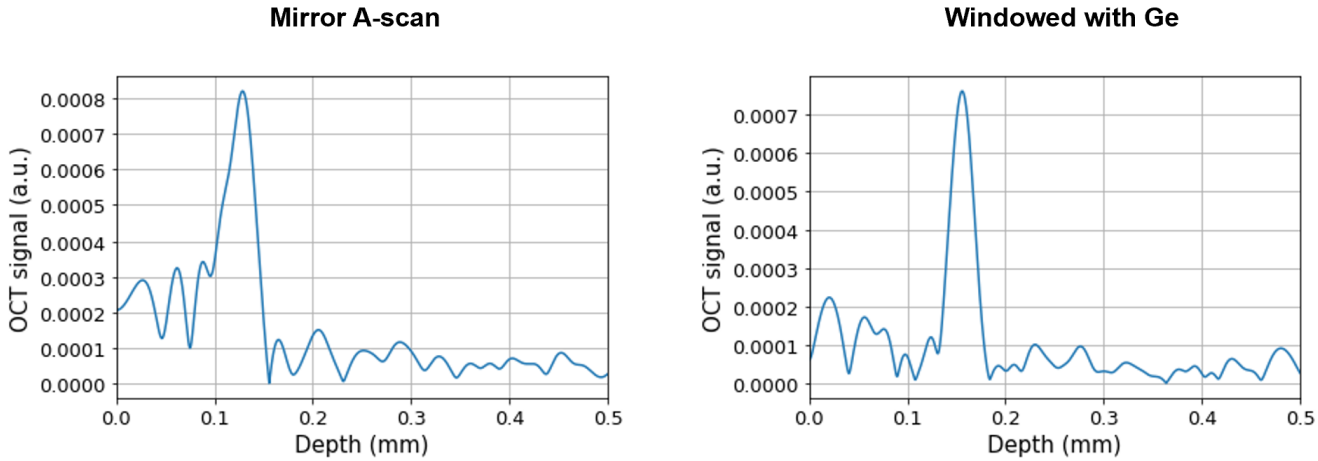

Figure 4.22: *The A-scans for the silver mirror measured with the MIR OCT setup, before and after the Ge window along the idler arm. The horizontal shift is not connected to the Ge thickness, since the mirror position was adjusted separately in the two cases.*

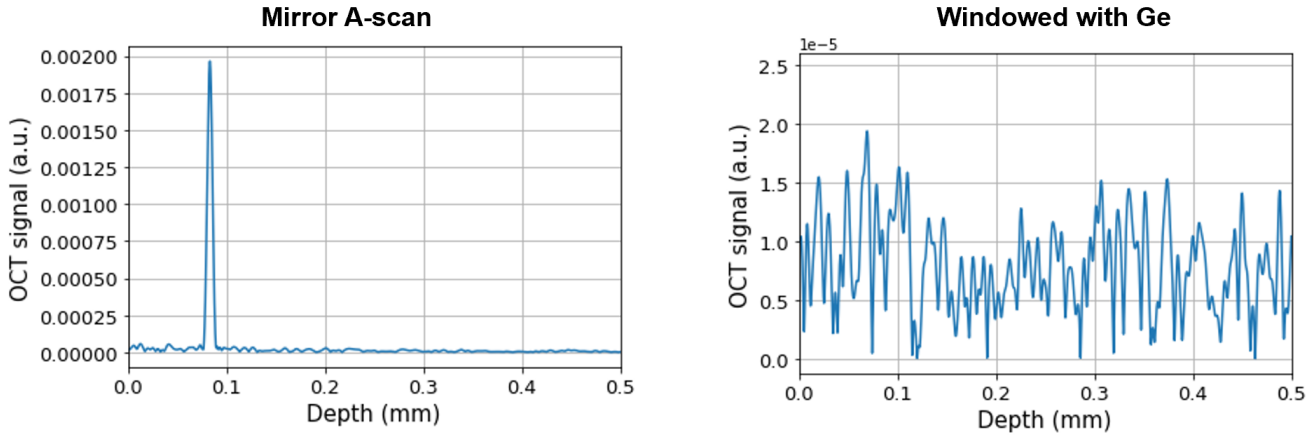

Figure 4.23: *The A-scans for the silver mirror measured with the NIR OCT setup, before and after the Ge window along the idler arm.*

To further prove this, I verified that the MIR OCT setup is even able to resolve the thin Si layer in the presence of the Ge window. The results are shown in Figure 4.24, in which the doublet of peaks with the expected distance is clearly recognizable despite the unfortunately quite high low-depth noise.

More in detail, the measured distance in this case is given by (181 ± 3) μm, corre-

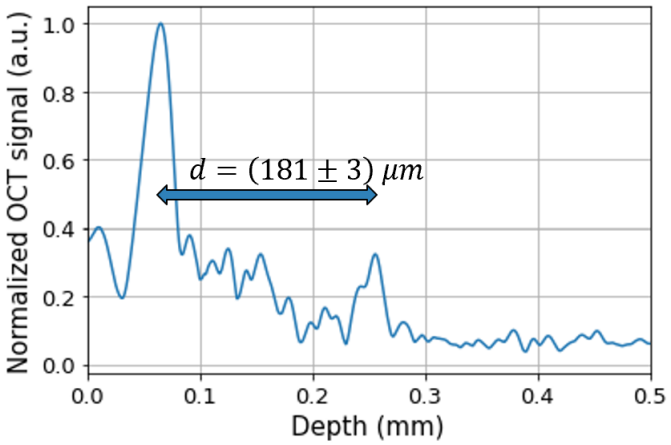

Figure 4.24: *The resulting averaged A-scan for the Si layer behind the Ge window, which was obtained by using the MIR OCT setup.*

sponding to a Si thickness of

$$d = (52.2 \pm 0.9)\mu\text{m}, \tag{4.9}$$

compatible with the previous results.

4.3.5 High-gain advantage

It is difficult to properly compare the performance of the current setup with the state-of-the-art one for the OCT with undetected photons in the low-gain regime [23]. The main reason is that the two setups suffer from different noise conditions (RIN and detector noise in my case, shot-noise level in Vanselow et al. case), have diverse fiber connection types (multimode fiber vs single-mode fiber), detection apparatus, and type of pump (pulsed laser versus CW laser). Thus, any direct comparison between the detected signal powers or the SNR would not be accurate. Nonetheless, the realized high-gain MIR OCT setup showed two remarkable novelties. The first one is the possibility to measure the average signal power directly using an ordinary Si power meter. The value found of circa 9 nW (for a pump power of ≈ 1 mW) already proves this achievement. The second one is related to the nature of the pump. My source is a ps-pulsed laser, with a repetition frequency of 1 kHz. This means that the measured signal photon number depends on the number of pulses reaching the detector during the measurement. For integration times shorter than the period of the laser (≈ 1 ms) and longer than the pulse duration (≈ 20 ps), we will have then a constant number of signal photons, therefore unchanged SNR. This condition is no longer valid for the low-gain case, in which the usage of the CW laser makes the number of signal photons linear with the integration time [23]. This is an important advantage for time-gated measurements, which are already performed with

frequencies up to 300000 A-scan/s (corresponding to an integration time smaller than 3 μs) using ultrahigh speed CMOS line scan camera for ophthalmology applications[80].

More decisive conclusions about the performances cannot be made without further investigations.

4.4 Conclusion and outlook

My project achieved the following main results:

- To the best of my knowledge, I realized the first experimental implementation for Fourier-domain OCT with MIR photons, operating in the PDC high-gain regime;
- The both designed and built setup relied on an aperiodically poled nonlinear crystal (apKTP), granting broad bandwidth and high-gain PDC spectra, with the idler centered at a wavelength of approximately 3 μm, in the MIR range;
- I performed the characterization of the setup's performance, demonstrating a typical SNR of approximately 40 dB, axial resolution as low as ≈ 30 μm, and depth range of approximately 320 μm.
- I successfully used the setup for some real interest samples. More specifically, I reconstructed the B-scan of a stepped-Al sample with a height of ≈ 100 μm and measured the thickness of a thin Si layer ≈ 50 μm thick;
- I built a classical NIR OCT setup to compare its performance to the MIR OCT one and verify the agreement between the measurements;
- I showed the advantage of operating with the MIR OCT setup over the NIR OCT one when dealing with the presence of a Ge window along the sample arm.

Significant improvements might be achieved by optimizing the crystal's design. By modifying the aperiodical profile function, we can provide broader PDC spectra, thus enhancing the axial resolution. Adopting a less common but more efficient windowing strategy (like the one suggested in [81]) could also positively affect the FWHM of the OCT peaks.

The lateral resolution can be upgraded by modifying the setup to the focusing geometry, thus focusing the idler beam into the sample instead of simply collimating it. However, this choice might decisively decrease the amount of signal and worsen the SNR. Since this effect cannot be simply compensated by increasing the pump power, due to the emergence of gray-tracking effects, further investigations are needed. The same can be stated for the depth range improvement. In principle, the OSA spectral resolution can be enhanced by employing smaller core-size fibers. However, this can also affect

the detected signal power and the SNR, finding the same condition as above. Again, a precise characterization of the trade-off between gray-tracking, pump power, and SNR is needed.

Scientific acknolewdgements

I deeply thank my supervisor, Prof. Francesco Minardi, and my co-supervisors, Prof. Maria Chekhova and Dr. Kazuki Hashimoto. Their fruitful indications and precious teaching were fundamental for realizing this thesis. I also thank the whole Chekhova's research group for their continuous support, Prof. D. B. Horoshko and Prof. M. I. Kolobov for developing the theoretical background for this work, Yoad Michael and Ziv Gefen for furnishing the nonlinear crystal, Michael Frosz and Azim-Onur Yazici for letting us use the FTIR spectrometer for samples inspection, and Kyoohyun Kim for letting us use the microscope to analyze the apKTP crystal.

Ringraziamenti

Non posso poi che ringraziare tutte le persone che, nel corso di questi anni, hanno scelto di darmi la loro vicinanza, il loro affetto, un supporto incondizionato rendendomi felice di quello che sono. Ringrazio la mia famiglia, mia madre Patrizia, mio padre Carlo Alberto, mia sorella Annaluce; mia zia Daniela, mio cugino Alessandro e mio zio Gianluca; ringrazio i miei compagni di liceo e di tante avventure Matteo, Chengxin, Marco e Cristiano; ringrazio le straordinarie persone con cui ho condiviso i miei anni a Bologna Davide, Rebecca, Giulia, Riccardo, Marco, Nicola e tutta la comunità collegiale. Ciò che mi avete donato è semplicemente impossibile da contraccambiare e per questo non posso che ricordarlo ogni volta che ne ho l'occasione, anche in questo piccolo traguardo.

Appendix A

Peak value of the OCT signal

We want to calculate the inverse FFT of Equation 1.29. In particular, we can focus on the cos term. Thus, we can write

$$\begin{aligned} i(q) &= \frac{1}{N}\sum_{n=0}^{N-1}\cos\left(\frac{2\pi n q_0}{N}\right)e^{i2\pi qn/N} \\ &= \frac{1}{2N}\sum_{n=0}^{N-1}e^{i2\pi qn/N}(e^{i2\pi nq_0/N}+e^{-i2\pi nq_0/N}) \\ &= \frac{1}{2N}\sum_{n=0}^{N-1}(e^{i2\pi(q+q_0)/N})^n+(e^{i2\pi(q-q_0)/N})^n \\ &= \frac{1}{2N}\sum_{n=0}^{N-1}(\frac{1-e^{i2\pi(q+q_0)}}{1-e^{i2\pi(q+q_0)/N}}+\frac{1-e^{i2\pi(q-q_0)}}{1-e^{i2\pi(q-q_0)/N}}) \end{aligned} \tag{A.1}$$

This expression has a peak for positive q when the second term's denominator is null, thus for $q = q_0$ (q_0 can be then interpreted as the position of the reflecting layer). Using L'Hopital's rule to calculate the limit of the second term for $q \to q_0$, we get

$$\begin{aligned} i(q_0) &= \frac{1}{2N}\sum_{n=0}^{N-1}\lim_{q\to q_0}\frac{1-e^{i2\pi(q-q_0)}}{1-e^{i2\pi(q-q_0)/N}} \\ i(q_0) &= \frac{1}{2N}\sum_{n=0}^{N-1}\frac{-2\pi i}{-2\pi i/N} \\ i(q_0) &= \frac{1}{2} \end{aligned} \tag{A.2}$$

Using this result, we find

$$N_{sig}(n) = \frac{1}{2}K(k_n)\mathrm{VIS} \tag{A.3}$$

Appendix B

Correlation of Real and Imaginary Part of the OCT Signal

We have to show that the real part and the imaginary part of $i_n(q)$, defined as in Equation 1.33, are uncorrelated. Their correlation is given by

$$
\begin{aligned}
&\langle \mathfrak{Re}(i_n)\mathfrak{Im}(i_n)\rangle = \\
&= \frac{1}{N^2}\langle \sum_{n=0}^{N-1} \mathbf{N}(n)\cos\left(\frac{2\pi nq}{N}\right)\sum_{l=0}^{N-1}\mathbf{N}(l)\sin\left(\frac{2\pi lq}{N}\right)\rangle \\
&= \frac{1}{N^2}\sum_{n=0}^{N-1}\sum_{l=0}^{N-1}\cos\left(\frac{2\pi nq}{N}\right)\sin\left(\frac{2\pi lq}{N}\right)\langle \mathbf{N}(n)\mathbf{N}(l)\rangle \\
&= \frac{1}{N^2}\sum_{n=0}^{N-1}\sum_{l=0}^{N-1}\cos\left(\frac{2\pi qn}{N}\right)\sin\left(\frac{2\pi ql}{N}\right)\sigma^2_{\mathbf{N}}\delta(n-l) \\
&= \frac{\sigma^2_{\mathbf{N}}}{N^2}\sum_{n=0}^{N-1}\cos\left(\frac{2\pi qn}{N}\right)\sin\left(\frac{2\pi qn}{N}\right) \\
&= \frac{\sigma^2}{2N^2}\sum_{n=0}^{N-1}\sin\left(\frac{4\pi qn}{N}\right) \qquad \text{(B.1)}
\end{aligned}
$$

which is 0 for q, n integers.

Appendix C

Variance of Real and Imaginary Part of OCT Signal

We have to calculate the variance for the real part of $i_n(q)$ defined as in 1.33. We can proceed as follows:

$$\begin{aligned}
&\sigma^2_{\mathfrak{Re}[i_n(q)]} = \langle(\mathfrak{Re}[i_n(q)])^2\rangle \\
&= \frac{1}{N^2}\langle\sum_{n=0}^{N-1}\mathbf{N}(n)\cos\left(\frac{2\pi qn}{N}\right)\sum_{l=0}^{N-1}\mathbf{N}(l)\cos\left(\frac{2\pi ql}{N}\right)\rangle \\
&= \frac{1}{N^2}\sum_{n=0}^{N-1}\sum_{l=0}^{N-1}\cos\left(\frac{2\pi qn}{N}\right)\cos\left(\frac{2\pi ql}{N}\right)\langle\mathbf{N}(n)\mathbf{N}(l)\rangle \\
&= \frac{1}{N^2}\sum_{n=0}^{N-1}\sum_{l=0}^{N-1}\cos\left(\frac{2\pi qn}{N}\right)\cos\left(\frac{2\pi ql}{N}\right)\sigma_N^2\delta(n-l) \\
&= \frac{\sigma_N^2}{N^2}\sum_{n=0}^{N-1}\cos^2(\frac{2\pi qn}{N})
\end{aligned} \tag{C.1}$$

Since $\sigma^2_{\mathbf{N}} = N_{noise}(n) = K_{tot}/N$, and the sum goes to $\frac{N}{2}$, we found the desired result.

Appendix D

Explicit calculation of $\langle N(\Omega, L)\rangle$

Firstly, we recall that the creation/annihilation operators fulfill

$$[\hat{a}(\Omega, z), \hat{a}(\Omega^{'}, z)] = [\hat{a}^{\dagger}(\Omega, z), \hat{a}^{\dagger}(\Omega^{'}, z)] = 0 \tag{D.1}$$

$$\hat{a}^{\dagger}(\Omega, z)\hat{a}(\Omega, z) = \hat{N}(\Omega, z) \tag{D.2}$$

$$[\hat{a}(\Omega, z), \hat{a}^{\dagger}(\Omega^{'}, z)] = \delta(\Omega - \Omega^{'}) \tag{D.3}$$

Secondly, we can notice that the expectation value must be calculated on the wave function at the beginning of the crystal, where we have no PDC. Thus

$$\big|\psi(t=0)\big\rangle = \big|0(\Omega)\big\rangle \tag{D.4}$$

We can now proceed with the calculation (already considering $\Omega = \Omega^{'}$), using the expression for $\hat{a}(\Omega, L)$ given by 2.53

$$\begin{aligned}
&\langle N(\Omega, L)\rangle = \langle 0|\, \hat{a}^{\dagger}(\Omega, L)\hat{a}(\Omega, L)\, |0\rangle = \\
&= \langle 0|\, (U^{*}(\Omega)\hat{a}^{\dagger}(\Omega, 0) + V^{*}(\Omega)\hat{a}(-\Omega, 0))(U(\Omega)\hat{a}(\Omega, 0) + V(\Omega)\hat{a}^{\dagger}(-\Omega, 0))\, |0\rangle = \\
&= \langle 0|\, |U(\Omega)|^2\hat{a}^{\dagger}(\Omega, 0)\hat{a}(\Omega, 0) + |V(\Omega)|^2\hat{a}(-\Omega, 0)\hat{a}^{\dagger}(-\Omega, 0)\, |0\rangle = \\
&= \langle 0|\, |U(\Omega)|^2\hat{N}(\Omega)\, |0\rangle + \langle 0|\, |V(\Omega)|^2([\hat{a}(\Omega, z), \hat{a}^{\dagger}(\Omega, z)] + \hat{a}^{\dagger}(-\Omega, 0)\hat{a}(-\Omega, 0))\, |0\rangle = \\
&= \langle 0|\, |V(\Omega)|^2\, |0\rangle + \langle 0|\, \hat{N}(-\Omega, 0)\, |0\rangle = \\
&= |V(\Omega)|^2
\end{aligned} \tag{D.5}$$

Remembering the expression for V given by Equation 2.56, we find the desired result.

Appendix E

Explicit calculation of $\hat{a}(\Omega, z_{out})$

We can simply replace the explicit expressions for $\hat{a}(\Omega, L+d)$, $\hat{a}(\Omega, L)$ in the one for $\hat{a}(\Omega, z_{out})$. We then get

$$\begin{aligned}
&\hat{a}(\Omega, z_{out}) = U_2(\Omega)T(\Omega)\hat{a}(\Omega, L) + U_2(\Omega)R(\Omega)\hat{a}_{vac}(\Omega) + \\
&+ V_2(\Omega)T^*(-\Omega)\hat{a}^\dagger(-\Omega, L) + V_2(\Omega)R^*(-\Omega)\hat{a}^\dagger_{vac}(-\Omega) = \\
&= U_2(\Omega)T(\Omega)U_1(\Omega)\hat{a}(\Omega, 0) + U_2(\Omega)T(\Omega)V_1(\Omega)\hat{a}^\dagger(-\Omega, 0) + \\
&+ V_2(\Omega)T^*(-\Omega)U_1^*(-\Omega)\hat{a}^\dagger(-\Omega, 0) + V_2(\Omega)T^*(-\Omega)V_1^*(-\Omega)\hat{a}(\Omega, 0) + \\
&+ U_2(\Omega)R(\Omega)\hat{a}_{vac}(\Omega) + V_2(\Omega)R^*(-\Omega)\hat{a}^\dagger_{vac}(-\Omega) = \\
&= \hat{a}(\Omega, 0)U_{int}(\Omega) + \hat{a}^\dagger(-\Omega, 0)V_{int}(\Omega) + +U_2(\Omega)R(\Omega)\hat{a}_{vac}(\Omega) + V_2(\Omega)R^*(-\Omega)\hat{a}^\dagger_{vac}(-\Omega)
\end{aligned} \tag{E.1}$$

as used in the main text.

Appendix F

Explicit calculation of $S(\omega_0 + \Omega)$

We have to calculate the expectation value of the number operator. Again, the state at $z = 0$ is expected to have no photons at the modes $\omega_0 + \Omega$, $\omega_0 - \Omega$. Therefore,

$$
\begin{aligned}
&S(\omega_0+\Omega) = \langle 0|\, \hat{a}^\dagger(\Omega, z_{out})\hat{a}(\Omega, z_{out})\, |0\rangle = \\
&= \langle 0|\, (U^*_{int}(\Omega)\hat{a}^\dagger(\Omega,0) + V^*_{int}(\Omega)\hat{a}(-\Omega,0) + U^*_2(\Omega)R^*(\Omega)\hat{a}^\dagger_{vac}(\Omega) + V^*_2(\Omega)R(-\Omega)\hat{a}_{vac}(-\Omega)) \\
&(U_{int}(\Omega)\hat{a}(\Omega,0) + V_{int}(\Omega)\hat{a}^\dagger(-\Omega,0) + U_2(\Omega)R(\Omega)\hat{a}_{vac}(\Omega) + V_2(\Omega)R^*(-\Omega)\hat{a}^\dagger_{vac}(-\Omega))\, |0\rangle = \\
&= \langle 0|\, |V_{int}(\Omega)|^2\hat{a}(-\Omega,0)\hat{a}^\dagger(-\Omega,0) + |V_2(\Omega)|^2|R(-\Omega)|^2\hat{a}_{vac}(-\Omega)\hat{a}^\dagger_{vac}(-\Omega))\, |0\rangle = \\
&= \langle 0|\, |V_{int}(\Omega)|^2(1+\hat{N}(-\Omega,0)) + |V_2(\Omega)|^2|R(-\Omega)|^2(1+\hat{N}_{vac}(-\Omega))\, |0\rangle = \\
&= |V_{int}(\Omega)|^2 + |V_2(\Omega)|^2|R(-\Omega)|^2
\end{aligned}
\tag{F.1}
$$

Remembering $V_{int}(\Omega) = U_2(\Omega)V_1(\Omega)T(\Omega) + V_2(\Omega)U^*_1(-\Omega)T^*(-\Omega)$, we find

$$
\begin{aligned}
&|V_{int}|^2(\Omega) = (U^*_2(\Omega)V^*_1(\Omega)T^*(\Omega) + V^*_2(\Omega)U_1(-\Omega)T(-\Omega))(U_2(\Omega)V_1(\Omega)T(\Omega) + V_2(\Omega)U^*_1(-\Omega)T^*(-\Omega)) = \\
&= |U_2(\Omega)|^2|V_1(\Omega)|^2|T(\Omega)|^2 + |V_2(\Omega)|^2|U_1(-\Omega)|^2|T(-\Omega)|^2 + \\
&+ U^*_1(-\Omega)U^*_2(\Omega)V^*_1(\Omega)V_2(\Omega)T^*(\Omega)T^*(-\Omega) + U_1(-\Omega)U_2(\Omega)V_1(\Omega)V^*_2(\Omega)T(\Omega)T(-\Omega)
\end{aligned}
\tag{F.2}
$$

This expression is extremely long and complex, so it is convenient to treat various terms separately. Firstly, we recall that various U_n, V_n terms satisfy

$$U_n(\Omega) = e^{i[\psi^L_n(\Omega) - \psi^0_n(\Omega) + \kappa_n(\Omega)]}\cosh r(\Omega) \tag{F.3}$$

$$V_n(\Omega) = e^{i[\psi^L_n(\Omega) + \psi^0_n(\Omega) + \kappa_n(\Omega)]}\sinh r_n(\Omega) \tag{F.4}$$

where r_n,ψ_n^L,ψ_n^0 are even, κ odd in Ω. We also recall that the pump is assumed to be undepleted, thus $r_1 = r_2 = r$ Considering terms containing them separately we get

$$|U_2(\Omega)|^2|V_1(\Omega)|^2 = \cosh^2 r(\Omega)\sinh^2 r(\Omega) = \frac{\sinh^2 2r(\Omega)}{4} \tag{F.5}$$

$$|V_2(\Omega)|^2|U_1(-\Omega)|^2 = \sinh^2 r(\Omega)\cosh^2 r(-\Omega) = \frac{\sinh^2 2r(\Omega)}{4} \tag{F.6}$$

$$\begin{aligned} &U_1^*(-\Omega)U_2^*(\Omega)V_1^*(\Omega)V_2(\Omega) = e^{-i[\psi_1^L(\Omega)-\psi_1^0(\Omega)-\kappa_1(\Omega)]}\cosh r(\Omega)e^{-i[\psi_2^L(\Omega)-\psi_2^0(\Omega)+\kappa_2(\Omega)]}\cosh r(\Omega) \\ &e^{-i[\psi_1^L(\Omega)+\psi_1^0(\Omega)+\kappa_1(\Omega)]}\sinh r(\Omega)e^{i[\psi_2^L(\Omega)\psi_2^0(\Omega)+\kappa_2(\Omega)]}\sinh r(\Omega) = \\ &= e^{-i[2\psi_1^L(\Omega)-2\psi_2^0(\Omega)]}\frac{\sinh^2 2r(\Omega)}{4} \end{aligned} \tag{F.7}$$

$$\begin{aligned} &U_1(-\Omega)U_2(\Omega)V_1(\Omega)V_2^*(\Omega) = e^{i[\psi_1^L(\Omega)-\psi_1^0(\Omega)-\kappa_1(\Omega)]}\cosh r(\Omega)e^{i[\psi_2^L(\Omega)-\psi_2^g(\Omega)+\kappa_2(\Omega)]}\cosh r(\Omega) \\ &e^{i[\psi_1^L(\Omega)+\psi_1^0(\Omega)+\kappa_1(\Omega)]}\sinh r(\Omega)e^{-i[\psi_2^L(\Omega)+\psi_2^0(\Omega)+\kappa_2(\Omega)]}\sinh r(\Omega) = \\ &= e^{i[2\psi_1^L(\Omega)-2\psi_2^0]}\frac{\sinh^2 2r(\Omega)}{4} \end{aligned} \tag{F.8}$$

Let us now focus on the behavior of $T(\Omega) = T_A(\Omega)e^{i\phi(\Omega)}$. T_A is the transmittance amplitude acquired by the field at $\omega_0 + \Omega$, $\phi(\Omega)$ the total phase. Understanding the behavior of $T_A(\Omega)$ is simple: in most cases, just the idler passes through a sample. Therefore $T_A(\Omega) = 1$,$T_A(-\Omega) = T_A$. $\phi(\Omega)$ has a common contribution for both signal and idler instead, given by their common path. If we call this distance L_0, the corresponding $\phi_0(\pm\Omega) = \frac{L_0}{c}\Omega$. Additionally, for the idler, we have to take into account the passage through the sample. We can express this term by adding $\phi^{add}(-\Omega) = \tau(\omega_0-\Omega)+\phi_s(-\Omega)$. In the OCT case, τ is given by $2z_s/c$. More compactly, we can write

$$\phi(\Omega) = \tau_0\Omega + \tau(\omega_0+\Omega)\theta(-\Omega) + \phi_0(\Omega)\theta(-\Omega) \tag{F.9}$$

with $\theta(\Omega)$ being the step function

$$\begin{cases} \theta(\Omega) & = 1 \quad \Omega > 0 \\ \theta(\Omega) & = 0 \quad otherwise \end{cases} \tag{F.10}$$

Now we can rewrite explicitly the terms in $T(\Omega)$ and $R(\Omega)$ (exploiting $|T(\Omega)|^2+|R(\Omega)|^2 = 1$)

$$|T(\Omega)|^2 = 1 \tag{F.11}$$
$$|T(-\Omega)|^2 = T_A^2 \tag{F.12}$$
$$T^*(\Omega)T^*(-\Omega) = T_A e^{-i\tau_0\Omega} e^{-i(-\tau_0\Omega+\tau(\omega_0-\Omega)+\phi_s(-\Omega))} = \\ = T_A e^{-i(\tau(\omega_0-\Omega)+\phi_s(-\Omega))} \tag{F.13}$$
$$T(\Omega)T(-\Omega) = T_A e^{i\tau_0\Omega} e^{i(-\tau_0\Omega+\tau(\omega_0-\Omega)+\phi_s(-\Omega))} = \\ = T_A e^{i(\tau(\omega_0-\Omega)+\phi_s(-\Omega))} \tag{F.14}$$
$$|R(-\Omega)|^2 = 1 - T_A^2 \tag{F.15}$$

Finally, combining everything we can write:

$$|V_{int}(\Omega)|^2 + |V_2(\Omega)|^2|R(-\Omega)|^2 = \frac{\sinh^2 2r(\Omega)}{4} + \frac{\sinh^2 2r(\Omega)}{4}T_A^2 + e^{-i[2\psi_1^L(\Omega)-2\psi_2^0(\Omega)]} \\ \frac{\sinh^2 2r(\Omega)}{4}T_A e^{-i(\tau(\omega_0-\Omega)+\phi_s(-\Omega))} + e^{i[2\psi_1^L(\Omega)-2\psi_2^0]}\frac{\sinh^2 2r(\Omega)}{4}T_A e^{i(\tau(\omega_0-\Omega)+\phi_s(-\Omega))} + \sinh^2 r(\Omega)(1-T_A^2) = \\ = \frac{\sinh^2 2r}{4}(1 + T_A^2 + T_A e^{-i[\tau(\omega_0-\Omega)+(\phi_s(-\Omega)+2\psi_1^L(\Omega)-2\psi_2^0(\Omega))]} + \\ + e^{+i[\tau(\omega_0-\Omega)+(\phi_s(-\Omega)+2\psi_1^L(\Omega)-2\psi_2^0(\Omega))]}) + \sinh^2 r(\Omega)(1-T_A^2) \tag{F.16}$$

We introduce $\rho(\Omega) = \phi_s(\Omega) + 2\psi_1^L(\Omega) - 2\psi_2^0(\Omega)$, then

$$S(\omega_0+\Omega) = \frac{\sinh^2 2r}{2}\left(\frac{1+T_A^2}{2} + T_A\cos\big(\tau(\omega_0-\Omega)+\rho(\Omega)\big)\right) + \sinh^2 r(\Omega)(1-T_A^2) \tag{F.17}$$

Appendix G

NIR-OCT setup

The realized classical NIR OCT setup is illustrated in Figure G.1.

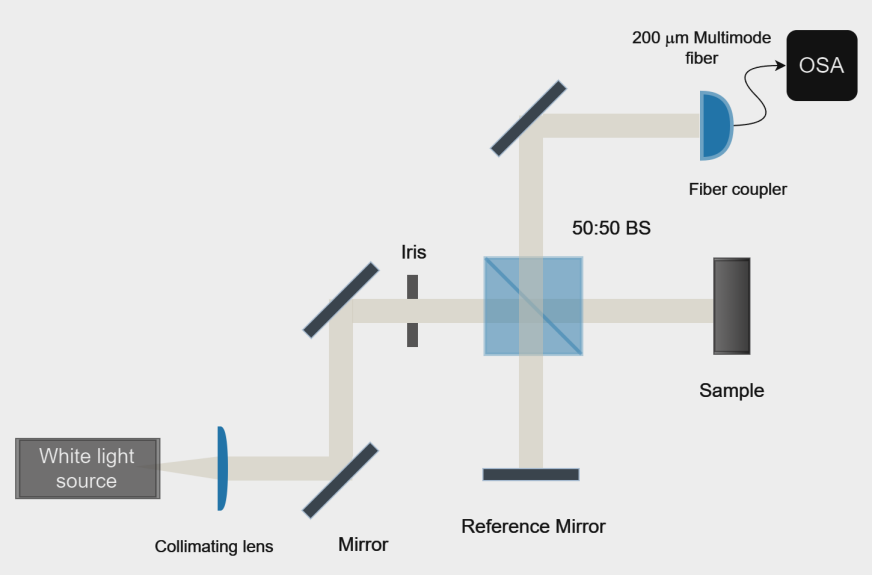

Figure G.1: *The optical setup realized to perform classical NIR-OCT.*

In this setup, the source is a broadband white light source (Thorlabs, SLS201L/M), which allows probing the sample up to a central wavelength of 1.5 μm, the standard one in commercially available NIR OCT setups [1]. The beam is then collimated and sent to a 50:50 beam splitter, the heart of the interferometer. An iris is placed along this path, to achieve a beam size comparable to that of the MIR-OCT setup. The light is then divided into reference and sample arms. the reference arm ends with a flat silver mirror, while the sample arm with the sample (mounted on a two-axis stage). Reflected light from both arms is sent back to the beam splitter and conveyed to the fiber coupler, which

is connected to the spectrometer via an optical fiber as the one used for the MIR-OCT case.

Appendix H

Description of the alignment procedure for the MIR OCT setup

The alignment procedure consists of the following main steps:

1. Ensure the sample is securely mounted along the idler arm.

2. Optimize the alignment of the crystal, reference mirror, and detection part (spatial filter + fiber coupler). The crystal position is crucial in both the z and x directions. Adjusting the z-position modifies the focusing point of the lens on the crystal, slightly altering the OPA process. The x-position must be carefully chosen to avoid defective regions of the crystal or to compensate for gray-tracking effects.

3. Install a short-pass filter (cutoff wavelength at 600 nm) along the reference path. This filter blocks the signal beam along the reference arm, leaving only the pump beam. The detected signal power at the output of the interferometer will then be determined solely by the DFG process between the back-reflected pump and the idler.

4. Adjust the sample's orientation and position to maximize the DFG process between the idler and the pump. Both the inclination and the z-position are critical in this step.

5. Remove the short-pass filter and monitor the output spectrum of the interferometer in real-time while slowly moving the z-position of the sample (minimum speed and acceleration for the employed motorized stage are 0.001 mm/s and 0.004 mm^2/s, respectively). As you approach the ZPD, the interference pattern becomes clearly distinguishable.

6. Fine-tune the alignment to maximize the visibility of the interference pattern.

The alignment procedure was realized while using a visible spectrometer instead of the OSA (Avantes, Avaspec 3648). The main reason is its fast data sampling, which allows for real-time monitoring. However, its limited spectral resolution makes it impossible to correctly resolve the interference fringes, making the usage of the OSA for the measurement indispensable.

It is worth explaining that, to connect the Avaspec 3648 to the fiber coupler, an additional connection consisting of an FCPC to SMA adapter and an additional multimode fiber with 400 mu$m$ core size was needed.

Appendix I

Knife edge measurement

The knife edge measurement is a general methodology that allows determining the optical beam size up to the micrometric range [82]. The fundamental principle is using a thin object (the knife edge) to partially block the beam. In this way, we modify the transmitted optical power P, which will depend on the position of the object. By slightly moving the knife edge in one direction, we can scan the different P values: the shape of the curve will be related to the beam size. This is mathematically equivalent to dealing with a non-completely reflective sample (like the D-shaped mirror) and measuring the reflected power while moving it. From Equation 1.30, we know that the OCT signal is proportional to the detected interference intensity, thus to the power. The dependence of I on the lateral position should be therefore completely equivalent to the power's one. In my specific case, we additionally have to take into account that we are working with an undetected photons scheme, thus without directly measuring the idler. Nonetheless, Equation 3.20 suggests that the linear proportionality between I and the back-reflected power of the idler is preserved. This means that changes in the idler power, which we cannot measure directly, are reflected proportionally in the OCT signal intensity that we do measure.

Now, let us consider the simplest case of a Gaussian beam. The intensity is then described by the Equation 1.44, which depends on the coordinates z, along the propagation of the beam, and r, along the radial direction. In the knife-edge measurement, the coordinate z is fixed, thus we can take $w(z) = w$ and decompose $r^2 = x^2 + y^2$. Calling $\frac{P}{\pi w^2/2} = I_0$, we find

$$I(x, y) = I_0 e^{-\frac{2x^2+2y^2}{w_x^2+w_y^2}} \tag{I.1}$$

with w_x, w_y being the components of w along x and y respectively. If we now work in the coordinate system centered in the middle of the beam, we can easily write the power

before putting the knife edge as

$$P = \int_{-\infty}^{+\infty}\int_{-\infty}^{+\infty} \mathrm{d}x\mathrm{d}y I(x,y) = I_0 \int_{-\infty}^{+\infty} \mathrm{d}x e^{-\frac{2x^2}{w_x^2}} \int_{-\infty}^{+\infty} \mathrm{d}y e^{-\frac{2y^2}{w_y^2}} \tag{I.2}$$

We now displaced the knife edge, considering just the motion along the x-axis for simplicity (it can be easily generalized). When the knife edge is at the position $x = D$, we have

$$P(D) = I_0 \int_{D}^{+\infty} \mathrm{d}x e^{-\frac{2x^2}{w_x^2}} \int_{-\infty}^{+\infty} \mathrm{d}y e^{-\frac{2y^2}{w_y^2}} \tag{I.3}$$

Calculating the integrals, we find

$$P(D) = \frac{I_0 w_x w_y \pi}{4} \mathrm{erfc}(\frac{D\sqrt{2}}{w_x}) \tag{I.4}$$

with the coefficient being the transmitted power without the knife edge P_0, erfc $= 1 -$ erf. To take into account the possible displacement between the coordinate system and the position $x = D_0$ of the beam, we can simply rewrite

$$P(D) = P_0 \mathrm{erfc}(\frac{(D - D_0)\sqrt{2}}{w}) \tag{I.5}$$

where the subscript of the beam radius was removed for generalization. If we now calculate the derivative of the Equation I.5, we find

$$\begin{aligned} &\frac{\mathrm{d}}{\mathrm{d}D} P_0 \mathrm{erfc}(\frac{(D - D_0)\sqrt{2}}{w}) = -P_0 \frac{\mathrm{d}}{\mathrm{d}D} \mathrm{erf}(\frac{(D - D_0)\sqrt{2}}{w}) = \\ &= -P_0(-\frac{2}{\sqrt{\pi}} e^{-\frac{2(D-D_0)^2}{w^2}}) \frac{\sqrt{2}}{w} = \frac{2P_0}{\sqrt{2\pi}\frac{w}{2}} e^{-\frac{(D-D_0)^2}{2\frac{w^2}{4}}} \end{aligned} \tag{I.6}$$

which is the expression of a Gaussian with $\sigma = \frac{w}{2}$. Thus, its FWHM will be

$$\mathrm{FWHM} = 2\sqrt{2\ln 2}\sigma = \sqrt{2\ln 2} w \tag{I.7}$$

compatible with the definition of the lateral resolution given in Equation 1.45.

This treatise shows that if we reconstruct the behavior in Equation I.5, we can find the lateral resolution as the FWHM of its derivative. The fit function was chosen to be

$$f(D) = a(1 - \mathrm{erf}((D - z) * f)) + b \tag{I.8}$$

which is perfectly equivalent to I.5 with an additional offset factor to take into account possible experimental shiftings.

The uncertainty on the FWHM was calculated using the confidence intervals of the parameters resulting from the fit. Since an analytical expression for the uncertainty

is difficult to find, I realized a simple Montecarlo simulation, producing 10000 $f(D)$ functions with the parameters a, b, z, and f randomly distributed within their confidence intervals. Eventually, I calculated for each one the FWHM of the derivative, finding its standard deviation. This value was chosen as the uncertainty associated with the estimation of the lateral resolution.

Appendix J

Details for power meter and spectrometers settings

It is important to specify the settings chosen for the two main measurement instruments: the Si power meter and the two spectrometers.

The S130VC power meter model operates in the range $200-1100$ nm. It is equipped with a $15-$Hz radio-frequency (RF) low-pass filtering, which extends the usual power range (500 pW-0.5 mW) up to 50 mW. Since the typical pump power in my case was around 1 mW, I employed the filter for all measurements.

The Avaspec 3648 operates in the wavelength range of $(250-1100)$ nm, thus covering the whole signal spectrum for the used apKTP. The main feature I have exploited for my project is its fast data sampling [83]. In particular, I set an integration time of 100 ms (corresponding to circa 10 spectra/s).

The AQ6374 OSA is a high-performance spectrometer, ideal for the precise measurement of the interfering signal spectra. The main parameters I considered for the project were:

- Span: the sampled interval of wavelengths. For the MIR-OCT setup, it was chosen based on the non-interference spectrum shape $(620-650)$ nm; for the NIR-OCT setup, it was chosen to achieve a central probing wavelength and an axial resolution comparable to those of commercially available OCT systems $(1300-1700)$ nm.

- Spectral resolution: This parameter was dictated by the core size of the multimode fiber, according to the User's manual [78]. For my 200 μm core fiber, the optimal setting spectral resolution is $\delta\lambda_{sp} = 0.5$ nm. The actual spectral resolution is set according to the monochromator slit width (so depending on the measured central wavelength), thus it may be slightly different than the setting one [78]. It can be read directly on the OSA and, in my case, was 0.6 nm for the MIR-OCT setup, 0.42 nm for the NIR-OCT one.

- Sampling points: This parameter determines the number of sampling points within the chosen span, thus affecting the Nyquist frequency. For both MIR-OCT and NIR-OCT setups, I chose to operate with a sampling period of 0.1 nm. Using Equation 1.40), the maximum depth ranges can be calculated: ≈ 998 μm for the MIR-OCT setup, ≈ 5625 μm for the NIR-OCT setup. I will show that both these values are significantly larger than the actual depth ranges determined from the roll-off curves: therefore, the Nyquist condition is surely satisfied.

- Sensitivity setting: The AQ6374 can provide high-sensitivity measurements by switching the sensor accordingly to the sensitivity mode chosen and the detected range of wavelengths [78]. I chose to use HIGH2 mode. This modality automatically switches between the short-wavelength sensor (operating in the range $350 - 900$ nm) and the wide-band sensor (operating in the range $1000 - 1750$ nm).

Finally, it is worth stressing that the dark counts were evaluated and properly subtracted when using both spectrometers.

Appendix K

Data analysis procedure

The adopted data analysis procedure to reconstruct the OCT spectra starting from the sampled patterns is inspired by the one available in the Supplementary material of [23]. It consists of the following steps:

1. Preliminary comparison of the interference and non-interference spectra. In my case, the non-interference spectrum was sampled three times for each different sample, to compensate for possible variations of the $S(k)$ shape. In this case, we might lose the direct proportionality between the height of the OCT peak and the square root of the reflectivity of the sample, as explained in the theory part. However, since I am interested just in the A-scan reconstruction it should be irrelevant. Already at this stage, it is possible to calculate the total signal power by simply adding all $y-$axis entries (since the "show power" mode was chosen)

2. Perform the division between the two spectra

3. Subtract the mean, which is responsible for the residual DC component after the FFT

4. Restrict the operative range to the region where the interference fringes were clearly visible, to minimize high-frequency and low-frequency noise. This region was typically found to be $623 - 645$ nm. This step inevitably affects the final axial resolution, thus it is important to balance between the reduction of noise and the corresponding decrease in the FWHM

5. At this stage, visibility can be calculated, by simply applying the definition

6. Pass from the wavelength domain to the frequency domain. It is important to perform interpolation in this step, to preserve equal space points along the $x-$axis. The reason is that the FFT algorithm requires a linear relationship between the

data points. However, the simple conversion from wavelengths to frequencies does not grant it.

The frequency step size was chosen to be equal to the largest step in frequencies in the original spectrum [23].

7. Apply the Hilbert transform to the resulting pattern. This strategy allows us to compensate for the chirping term $\rho(\Omega)$ by multiplying the transformed spectrum by a phase term quadratic in frequency $e^{-i\eta(2\pi(f-f_c))^2}$[84] (where f_c is the central frequency). The optimal dispersion coefficient η was found to be equal to 12500×10^{-30} $1/\text{Hz}^2$. It is worth highlighting that the positive sign of alpha must be used when the idler arm path is longer than the reference one. If, instead, it is smaller, the sign should be changed

8. Both windowing and zero-padding are applied to the Hilbert-transformed spectra. In particular, the Hanning window function was chosen, since it is the standard one for preliminary spectral shaping in OCT [85]. Nonetheless, it is important to underline that the Hanning window is known to be associated with a worsening of the axial resolution. The study [81] compares the effects on the FWHM when using the Rectangular window and the Hanning window, before applying the inverse FFT to some simulated interference spectra. The results, reported in Figure K.1, show a much clearer peak in the second case, but at the cost of a significative worsening of the axial resolution from 0.0024 to 0.0041.

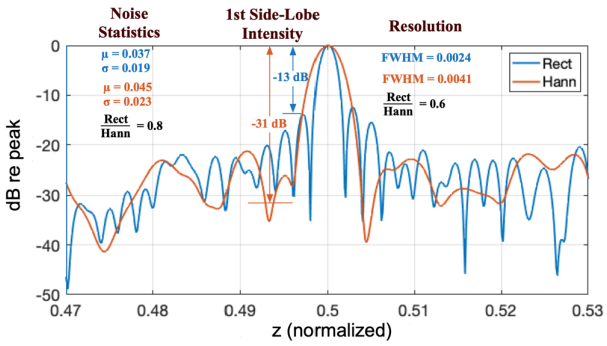

Figure K.1: *The comparison between the performances of the rectangular window and Hanning window applied to some simulated interference patterns. Taken from [81].*

9. Apply the inverse Fast Fourier Transform implemented in the NumPy library and convert the result from the time domain to the depth domain.

It is also important to underline how we can proceed to calculate the various figures of merit:

- The signal power can be simply calculated as the sum of the y-entries of the interference spectrum
- The visibility can be found from the interference data as well, by using the definition (Equation 1.22)

Appendix L

Characterization of OSA noise

To verify if the OSA is responsible for some systematic noise, possibly explaining the discrepancy between the expected linear dependence of the SNR on the number of averages and the observed saturation, I measured the pure electrical noise by removing any input. In the absence of any signal, the sampled data should oscillate around the 0 with standard deviation equal to the pure electrical noise. If we have no systematic effects, we expect the standard deviation value to scale as $1/\sqrt{N}$, with N the number of averages. The experimental plot with the corresponding $y = 1/\sqrt{x}$ fit is reported in Figure L.1

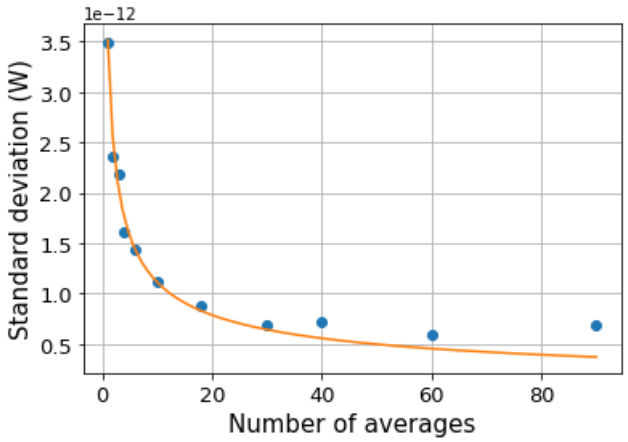

Figure L.1: *The measured standard deviation in the absence of any input at varying number of averages. The orange line corresponds to the fit with the expected function* $y = 1/\sqrt{N}$.

At a high number of averages (> 30), a discrepancy from the expected behavior is observed, possibly indicating the presence of some systematic contributions. Nonetheless, the fit is in extremely good agreement with the data below 30 averages. Since this is the region in which I operated, we can conclude that the detector is not responsible for the

observed saturation of the SNR.

Appendix M

Results of preliminary measurements for NIR-OCT setup

In the case of the NIR-OCT setup, just an essential characterization was performed. An example of the OCT spectrum is reported in Figure M.1a, while Figure M.1b shows the roll-off curve. The NIR-OCT setup displays high SNR (≈ 64.7 dB for depths < 100 μm), long depth range ≈ 2.5 mm, and a very stable axial resolution (6.7 ± 0.2) μm.

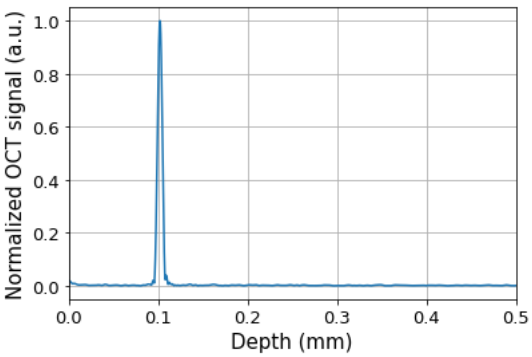

(a) *Example of OCT spectrum obtained with the NIR setup, with the silver mirror at* $z \approx 102$ μm *from the ZPD position.*

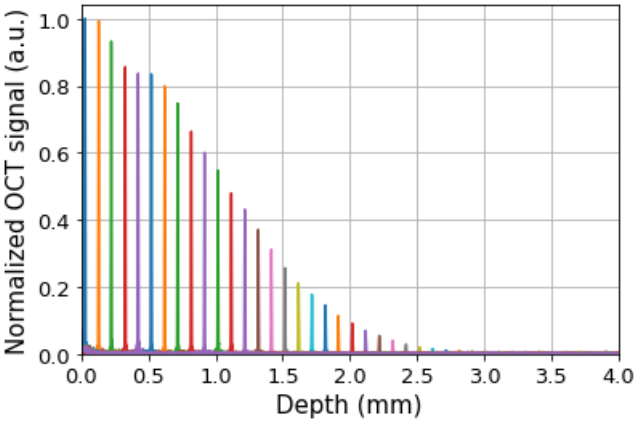

(b) *The experimental roll-off curve for the NIR-OCT setup.*

Figure M.1: *Characterization of the NIR-OCT setup performance.*

The performance can be then considered comparable to the ones of commercially available setups [1]. It is worth noticing that the noninterference spectra are very flat in the measured range (1.3-1.7 μm), despite presenting some anomalies at around 1.38 μm as shown in Figure M.2.

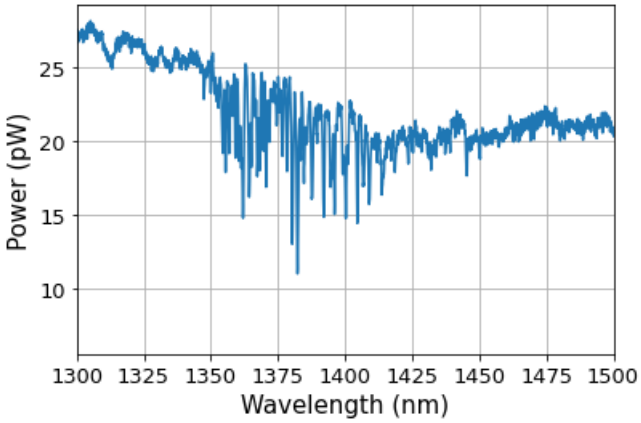

Figure M.2: *An example of non-interference spectrum measured using the NIR-OCT setup. We can notice the irregular behavior due to the water absorption peak at around* 1.38 μm.

This is compatible with the known absorption spectrum of water vapor [86][87]. Nonetheless, the standard analysis procedure satisfactorily compensates for this effect.

Appendix N

Interference spectra simulation and validation for NIR OCT setup

In general, the theory allows us to write the interference spectra as the product between the non-interference ones and the proper interference pattern. Moreover, we should take into account the finite resolution of the spectrometer's response function which might slightly reshape the spectrum during the measurement. To simulate both these effects, I proceeded accordingly to the following steps:

- Experimental sampling of the non-interference spectrum. Since the OSA furnished it, this spectrum is already given by the convolution between the true non-interference spectrum and the response function of the spectrometer.
- Mathematical simulation of the interference pattern, using the theoretical expressions.
- In general, the experimental interference spectrum is given by the convolution between

  1. the product of the non-interference spectrum and the interference pattern
  2. the spectrometer's response function

  However, the response function has a low spectral resolution: this means we can approximate the convolution of the product as the product of the convolutions
- Since we already have the convoluted non-interference spectrum, it is sufficient to convolve the calculated interference pattern with the response function, which was simulated to be a Lorentzian with FWHM equal to the spectral resolution
- For the MIR-OCT simulated spectra, the chirping $\rho(\Omega)$ was taken null for simplicity

- The noise was taken null for simplicity in the simulations.

Figure N.1 shows the optimal agreement between experimental and simulated interference spectra for the NIR OCT setup, validating the written code.

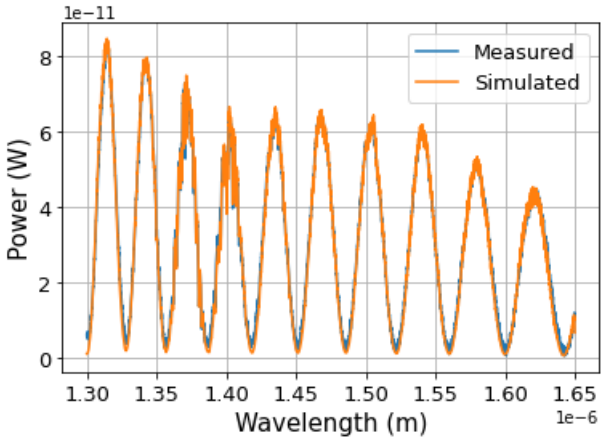

Figure N.1: *Comparison between the experimental and the simulated interference spectra for the NIR-OCT setup, using the silver mirror ($R \approx 1$) as the sample at $z = 31$ μm.*

Bibliography

[1] W. Drexler and J. Fujimoto, *Optical Coherence Tomography: Technology and Applications*. Biological and Medical Physics, Biomedical Engineering, Springer Berlin Heidelberg, 2008.

[2] D. Huang, E. A. Swanson, C. P. Lin, J. S. Schuman, W. G. Stinson, W. Chang, M. R. Hee, T. Flotte, K. Gregory, C. A. Puliafito, *et al.*, "Optical coherence tomography," *Science*, vol. 254, pp. 1178–1181, Nov 1991.

[3] L. M. Sakata, J. DeLeon-Ortega, V. Sakata, and C. A. Girkin, "Optical coherence tomography of the retina and optic nerve – a review," *Clinical & Experimental Ophthalmology*, vol. 37, no. 1, pp. 90–99, 2009.

[4] J. W. Verhoeven, "Glossary of terms used in photochemistry (iupac recommendations 1996)," *Pure and Applied Chemistry*, vol. 68, no. 12, pp. 2223–2286, 1996.

[5] V. Tuchin, *Handbook of Coherent-Domain Optical Methods*. Springer, 2nd ed., 2013.

[6] First International Symposium on Optical Coherence Tomography for Non-Destructive Testing (OCT4NDT), "First International Symposium on Optical Coherence Tomography for Non-Destructive Testing (OCT4NDT)." Linz, Austria. `http://www.oct4ndt.at`, 2013.

[7] C. F. Bohren and D. R. Huffman, *Absorption and Scattering of Light by Small Particles*. Wiley-VCH, 1998.

[8] R. Su, M. Kirillin, E. W. Chang, E. Sergeeva, S. H. Yun, and L. Mattsson, "Perspectives of mid-infrared optical coherence tomography for inspection and micrometrology of industrial ceramics," *Opt. Express*, vol. 22, pp. 15804–15819, Jun 2014.

[9] J. M. Charsley, C. Farrell, M. Rutkauskas, P. G. Schunemann, and D. T. Reid, "Mid-infrared optical coherence tomography with a stabilized op-gap optical parametric oscillator," *Opt. Lett.*, vol. 49, pp. 2882–2885, Jun 2024.

[10] T. Amotchkina, M. Trubetskov, D. Hahner, and V. Pervak, "Characterization of e-beam evaporated ge, ybf3, zns, and laf3 thin films for laser-oriented coatings," *Appl. Opt.*, vol. 59, pp. A40–A47, Feb 2020.

[11] A. Rogalski, *Infrared Detectors*. CRC Press, 2nd ed., 2011.

[12] C. S. Colley, J. C. Hebden, D. T. Delpy, A. D. Cambrey, R. A. Brown, E. A. Zibik, W. H. Ng, L. R. Wilson, and J. W. Cockburn, "Mid-infrared optical coherence tomography," *Review of Scientific Instruments*, vol. 78, no. 12, p. 123108, 2007.

[13] A. F. Fercher, "Optical coherence tomography," *Journal of Biomedical Optics*, vol. 1, pp. 157–173, Apr 1996.

[14] D. Varnell, M. C. Zheng, M. Chow, and C. Gmachl, "Spectroscopy and imaging using a mid-ir quantum cascade optical coherence tomography (oct) system," in *Conference on Lasers and Electro-Optics*, p. ATu1J.7, Optica Publishing Group, 2016.

[15] I. Zorin, P. Gattinger, A. Prylepa, and B. Heise, "Time-encoded mid-infrared fourier-domain optical coherence tomography," *Opt. Lett.*, vol. 46, pp. 4108–4111, Sep 2021.

[16] I. Zorin, R. Su, A. Prylepa, J. Kilgus, M. Brandstetter, and B. Heise, "Mid-infrared fourier-domain optical coherence tomography with a pyroelectric linear array," *Opt. Express*, vol. 26, pp. 33428–33439, Dec 2018.

[17] Q. Hu, J. S. Dam, C. Pedersen, and P. Tidemand-Lichtenberg, "High-resolution mid-ir spectrometer based on frequency upconversion," *Opt. Lett.*, vol. 37, pp. 5232–5234, Dec 2012.

[18] N. M. Israelsen, C. R. Petersen, A. Barh, D. Jain, M. Jensen, G. Hannesschläger, P. Tidemand-Lichtenberg, C. Pedersen, A. G. Podoleanu, and O. Bang, "Real-time high-resolution mid-infrared optical coherence tomography," *Light, Science & Applications*, vol. 8, 2018.

[19] S. Yagi, T. Nakamura, K. Hashimoto, S. Kawano, and T. Ideguchi, "Mid-infrared optical coherence tomography with mhz axial line rate for real-time non-destructive testing," 2023.

[20] K. Hashimoto, T. Nakamura, T. Kageyama, V. Badarla, H. Shimada, R. Horisaki, and T. Ideguchi, "Upconversion time-stretch infrared spectroscopy," *Light: Science & Applications*, vol. 12, p. 48, 03 2023.

[21] M. V. Chekhova and Z. Y. Ou, "Nonlinear interferometers in quantum optics," *Adv. Opt. Photon.*, vol. 8, pp. 104–155, Mar 2016.

[22] A. V. Paterova, H. Yang, C. An, D. A. Kalashnikov, and L. A. Krivitsky, "Tunable optical coherence tomography in the infrared range using visible photons," *Quantum Science and Technology*, vol. 3, p. 025008, apr 2018.

[23] A. Vanselow, P. Kaufmann, I. Zorin, B. Heise, H. M. Chrzanowski, and S. Ramelow, "Frequency-domain optical coherence tomography with undetected mid-infrared photons," *Optica*, vol. 7, pp. 1729–1736, Dec 2020.

[24] G. J. Machado, G. Frascella, J. P. Torres, and M. V. Chekhova, "Optical coherence tomography with a nonlinear interferometer in the high parametric gain regime," 2020.

[25] C. Lindner, J. Kunz, S. J. Herr, J. Kiessling, S. Wolf, and F. Kühnemann, "High-sensitivity quantum sensing with pump-enhanced spontaneous parametric down-conversion," *APL Photon.*, vol. 8, no. 5, p. 051301, 2023.

[26] K. Spasibko, "Spectral and statistical properties of high-gain parametric down-conversion," 2020.

[27] T. S. Iskhakov, A. M. Pérez, K. Y. Spasibko, M. V. Chekhova, and G. Leuchs, "Superbunched bright squeezed vacuum state," *Opt. Lett.*, vol. 37, pp. 1919–1921, Jun 2012.

[28] K. Hashimoto, D. B. Horoshko, and M. V. Chekhova, "Broadband spectroscopy and interferometry with undetected photons at strong parametric amplification," *Advanced Quantum Technologies*, vol. n/a, no. n/a, p. 2300299.

[29] K. Hashimoto, D. B. Horoshko, M. I. Kolobov, Y. Michael, Z. Gefen, and M. V. Chekhova, "Fourier-transform infrared spectroscopy with undetected photons from high-gain spontaneous parametric down-conversion," 2024.

[30] J. S. Schuman, C. A. Puliafito, and J. G. Fujimoto, *Optical Coherence Tomography of Ocular Diseases*. Thorofare, NJ: Slack Inc., 2nd ed., 2004.

[31] F. Mark, *Quantum Optics: An Introduction*. Oxford University Press, 2006.

[32] A. Podoleanu, "Optical coherence tomography," *The British journal of radiology*, vol. 78, pp. 976–88, Mar. 2012.

[33] S. Taplin, A. G. Podoleanu, D. J. Webb, and D. A. Jackson, "Displacement sensor using channelled spectrum dispersed on a linear CCD array," *Electronics Letters*, vol. 29, p. 896, May 1993.

[34] W. Wieser, B. R. Biedermann, T. Klein, C. M. Eigenwillig, and R. Huber, "Multi-megahertz oct: High quality 3d imaging at 20 million a-scans and 4.5 gvoxels per second," *Opt. Express*, vol. 18, pp. 14685–14704, Jul 2010.

[35] T. Klein, W. Wieser, C. M. Eigenwillig, B. R. Biedermann, and R. Huber, "Megahertz oct for ultrawide-field retinal imaging with a 1050nm fourier domain mode-locked laser," *Opt. Express*, vol. 19, pp. 3044–3062, Feb 2011.

[36] J. Kalkman, "Fourier-domain optical coherence tomography signal analysis and numerical modeling," *International Journal of Optics*, vol. 2017, pp. 1–16, 03 2017.

[37] K. Zetie, S. Adams, and R. Tocknell, "How does a mach-zehnder interferometer work?," *Physics Education*, vol. 35, 01 2000.

[38] R. Leitgeb, C. K. Hitzenberger, and A. F. Fercher, "Performance of fourier domain vs. time domain optical coherence tomography," *Opt. Express*, vol. 11, pp. 889–894, Apr 2003.

[39] A. Agrawal, T. J. Pfefer, P. D. Woolliams, P. H. Tomlins, and G. Nehmetallah, "Methods to assess sensitivity of optical coherence tomography systems," *Biomed. Opt. Express*, vol. 8, pp. 902–917, Feb 2017.

[40] S. Aja-Fernández and G. Vegas Sánchez-Ferrero, *Statistical Analysis of Noise in MRI*. 01 2016.

[41] M. Ali and R. Parlapalli, "Algorithms for optical coherence tomography on tms320c64x+." Application Report SPRABB7–June 2010, June 2010.

[42] S. Aumann, S. Donner, J. Fischer, and F. Müller, *Optical Coherence Tomography (OCT): Principle and Technical Realization*, pp. 59–85. Cham: Springer International Publishing, 2019.

[43] Z. Gao, R. Jia, H. Zhang, Z. Xia, and W. Fang, "Simulation and analysis of spectral response function and bandwidth of spectrometer," *International Journal of Aerospace Engineering*, vol. 2016, no. 1, p. 2759121, 2016.

[44] R. Paschotta, "Gaussian beams." RP Photonics Encyclopedia. Available online at `https://www.rp-photonics.com/gaussian_beams.html`.

[45] K. Serrels, M. Renner, and D. Reid, "Optical coherence tomography for non-destructive investigation of silicon integrated-circuits," *Microelectronic Engineering*, vol. 87, no. 9, pp. 1785–1791, 2010. 11th SEMATECH Surface Preparation and Cleaning Conference.

[46] R. Gerhardt, *Properties and Applications of Silicon Carbide*. Rijeka: IntechOpen, Apr 2011.

[47] R. W. Boyd, "Chapter 1 - the nonlinear optical susceptibility," in *Nonlinear Optics (Third Edition)* (R. W. Boyd, ed.), pp. 1–67, Burlington: Academic Press, third edition ed., 2008.

[48] R. W. Boyd, "Chapter 2 - wave-equation description of nonlinear optical interactions," in *Nonlinear Optics (Third Edition)* (R. W. Boyd, ed.), pp. 69–133, Burlington: Academic Press, third edition ed., 2008.

[49] C. Couteau, "Spontaneous parametric down-conversion," *Contemporary Physics*, vol. 59, p. 291–304, July 2018.

[50] W. H. Louisell, A. Yariv, and A. E. Siegman, "Quantum fluctuations and noise in parametric processes. i.," *Phys. Rev.*, vol. 124, pp. 1646–1654, Dec 1961.

[51] D. N. Klyshko, "Coherent photon decay in a nonlinear medium," 1967.

[52] B. Y. Zel'dovich and D. N. Klyshko, "Field statistics in parametric luminescence," *Pisma v ZhETF*, vol. 9, p. 69, 1969.

[53] D. Magde and H. Mahr, "Study in ammonium dihydrogen phosphate of spontaneous parametric interaction tunable from 4400 to 16 000 å," *Phys. Rev. Lett.*, vol. 18, pp. 905–907, May 1967.

[54] S. E. Harris, M. K. Oshman, and R. L. Byer, "Observation of tunable optical parametric fluorescence," *Phys. Rev. Lett.*, vol. 18, pp. 732–734, May 1967.

[55] S. A. Akhmanov, V. V. Fadeev, R. V. Khokhlov, and O. N. Chunaev, "Quantum noise in parametric light amplifiers," *ZhETF Pisma Redaktsiiu*, vol. 6, p. 575, Aug. 1967. Provided by the SAO/NASA Astrophysics Data System.

[56] D. C. Burnham and D. L. Weinberg, "Observation of simultaneity in parametric production of optical photon pairs," *Phys. Rev. Lett.*, vol. 25, pp. 84–87, Jul 1970.

[57] J. Y. Cheung, C. J. Chunnilall, E. R. Woolliams, N. P. Fox, J. R. Mountford, and J. Wang, "The quantum candela: a re-definition of the standard units for optical radiation," *Journal of Modern Optics*, vol. 54, no. 2-3, pp. 373–396, 2007.

[58] N. Gisin, G. Ribordy, W. Tittel, and H. Zbinden, "Quantum cryptography," *Rev. Mod. Phys.*, vol. 74, pp. 145–195, Mar 2002.

[59] J. L. O'Brien, "Optical quantum computing," *Science*, vol. 318, p. 1567–1570, Dec. 2007.

[60] R. Dändliker, "The concept of modes in optics and photonics," in *Education and Training in Optics and Photonics*, p. GP193, Optica Publishing Group, 1999.

[61] R. Loudon, *The Quantum Theory of Light*. Oxford University Press, 3rd ed., 2000.

[62] Y. D. Chong, "Quantum mechanics iii (chong)." Physics LibreTexts, Nanyang Technological University, April 30 2021.

[63] D. N. Klyshko, *Photons and Nonlinear Optics*. Amsterdam: Gordon and Breach Science Publishers, 1988.

[64] M. I. Kolobov, "The spatial behavior of nonclassical light," *Rev. Mod. Phys.*, vol. 71, pp. 1539–1589, Oct 1999.

[65] D. B. Horoshko and M. I. Kolobov, "Generation of monocycle squeezed light in chirped quasi-phase-matched nonlinear crystals," *Phys. Rev. A*, vol. 95, p. 033837, Mar 2017.

[66] K. Y. Spasibko, T. S. Iskhakov, and M. V. Chekhova, "Spectral properties of high-gain parametric down-conversion," *Opt. Express*, vol. 20, pp. 7507–7515, Mar 2012.

[67] M. Houe and P. D. Townsend, "An introduction to methods of periodic poling for second-harmonic generation," *Journal of Physics D: Applied Physics*, vol. 28, p. 1747, sep 1995.

[68] K. Rustagi, S. Mehendale, and S. Meenakshi, "Optical frequency conversion in quasi-phase-matched stacks of nonlinear crystals," *IEEE Journal of Quantum Electronics*, vol. 18, no. 6, pp. 1029–1041, 1982.

[69] E. J. Lim, M. M. Fejer, and R. L. Byer, "Second harmonic generation of green light in periodically poled planar lithium niobate waveguide," *Electron. Lett.*, vol. 25, pp. 174–175, 1989.

[70] X. Y. Zou, L. J. Wang, and L. Mandel, "Induced coherence and indistinguishability in optical interference," *Phys. Rev. Lett.*, vol. 67, pp. 318–321, Jul 1991.

[71] G. Barreto Lemos, M. Lahiri, S. Ramelow, R. Lapkiewicz, and W. N. Plick, "Quantum imaging and metrology with undetected photons: tutorial," *Journal of the Optical Society of America B*, vol. 39, p. 2200, July 2022.

[72] F. Roeder, R. Pollmann, M. Stefszky, M. Santandrea, K.-H. Luo, V. Quiring, R. Ricken, C. Eigner, B. Brecht, and C. Silberhorn, "Optical coherence tomography with undetected photons based on an integrated pdc source," p. JTu5A.55, 01 2023.

[73] Y. T. . Measurement, "Optical spectrum analyzer technology." https://tmi.yokogawa.com/us/solutions/products/optical-measuring-instruments/optical-spectrum-analyzer/, n.d. Accessed: 2023-10-05.

[74] N. Rajesh, "Review on gray track effects on potassium titanyl phosphate single crystals," *Juniper Online Journal Material Science*, vol. 3, 12 2017.

[75] T. Optics, "Germanium." https://www.tydexoptics.com/materials1/for_transmission_optics/germanium/. Accessed: 2023-10-05.

[76] I. Lombardero, M. Ochoa, N. Miyashita, Y. Okada, and C. Algora, "Theoretical and experimental assessment of thinned germanium substrates for iii–v multijunction solar cells," *Progress in Photovoltaics: Research and Applications*, vol. 28, no. 11, pp. 1097–1106, 2020.

[77] M. N. Polyanskiy, "Refractiveindex.info database of optical constants," *Sci. Data*, vol. 11, p. 94, 2024.

[78] Y. T. . M. Corporation, *User's Manual AQ6374 Optical Spectrum Analyzer*. Yokogawa Test & Measurement Corporation, 4th edition ed., 2023. IM AQ6374-01EN.

[79] V. Behar, D. Adam, and Z. Friedman, "A new method of spatial compounding imaging," *Ultrasonics*, vol. 41, pp. 377–84, Jul 2003. Accessed: 2023-10-25.

[80] B. Potsaid, I. Gorczynska, V. J. Srinivasan, Y. Chen, J. Jiang, A. Cable, and J. G. Fujimoto, "Ultrahigh speed spectral / fourier domain oct ophthalmic imaging at 70,000 to 312,500 axial scans per second," *Opt. Express*, vol. 16, pp. 15149–15169, Sep 2008.

[81] C. B. Walker, A. Wisniowiecki, J. C. Tang, P. M. Quiñones, W. Kim, J. S. Oghalai, and B. E. Applegate, "Multi-window approach enables two-fold improvement in OCT axial resolution with strong side-lobe suppression and improved phase sensitivity," *Biomed Opt Express*, vol. 14, pp. 6301–6316, Nov 2023.

[82] M. Mylonakis, S. Pandey, K. G. Mavrakis, G. Drougakis, G. Vasilakis, D. G. Papazoglou, and W. von Klitzing, "Simple precision measurements of optical beam sizes," *Appl. Opt.*, vol. 57, pp. 9863–9867, Nov 2018.

[83] V. Lozovsky, "Avaspec-3648 fiber optic spectrometer." https://www.avantes.ru/en/spectrometer/avaspec3648.php, n.d.

[84] M. Wojtkowski, V. J. Srinivasan, T. H. Ko, J. G. Fujimoto, A. Kowalczyk, and J. S. Duker, "Ultrahigh-resolution, high-speed, fourier domain optical coherence tomography and methods for dispersion compensation," *Opt. Express*, vol. 12, pp. 2404–2422, May 2004.

[85] D. Hillmann, T. Bonin, C. Lührs, G. Franke, M. Hagen-Eggert, P. Koch, and G. Hüttmann, "Common approach for compensation of axial motion artifacts in swept-source oct and dispersion in fourier-domain oct," *Opt. Express*, vol. 20, pp. 6761–6776, Mar 2012.

[86] R. G. Eldridge, "Water vapor absorption of visible and near infrared radiation," *Appl. Opt.*, vol. 6, pp. 709–713, Apr 1967.

[87] I. E. Gordon and al., "The HITRAN2020 molecular spectroscopic database," vol. 277, p. 107949, Jan. 2022.